Spin-dependent heat transport and thermal boundary resistance

Submitted in partial fulfillment of the requirements for

the degree of

Doctor of Philosophy

in

Electrical and Computer Engineering

Taehee Jeong

B.S., Ceramic Engineering, Inha University
M.S., Materials Science and Engineering, Pohang University of Science and Technology
M.S., Materials Science and Engineering, Pennsylvania State University

Carnegie Mellon University
Pittsburgh, PA

May, 2011

Acknowledgments

I have had the pleasure of working with many exceptional people during my time at Carnegie Mellon University. First and foremost, I wish to heartily thank my advisor, Professor Jimmy Zhu, for the chance to pursue my graduate studies under his guidance and instruction. He served the chair of the committee for my thesis. I wish to acknowledge the assistance and advice of my thesis committee which consists of Professor Jimmy Zhu, Professor David Laughlin, Professor Jim Bain, Dr. Matthew Gibbons, for their interest and discussion of this thesis. In addition, I would like to appreciate Professor David Lambeth for fruitful discussions for magnetism.

I also extends my heartfelt thanks to my colleagues in Data Storage Systems Center (DSSC) : Dr. Matthew T. Moneck, Dr. Jeong-Heon Park, Mr. Andrew Gamble who has taught me various fabrication and measurement resources. I would also like to thank cleanroom staffs, Carsen Kline, Mike Sakaluk, Tim Fisher, and Chris Bowman for their facilitating machines at the cleanroom. Also I got a lot of help from Dr. Wen-Chi Lin for Labview programing, Dr. Yiming Wang for Matlab programing, Mr. Tom Nuhfer and Dr. Suk Chung for TEM images, Mr. Jason Wolf for XRD and AFM measurement, Mr. Andy Zhang for SEM images, Mr. Nathan Lazarus for wire-bonding.

I would like to thank Dr. Matthew Gibbons from Western Digital Corporation and Dr. Min Xiao from Seagate technology. Their guidance and helps during my internship are truly appreciated.

I would like to express my sincere thanks to Dr. Yizhang Yang and Professor Mehdi Asheghi for their fruitful discussion for the transient thermoreflectance setup.

I would like to thank the DSSC at Carnegie Mellon University, and the support team of the DSSC, for providing an excellent research environment and tight collaborations with the magnetic storage industries.

Sincere appreciation is expressed for the partial financial support of the National Science Foundation and DSSC which made this work possible.

I wish to express my deepest gratitude to my mother and mother-in-law for their endless love and prayer. Without their prayer, this would not have been possible.

Last, but certainly not least, I would like to thank my wife Eunnam Choi, and our children, Esther (Suhyun), Joseph, Joshua, for standing by me. Your love, encouragement, and forbearance are what made this possible in the end.

Abstract

Spin-dependent heat transport is a new research area and can create many future applications. The Giant Magnetoresistance (GMR) effect, which was discovered in 1988, is significant change in electric resistance due to spin-dependent electron scattering. The GMR effect has greatly impacted on techniques of data storage and magnetic sensors. For example, the areal density of hard disk drive was increased 100 times using the GMR effect. Likewise, spin-dependent heat transport, which is also called the Giant Magnetothermal Resistance (GMTR) effect, is expected to create a wealth of new applications, for example nanoscale heat or temperature detectors and spin thermoelectrics. In addition, the technique developed for this study will help with heat management in micro/nano electronics including data storage devices and heat/energy assisted magnetic recording.

In this thesis, thermal conductivity change depending on the magnetic configurations has been studied. In order to make different magnetic configurations, we developed a spin valve structure, which has high MR ratio and low saturation field. The high MR ratio was achieved using Co/Cu multilayer and 21Å or 34Å thick Cu layer. The low saturation field was obtained by implementing different coercivities of the successive ferromagnetic layers. For this purpose, Co/Cu/Cu tri-layered structure was used with the thicknesses of the Co layers; 15 Å and 30 Å. For the thermal conductivity measurement, a three-omega method was employed with a thermally isolated microscale rod. We fabricated the microscale rod using optical

lithography and MEMS process. Then the rod was wire-bonded to a chip-carrier for further electrical measurement. For the thermal conductivity measurement, we built the three-omega measurement system using two lock-in amplifiers and two differential amplifiers. A custom-made electromagnet was added to the system to investigate the impact of magnetic field.

We observed titanic thermal conductivity change depending on the magnetic configurations of the Co/Cu/Co multilayer. The thermal conductivity change was closely correlated with that of the electric conductivity in terms of the spin orientation, but the thermal conductivity was much more sensitive than that of the electric conductivity. The relative thermal conductivity change was 50% meanwhile that of electric resistivity change was 8.0%. The difference between the two ratios suggests that the scattering mechanism for charge and heat transport in the Co/Cu/Co multilayer is different. The Lorentz number in Weidemann-Franz law is also spin-dependent. The application of this significant thermal conductivity change is remained for future work.

Thermal boundary resistance between metal and dielectrics was also studied in this thesis. The thermal boundary resistance becomes critical for heat transport in a nanoscale because the thermal boundary resistance can potentially determine overall heat transport in thin film structures. A transient thermoreflectance (TTR) technique can be used for measuring the thermal conductivity of thin films in cross-sectional direction. In this study, a pump-probe scheme was employed for the TTR technique. We built an optical pump-probe system by using a nanosecond pulse laser for

pumping and a continuous-wave laser for probing. A short-time heating event occured at the surface of a sample by shining a laser pulse on the surface. Then the time-resolved thermoreflectance signals were detected using a photodetector and an oscilloscope. The increased temperature decreases slowly and its thermal decay depends on the thermal properties of a sample. Since the reflectivity is linearly proportional to the temperature, the time-resolved thermoreflectance signals have the information of the thermal properties of a sample. In order to extract the thermal properties of a sample, a thermal analysis was performed by fitting the experimental data with thermal models. We developed 2-layered and 3-layered thermal models using the analogies between thermal conduction and electric conduction and a transmission-line concept.

We used two sets of sample structures: Au/SiN_x/Si substrate and Au/CoFe/SiN_x/Si substrate with various thickness of SiN_x layer. Using the pump-probe system, we measured the time-resolved thermoreflectance signals for each sample. Then, the thermal conductivity and thermal boundary resistance were obtained by fitting the experimental data with the thermal models. The thermal conductivity of SiN_x films was measured to be 2.0 W/mK for both structures. In the case of the thermal boundary resistance, it was 0.81×10^{-8} m^2K/W at the Au/SiN_x interface and 0.54×10^{-8} m^2K/W at the CoFe/SiN_x interface, respectively. The difference of the thermal boundary resistance between Au/SiN_x and CoFe/SiN_x might be came from the different phonon dispersion of Au and CoFe. The thermal conductivity did not depend on the thickness of SiN_x films in the thickness range of

50-200nm. However, the thermal boundary resistance at metal/SiN_x interfaces will impact overall thermal conduction when the thickness of SiN_x thin films is in a nanometer order. For example, apparent thermal conductivity of SiN_x film becomes half of the intrinsic thermal conductivity when the thickness decreases to 16nm. Therefore, it is advised that the thermal boundary resistance between metal and dielectrics should be counted in nano-scale electronic devices.

Table of Contents

List of Figures

List of Tables

1 Introduction

This thesis consists of two parts. One part is spin-dependent heat transport, and the other part is thermal boundary resistance. For the study of the spin-dependent heat transport, a three-omega method was employed. For the thermal boundary resistance, a transient thermoreflectance technique was used. In this thesis, not only sample preparation and measuring physical phenomena, but also designing and building of the two measurement system were emphasized. In addition, the size effect of copper films was investigated since the thickness of each layer for current multilayered samples is in the range of under strong size effect.

1.1 Motivation

It is well established that the thermal conductivity in metals is proportional to the electrical conductivity [1] due to the electronic contribution to the thermal conductivity. Even though the observed thermal conductivity is the sum of the electronic and phonon conductivity, the contribution of phonons to the heat transport is negligible in metals [2, 3]. Therefore, the thermal conductivity in metals can be predicted from the electric conductivity using a linear relationship based on Weidemann-Franz law [1, 2, 4].

When electric currents pass through a spin-valve structure such as a ferromagnetic/non-magnetic/ferromagnetic sandwich structure, the up and down spin in the currents will experience different electric resistance depending on the magnetic

directions of the two ferromagnetic layers. When the two magnetic layers have opposite magnetic directions, the structure has a high electric resistance. When the two layers have the same magnetic direction, the resistance becomes low. This phenomenon is called Giant Magnetoresistance (GMR) effect [5, 6]. The GMR effect is due to the spin dependence of electron scattering from ferromagnetic thin films and their interfaces [5, 7]. Since electrons are the main carriers for thermal conduction in metals, it is generally expected that the behavior of the thermal conductivity would be similar to the behavior of the electrical conductivity in a spin-valve structure. However, this hypothesis has not been verified experimentally.

Electrons carry charge and heat in metals. The electric conduction is due to charge transport. In the case of a spin-valve structure, the electric transport depends on the spin-dependent scattering at ferromagnetic layers and their interface [5, 7]. However, there is no supporting literature that the spin-dependent scattering rate for heat and charge would be the same. If the scattering rate for both is different, the ratio of the thermal conductivity change in a spin-valve structure would be different from that of the electrical conductivity. One of the easiest ways to examine the hypothesis is to measure the thermal conductivity change of a spin-valve structured film while sweeping a magnetic field. However, measuring the heat transport of very thin films and their multilayer structures is often significantly more difficult than measuring the electric transport. One of the difficulties in measuring the heat transport of thin films is that the thermal conduction through substrates is significantly larger compared to that of the films, which often makes the desired thermal measurements inaccurate.

This would be one of the reasons why only a few literatures [8-10] are reported for Giant Magnetothermal Resistance (GMTR) effect.

The GMR effect opened the door to new scientific and technological possibilities, including a great influence on techniques of data storage and magnetic sensors. Likewise, spin-dependent heat transfer, which is also called the GMTR effect, is expected to create a wealth of new applications, for example nanoscale heat or temperature detection. In addition, it will help with heat management in data storage devices and heat/energy assisted magnetic recording [11, 12].

One of the objectives of this thesis is to investigate the spin-dependent heat transport phenomenon. To achieve this goal, we developed a spin-valve structure with 10% MR ratio. Using the spin-valve structure, we fabricated a microscale thermally isolated bridge structure for thermal measurement. For the thermal conductivity measurement of thin films, a three-omega (3ω) method is employed. Eventually, we observed thermal transport in a magnetic multilayer depending on the magnetic directions of the two ferromagnetic layers, i.e. spin-dependent heat transport with a thermally isolated bridge structure.

Another objective of this thesis is to investigate thermal boundary resistance between metal and dielectrics. Thermal boundary resistance is the thermal resistance between dissimilar materials. When heat flux passes through two different materials, the temperature of the two materials can be different due to the thermal boundary resistance. In nanoscale electronic devices, the thermal boundary resistance can impact overall heat transport instead of thermal properties of individual layers, in

particular between metals and dielectrics. This study describes the thermal boundary resistance between Au/SiN_x and CoFe/SiN_x. For this study, we built an optical pump-probe measurement system based on the transient thermoreflectance technique for measurement of cross-sectional heat transport of thin films. In this study, we fabricated the two sample structures: Au/SiN_x/Si substrate and Au/CoFe/SiN_x/Si substrate with a wide range of thickness of SiN_x layer. After analyzing the time-resolved thermoreflectance signals, we got the thermal conductivity of SiN_x with and the thermal boundary resistance at the interface of Au/SiN_x and CoFe/SiN_x.

1.2 Thesis Outline

In Chapter 1, the motivation and objective of this study are introduced.

In Chapter 2, the physics of GMR effect and a spin-valve structure for high MR ratio and low saturation field are addressed.

In Chapter 3, experimental procedures for spin-dependent heat transport are described in detail. Thin film deposition of a spin-valve structure, optical lithography procedure for four-point probe structure, MEMS processes for a thermally isolated bridge structure, steady-state joule heating setup, three-omega setup are addressed in this chapter.

In Chapter 4, Development of a spin-valve structure and its MR results are first described. Then, the experimental results of a spin-valve structure by using steady state joule heating measurement and its practical and fundamental problems are addressed. Finally, the experimental results of the thermal conductivity and its

spin-dependency by using the three-omega method are addressed.

In Chapter 5, experimental procedures for the pump-probe method are described in detail. The pump-probe method is based on the transient thermoreflectance (TTR) technique. The principle and experimental detail for the setup are addressed.

In order to extract thermal properties from the TTR measurement, analytical solutions are required. In Chapter 6, we addressed in-detail mathematical steps based on the transmission-line technique to get the analytical solutions.

In Chapter 7, we describe the results for the thermal conductivity of SiNx films with different thickness using the TTR technique. In addition, we describe the experimental data of thermal boundary resistance at Au/SiN_x and $CoFe/SiN_x$ interface using the TTR method. We discussed the origin of the difference of the thermal boundary resistance and the impact for heat transport when the thickness of SiN_x films in a nanoscale.

In Chapter 8, Size effect of Cu films are presented. Since the thickness of each layer in the spin-valve structure is a few nanometers, the electric conductivity is under the size effect. Some preliminary analysis is addressed.

Chapter 9 summarized the entire dissertation and recommended the future works.

2 Background

2.1 Physics of GMR effect

In magnetic recording, information is stored as the local orientation of magnetization in ferromagnets. In order to read the stored information, we need to measure the orientation. One of the ways to read the information is to use the GMR effect. In fact, the GMR effect and a read head using the effect contributed to the increase in Hard Disk Drive (HDD) areal recording density from 0.1 to 100 Gbit /in^2 between 1991 and 2003 [13].

The GMR effect is a significant change in the electrical resistance of the ferromagnetic multilayers depending on magnetic configuration of the ferromagnetic multilayers. The GMR effect stems from the spin-dependent scattering of conduction electrons in the ferromagnetic layers and their interface [5]. For the ferromagnetic metals Fe, Ni, Co and their alloys, both the 4s and 3d electron bands contribute to the density of states at the Fermi level E_F. Due to exchange coupling between the two bands, the energy of spin-up and spin-down 3d bands is separated [13, 14]. Hence, the density of state of the two bands at E_F becomes different [7]. This spin-dependent density of state at E_F causes spin-dependent scattering for conduction electrons.

4s electrons dominates electric conduction in a ferromagnetic multilayered structure since 4s electrons have a much higher mobility. Since the electrons try to keep the same spin-direction within spin-flipping length [14], the conduction electrons will experience different scattering from the ferromagnetic layer depending

on the spin direction. For example, if the spin direction of the conduction electrons is the opposite with the magnetic direction of the ferromagnetic layer, the electrons will experience scattering when they pass through the ferromagnetic layers. If the spin direction is the same with the magnetic direction, the electrons do not experience any scattering.

In order to understand the spin-dependent scattering, the electron band structure and its density of state for Co and Cu are addressed [7] since a Co/Cu/Co multilayered structure is used for the current study. In the case of Cu, the band structure is the same for the up-spin and down-spin electrons. The d bands are fully occupied and density of state at the Fermi energy is almost empty [7], which results in high electric conductivity of Cu. Meanwhile, in the case of Co, the d band is split and the electronic band structure is different depending on the two spin orientations [7]. For majority-spin electrons, the density of state at the Fermi level is almost empty, while for minority-spin electrons, the density of state at the Fermi level is fully occupied. This different density of state results in spin-dependent scattering.

Figure 2-1 illustrates what happens as the up-spin and down-spin electrons pass through a multilayer stack composed of alternating ferromagnetic layers and non-ferromagnetic layers. Figure 2-1(a) shows that the ferromagnetic layers are magnetized at one direction, which is called parallel state. When the spin direction of electrons is the same with the magnetization of the ferromagnetic layers, electrons experience almost no scattering. But when the spin direction is the opposite with the magnetic direction, the electrons experience scattering when they pass through the

ferromagnetic layers. Since the spin conduction can be treated as a two-channel, overall resistance will be low. Meanwhile Figure 2-1(b) shows the magnetic directions of the ferromagnetic layers are aligned opposite direction. When the ferromagnetic layers are anti-parallel, both spin-up and spin-down electrons undergo collisions, giving rise to a high overall resistance.

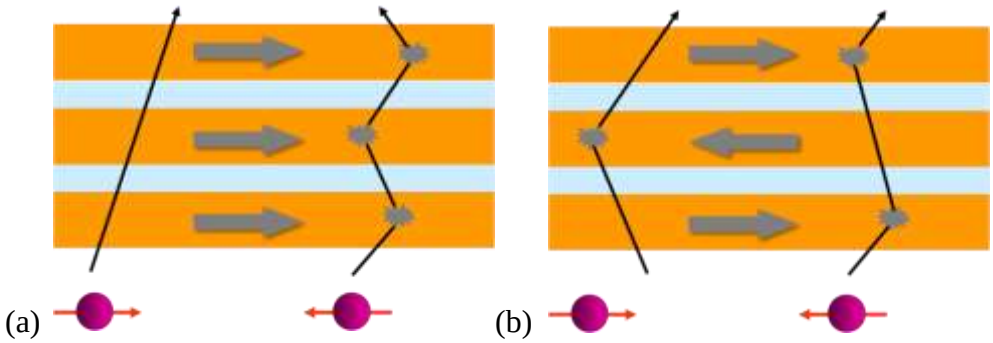

Figure 2-1 Schematics of the spin-dependent electrons scattering in a ferromagnetic/non-magnetic/ferromagnetic multilayer stack; (a) when the magnetic orientation of the ferromagnetic layers are parallel, (b) when the magnetic orientation of the ferromagnetic layers are antiparallel.

This spin-dependent scattering process can be represented by a two current channel model [15] illustrated in Figure 2-2. In this model, the up-spin and down-spin conduction channels are connected in parallel. The resulting resistances of the non-scattering and scattering events are represented as r and R, respectively. For the parallel configuration, the total resistance can be derived as follows.

$$\frac{1}{R_{total}} = \frac{1}{2r} + \frac{1}{2R} \qquad 2\text{-}1$$

$$\frac{1}{R_{total}} = \frac{R+r}{2Rr} \qquad 2\text{-}2$$

$$R_{total} = \frac{2Rr}{R+r} \qquad 2\text{-}3$$

$$R_{total} \approx 2r\,(if \quad R >> r) \qquad 2\text{-}4$$

Also the total resistance in the case of anti-parallel configuration can be derived as follows.

$$\frac{1}{R_{total}} = \frac{1}{R+r} + \frac{1}{R+r} \qquad 2\text{-}5$$

$$\frac{1}{R_{total}} = \frac{2}{R+r} \qquad 2\text{-}6$$

$$R_{total} = \frac{R+r}{2} \qquad 2\text{-}7$$

$$R_{total} \approx \frac{R}{2}\,(if \quad R >> r) \qquad 2\text{-}8$$

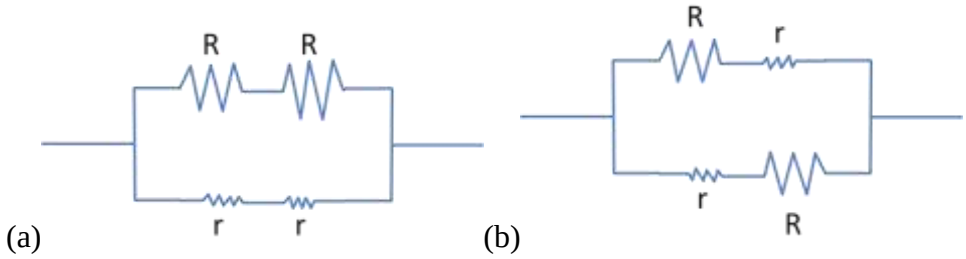

(a) (b)

Figure 2-2 Two-channel model to describe the GMR effect; (a) parallel and (b) anti-parallel configuration

It is clear that total resistance of anti-parallel configuration will be much higher than that of parallel configuration by assuming that the resistance of scattering is much higher than that of non-scattering.

2.2 Spin value structure for high MR and low saturation field

Our sub-goal is to develop a spin-valve sample with a high MR ratio and low saturation field. Since the MR ratio is expected to be relevant to the thermal conductivity change, it will be easy to detect spin-dependent heat transport using the high MR ratio sample. After the GMR effect was discovered at 1988 [5, 6] and a lot of research has been performed to increase the MR ratio. However, it is not straightforward to get the high MR ratio with low saturation field at room temperature.

The general MR ratio to achieve is 5-6% by using typical sputtering [14]. In literature a 20% MR ratio are reported at room temperature [13, 14]. However, it was achieved using a complicated layered structure and specular reflection with atomic scale controlled layer thickness and surface roughness [16]. In addition, a high MR ratio sample usually has high saturating magnetic field [6]. But the high saturating field is not appropriate for the current study. For the current study, the maximum field to apply is limited to less than 700 Oe. We use a custom-made electromagnet, which does not include a cooling water system. The cooling system is essential for generating high magnetic field. After all, our sub-goal is set to develop a spin-valve structure with 10% MR ratio with less than 500 Oe saturating field.

A ferromagnetic layer/non-magnetic layer/ferromagnetic layer sandwich structure is used to control spin configuration. For the non-magnetic spacer materials, Cu, Ru, Au, Ag, Cr, and Ta have been studied [14, 17]. For ferromagnetic materials,

Co, Fe, Ni and its alloy are available. Among them, Co/Cu multilayer is selected for this study since Co/Cu is reported for the highest MR ratio [18].

There are several other factors which impact the MR ratio. Among them, the thickness of the spacer layer, the interface roughness, the number of the repetitions of layers, and current leakage through substrate are considered for the current study.

It is well known that there is exchange coupling between the two ferromagnetic layers through a non-magnetic layer. Its exchange coupling oscillates from antiferromagnetic coupling to ferromagnetic coupling depending on the thickness of the non-magnetic layer [17, 19]. In the case of the Co/Cu/Co structure, there are three peaks for antiferromagnetic coupling: 8Å, 21Å, 34Å [20, 21]. At these three thicknesses, the antiferromagnetic coupling strength has a peak value even though the overall strength decreases as the thickness increases [14]. This anti-ferromagnetic strength is very important because this strength is closely correlated with saturation field and MR ratio. Typically, the MR ratio follows the saturation field trend [22]. For example, at the 1^{st} peak (8 Å) we can get a very strong saturation field and a high MR ratio. However, strong saturation field is not appropriate for application of a GMR sensor or the current study. The saturation field decreases in the 2^{nd} peak (21 Å) and 3^{rd} peak (34Å).

Another factor which impacts GMR ratio is interface roughness. Rough interface becomes a source for inelastic electron scattering [7]. This inelastic scattering reduces the MR ratio because it is not spin-dependent. The interface roughness is primarily dependent on the film thickness and sputtering conditions, i.e.

sputtering power and pressure. It is well known that high sputtering power and low sputtering pressure increase the mobility of sputtering elements and reduce the surface roughness of the film.

The 3rd factor is the number of the repetitions of layers. As the repeated number increase, the MR ratio generally increases because the probability of spin-dependent scattering increases [7]. However, the increasing repetitions of layers increase the roughness of the films too. Therefore, there is an optimum number to compensate the two effects.

The last factor is the leakage through Si substrate. The current leakage through the substrate will reduce the MR ratio. Intrinsic Si wafer has relatively high electric resistivity compared to metals. Typical electrical resistivity of intrinsic Si wafer is about 640 Ωm. Commercial Si wafer is usually doped with B or P to make a semiconductor. Since the electric resistivity of doped Si wafer is highly dependent on the doping concentration, its range is very wide as 1×10^{-5} ~ 0.6 Ωm [23].

In order to study the feasibility of leakage through the Si substrate, electrical measurement procedure is investigated. For electrical resistivity measurement, the spin-valve sample is patterned as a shape of four-point of probe using a photomask as shown in Figure 2-3. To measure electric resistance, electric current is applied through the two pads located at the end and the voltage across the two inside pads is measured. Since the pad area is much larger than the cross-sectional area of the bridge, the resistances of the pad area and the bridge are comparable.

(a)

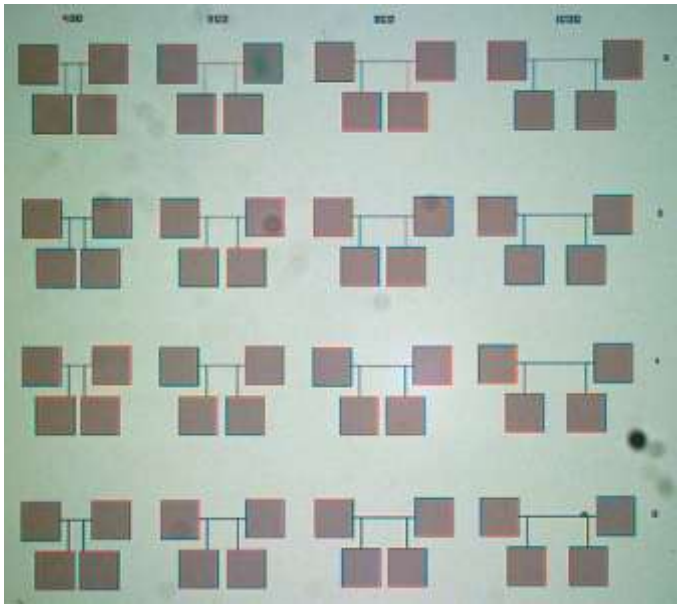

(b)

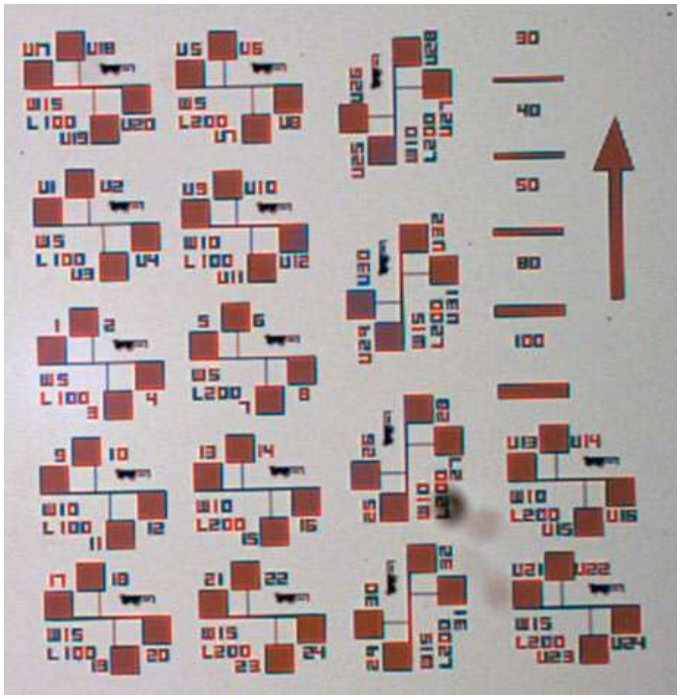

Figure 2-3 Four-point probe pattern for electrical resistance measurement (a) 1st mask, Pad: 400×400μm, length: 400, 600, 800, 1000 μm, width: 2, 3, 4, 8 μm, (b) 2nd mask, Pad: 200×200μm, length: 100, 200 μm, width: 5, 10, 15 μm

The ratio of the resistance of the bridge and the pad can be roughly calculated in the following equation.

$$\frac{R_{bridge}}{R_{pad}} = \frac{\rho_b \frac{L}{A_b}}{\rho_p \frac{L}{A_p}} = \frac{\rho_b A_p}{\rho_p A_b} \qquad 2\text{-}9$$

Here, the resistivity of the bridge, ρ_b is assumed as 1×10^{-7} Ωm and that of the pad, ρ_p is assumed as 1×10^{-3} Ωm. The cross-sectional area of the bridge (width 10μm, the film thickness 50nm) will be 0.5 μm^2. The cross-sectional area of the pad will be $200\times200=4\times10^4$ μm^2. Then, the resistance ratio of the bridge to pad is as follows.

$$\frac{R_{bridge}}{R_{pad}} = \frac{\rho_b A_p}{\rho_p A_b} = \frac{(1\times10^{-7})\times(4\times10^4)}{(1\times10^{-3})\times0.5} = 0.8 \qquad 2\text{-}10$$

The roughly calculated resistance of the bridge is in the same order of the pad. Therefore, it is possible for some portion of applied current pass through the Si substrate and reduces the MR ratio. This current leakage can be typically prevented by using an oxide coated Si wafer.

Impurity located at the interface also can impact significantly the MR ratio. For example, unexpected impurity can be introduced between layers in a vacuum chamber during break between two different sputtering processes, which occurs in the CVC sputtering system at the cleanroom at Carnegie Mellon University.

In order to obtain low saturation field for the spin-valve structure, we used different coercivities of the ferromagnetic layers instead of antiferromagnetic coupling between the ferromagnetic layers. The antiferromagnetic coupling usually results in high saturation field. Different coercivities of the ferromagnetic layers can make the relative orientation change of the magnetization in the ferromagnetic multilayers [7, 14]. If two ferromagnetic layers have different coercivities, the magnetic

configuration will be in the field range of the two coercivities. Therefore, the saturation field will be much lower than that in antiferromagnetic coupled structure.

3 Experimental details for spin-dependent heat transport measurement

In order to use a three-omega (3ω) or steady-state joule heating method for thermal measurement, a thermally isolated bridge structure is required. We developed a MEMS process for the suspended bridge structure. In addition, we set up a three-omega and steady-state joule heating measurement system. The detail experimental procedures are addressed in following sub-sections.

3.1 Thin film deposition

All the film layers constituting a spin-valve structure were deposited on 3" Si wafer or 1μm thick oxidized Si wafer or 27nm thick oxidized Si wafer using a CVC Connexion 6-Target Sputtering System installed at the cleanroom in Carnegie Mellon University [24]. The system has 6 sputtering targets, 12" or 5" diameter, and is equipped with a loadlock. Also this system is available to apply perpendicular or parallel magnetic field on substrate. The deposition process is computer-controlled using programed recipes. The base pressure in the main chamber is maintained below 1.0×10^{-8} Torr.

For the spin-valve structure, we used Ta/$[Co/Cu/Co]_N$/Ta/oxide/Si substrate structure. The detail deposition procedure is addressed as follows. 2 ~ 5nm thick Ta layer was deposited as a wetting layer on a Si or oxide substrate. It is well known that a few nanometer thick sputtered Ta forms an amorphous film. Thus this layer prevents

the formation of texture from a Si (100) substrate. Figure 3-1 shows the Transmission Electron Microscope (TEM) image of Ta film. The TEM image was taken using the FEI Tecnai F20 Field Emission TEM at the J. Earl and Mary Roberts (JEMR) Microstructural Characterization Facility [25]. The 2nm thick Ta layer shows an amorphous form as expected. Another role of Ta layer is a barrier against Cu diffusion into Si substrate [26].

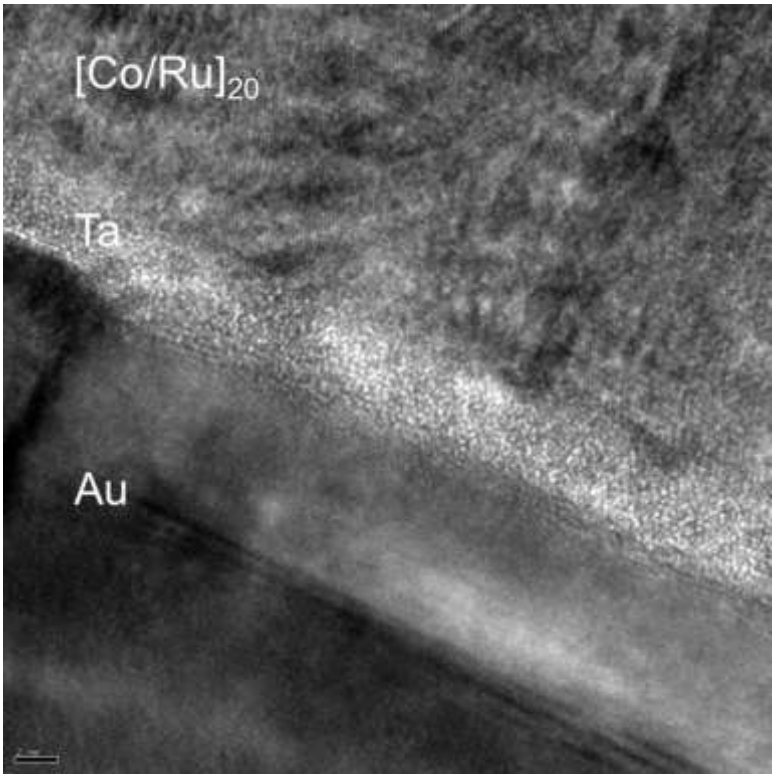

Figure 3-1 TEM bright field image of cross-section of $[Co/Ru]_{20}$/Ta/Au; Ta layer does not have a lattice image, which indicates an amorphous form.

After the Ta layer deposition, Co/Cu/Co multilayers were deposited by sputtering Co and Cu films. The thickness and number of Co/Cu/Co tri-layers was optimized to achieve a high MR ratio. The thickness varied from 10 Å to 40 Å for Co

and 8 Å to 60 Å for Cu. The number of tri-layers, N, was altered from N = 3 to N = 15.

It is well known that the interface roughness of a ferromagnetic multilayer is closely relevant to a MR ratio [7, 14] as described in Chapter 2.2. However, it is not easy to quantitatively measure the interface roughness. One of the typical methods is to see the cross-sectional TEM image of the interface. However, from the TEM image we can get only qualitative and local area information of the interface roughness even though a lot of effort is required for preparing samples and operating a TEM. Instead, we measured the surface roughness of each single film depending on sputtering conditions using Atomic force microscope (AFM).

The AFM measurement was conducted using a Veeco Scanning Probe Microscope System, which consists of a Dimension 3100 SPM with a Dimension hybrid closed loop scan head and a Nanoscope IVa SPM control station in the JEMR Microstructural Characterization Facility [25] . The system is mounted on an air table for vibration isolation and features an enclosure for isolation from ambient noise and temperature variations. Table 3-1 shows the surface roughness depending on the sputtering conditions, which were measured by the AFM.

Table 3-1 RMS roughness for Cu, Co, NiFe depending in sputtering conditions, measured by AFM

Materials	Sputtering power (Watt)	Sputtering pressure (mTorr)	Rms roughness (Å)	Sputtering rate (Å/sec)
Cu	40	2	11.5	1
Cu	40	3	11.0	1
Cu	40	5	12.5	1
Cu	60	3	10.7	1.5
Cu	80	3	12.6	2
Co	40	3	7.4	1
Co	40	5	12.4	1
NiFe	80	3	15.5	1

Figure 3-2 shows AFM images of Cu and Co films for some sputtering conditions. The surface roughness of a thin film is relevant to the grain size of the film [27]. Grain boundary would be a main cause of the surface roughness. In order to make small grains, high sputtering power and low sputtering pressure are desirable. However, there is a limitation for this sputtering condition. Increasing sputtering power and decreasing sputtering pressure usually result in increasing sputtering rate. If the sputtering rate is more than 2 Å/sec, the exposure time for plasma will be less than 5 seconds for some layer since the thickness of each layer is only 8-30Å. This short exposure time might result in discontinuous film structure. Therefore, the margin for optimizing sputtering condition is very limited.

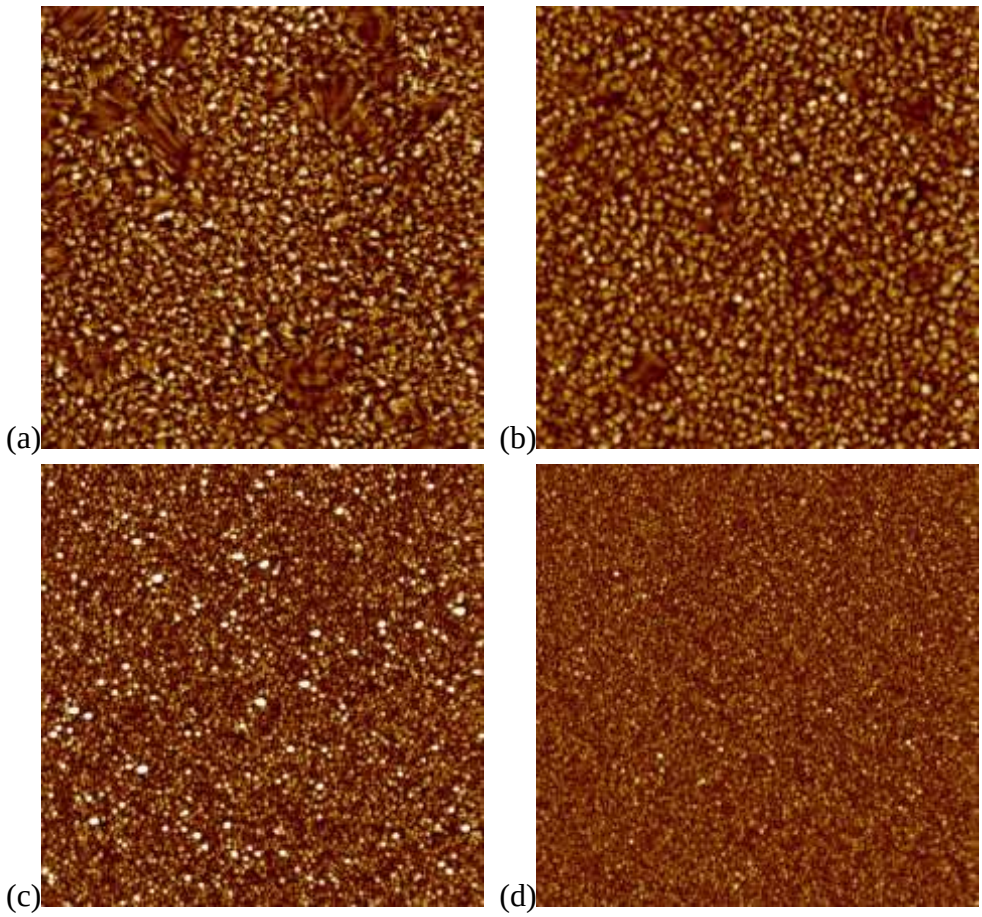

Figure 3-2 AFM images of surface roughness of Cu and Co films with different sputtering power and pressure: (a) Cu: 80W, 3mT (b) Cu: 60W, 3mT (c) Co: 40W, 5mT (d) Co: 40W, 3mT. Each image was scanned over a 2μm×2μm area.

After the Co/Cu/Co multilayer deposition, a 3-5nm thick Ta layer was deposited as a cap layer to protect the multilayer from oxidation.

In addition, in the case of fabricating a bridge structure, deposition of Au film on pad areas is required for wire-bonding. 200nm thick Au film was deposited using a Perkin Elmer 6J Sputtering System. To improve adhesion between Au and other materials, very thin Ti or Cr films are usually deposited. For the current study, 5nm thick Ti film was deposited with Au film for the adhesion layer.

The sputtering process of Co and Cu film was evaluated under different Ar

pressures from 2 to 5 mTorr and DC plasma powers from 40 to 80 Watt in order to optimize the film quality, primarily focusing on the sputtering rate and the film roughness. The deposition rate of all sputtering conditions was examined by measuring the step height between the deposited film and the substrate at five different points in the wafer using a KLA-Tencor P-15 profilometer. Table 3-2 summarized sputtering conditions for thin films constituting the spin-valve samples.

Table 3-2 sputtering conditions for thin films constituting the spin valve samples

Materials	Power [Watt]	Pressure [mTorr]	Flow rate of Ar [sccm]	Magnetic Field	Sputtering rate [Å/sec]	Sputtering machine
Ta	100	5	50	Off	1.27	CVC
Cu	60	3	40	Off	1.5	CVC
Co	40	3	40	On	1.0	CVC
NiFe	80	3	40	On	1.0	CVC
Ti	100	5	50	N/A	2.5	6J
Au	50	5	50	N/A	8.3	6J

3.2 Procedures for Four-point probe structure

In order to measure the electric resistivity of the spin-valve samples, it is necessary to make a four-point probe structure. The four-point probe structure has two benefits comparing to un-patterned thin films. One is to define a current path. The other is to define magnetic easy axis originating from shape anisotropy [28]. The four-point probe structure was fabricated using an optical lithography processing using the fabrication facilities in a cleanroom at Carnegie Mellon University. For the

optical lithography, we used the photomasks, which is shown in Figure 2-3.

Optical lithography is a very important process for fabrication of nanoelectronic devices. The optical lithographic process makes it possible to fabricate many micro/nano scale devices. First, photoresist was spun onto the wafer where the spin-valve structured films were deposited. The photoresist was coated into a uniform thickness film with a few μm thicknesses. Upon exposure to the light of the correct wavelength, the photoresist becomes more soluble in the case of positive photoresist. Using a developer, the light exposed area of the photoresist was removed. Then the area of the film was selectively etched by ion milling while the remaining photoresist plays a role of a mask. The overall procedures are summarized using a flow chart in Figure 3-3. In addition, the cross-sectional images for each step are illustrated in Figure 3-4 for patterning processing using optical lithography.

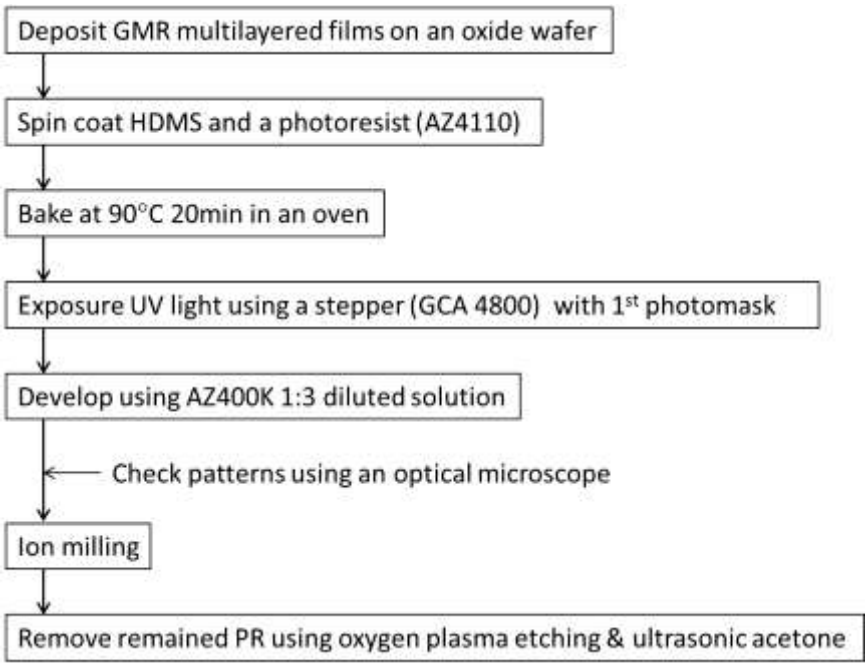

Figure 3-3 Procedures for pattering four-point probe structure

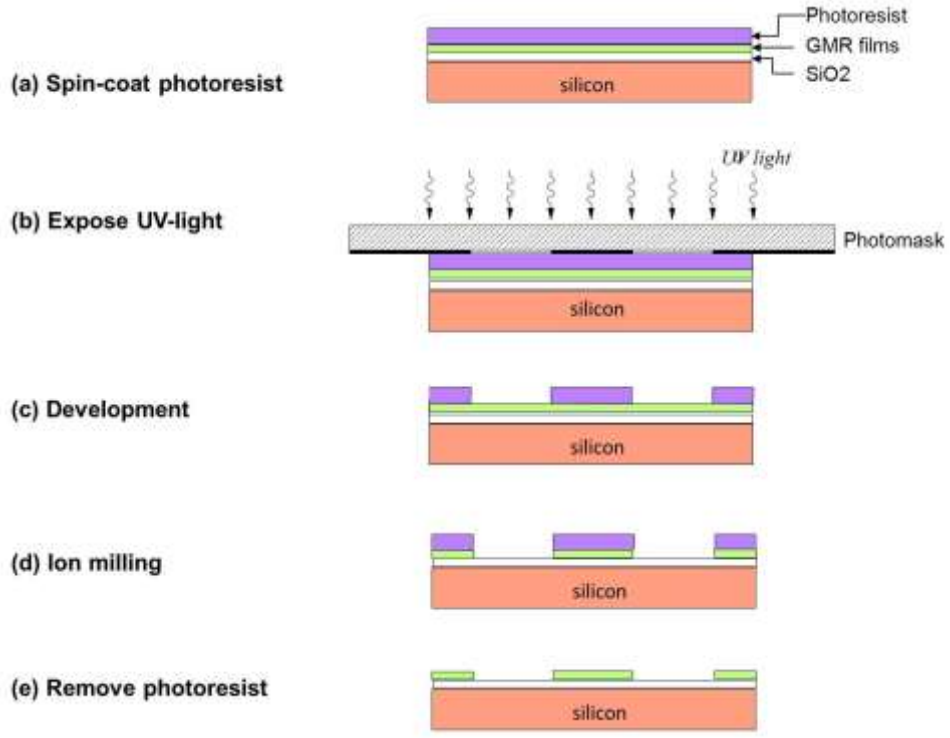

Figure 3-4 Illustrated patterning processing with optical lithography

The detail procedures for patterning processing using optical lithography are addressed as follows.

1) Surface cleaning

We usually used a 3" diameter Si wafer which is coated with 1μm thick thermally grown SiO_2. First we cleaned the surface of the wafer with a sequence of acetone, isopropanol and DI water rinse. Then, the wafer was thoroughly dried using a nitrogen-gas gun. Instead of drying the wafer using the nitrogen-gas gun, we often further clean and dry the wafer using a Semitool 870 Spin Rinser/Dryer. The spin Rinser/Dryer rinses a wafer in DI water to 15 MΩ and dries with heated nitrogen.

2) Photoresist spin-coating

After cleaning the surface of the wafer, we coated a photoresist onto the surface of the wafer. We used AZ41100 (4000rpm, 1.10μm) as the photoresist, and hexamethyldisilazane (HMDS) for adhesion of the photoresist to the surface of the wafer [29]. For coating the photoresist onto the surface of the wafer, we used the Solitect spinner at the cleanroom.

The timer of the spinner was set to 6 sec at 600rpm for spreading and then 30sec at 4000 rpm for spinning. Then, we centered carefully the wafer on the spinning chuck and turned on the vacuum to hold the wafer in place.

We dispensed a drop of HMDS onto the center position of the wafer and started the spread/spin cycle. Then, we dispensed a drop of AZ4100 onto the wafer in the same way as HMDS did.

Since both the HMDS and photoresist are liquid forms, we used a spin coating method to coat them onto the wafer. The spin coating is a method to coat a liquid form onto the wafer with relatively uniform thickness. The coated thickness is inversely proportional to the square root of the viscosity of the liquid [29]. Since the viscosity of the HMDS is very low, the coated thickness of the HMDS would be a single monolayer [29].

After coating the photoresist, we placed the wafer in a convection oven at 90°C for 20 minutes. Then, we kept the wafer to a metal holder to cool down for 1 minute. The soft baking removes a remaining solvent from the photoresist and improves the photoresist adhesion. The baking time and temperature affect the photosensitivity of the photoresist.

3) Exposure UV-light

The next step was UV-light exposure to the photoresist to generate a pattern. For the exposure, we used a GCA 4800 stepper, which is a 10 times reduction g-line stepper, operating at a wavelength of 436 nm and numerical aperture of 0.38, thus providing a theoretical resolution of 0.7μm. However, the practical resolution is about 1μm. First we loaded a 5”×5”×0.09” quartz photomask to the stepper just below a mercury arc lamp. Then, we loaded the photoresist-coated wafer on a movable stage, where is located at the bottom of the stepper. The UV-light is generated from a arc lamp, then passed through the photomask and projected down to the wafer. The projected pattern is reduced to a tenth of the original pattern size. The exposure time was 0.16-0.18 sec with focus 251. This process was repeated to make several patterns onto the wafer.

4) Development

To remove the exposed photoresist from the wafer, we used a diluted solution of developer with the ratio of 1:3. We mixed developer AZ 400K 200ml and DI-water 600ml into a glass beaker. Then, we immersed the wafer into the diluted solution and agitated the wafer for about 2 min using a wafer holder. However, the developing time was not fixed. We monitored the pattern feature of the wafer while agitating. When watching every pattern features come out, we immediately stopped agitating and immersed the wafer to a DI-wafer bath. Then, we cleaned softly the surface of the wafer using a DI-water gun and dried it using a nitrogen gas gun. The DI-water rinse and N_2 drying are needed to remove any remaining developer, and stop any chemical

processes on the wafer.

A developer removes the exposed areas of positive photoresist. The developing procedure is more critical than exposure. There are three important factors to impact the developing process: the ratio of the dilute solution, developing time, and agitating way. First, the ratio of the dilute solution is approximately 1:3, but it is not easy to mix accurate amount of the developer and the DI-water with the exact ratio. If the fraction of the developer is more than 1/4, the developing process is accelerated and hard to control the optimum developing time. If the fraction is less, the developing process takes exponentially longer. Second, the developing time is also critical to obtain a properly developed pattern. If the time is too short, the pattern will be underexposed, which means that some part of the exposed photoresist still remains. If the development time is too long, the pattern will be overexposed, small features will be completely washed away. For example, Figure 3-5 shows an overexposed pattern, which some bridge parts were disappeared. Last, the way to agitate the wafer in the developer is also sensitive to the feature of the pattern. Too much or too little agitation during developing will result in over or under developing, respectively. In addition, the processing of many wafers in one batch of developer decreases the developing rate. It is suggested to use fresh developer every time in order to get a constant result.

To check the exposure and developed conditions, we examined the developed wafer using an optical microscope (Olympus, MX80). During observing the wafer by the microscope, it is important to use a green light filter since white light will

expose the photoresist.

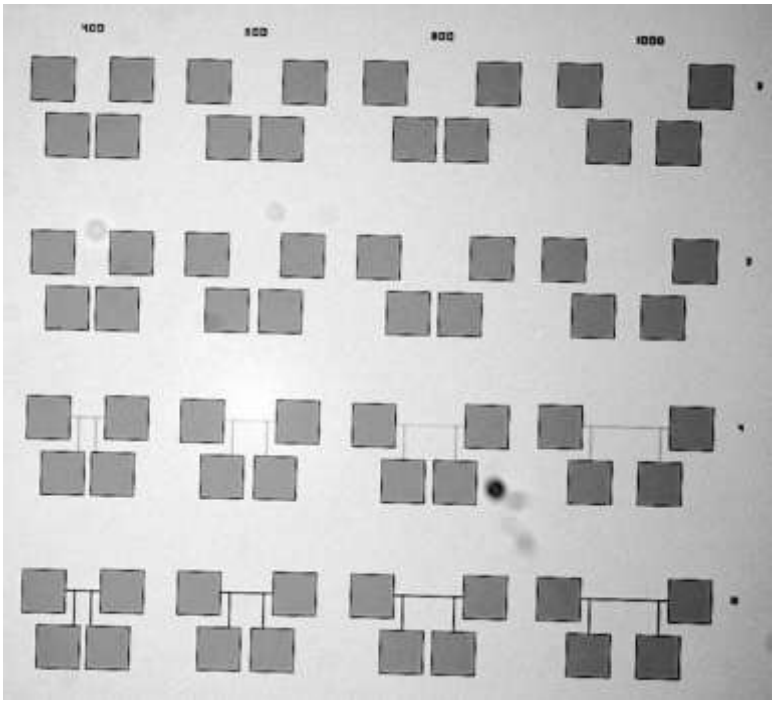

Figure 3-5 Over-developed pattern; 2μm and 3μm width lines were disappeared. 4μm width lines were partly remained and 8μm lines exist.

5) Ion milling

Following the developing process, ion milling process was proceeded to pattern the four-point probe structure to the film. A commonwealth scientific system was used for ion milling. The wafer is vaccum sealed to a siliver impregnated silicon rubber pad to make a good thermal contact between a water-cooling stage and the wafer during ion milling process. Then, the etching chamber was pumped down to the base pressure of 3×10^{-7} Torr. During the etching, the chamber pressure was typically set to 1.3×10^{-4} Torr. The sample stage was rotated and angled 22.5° in order to minimize sidewall deposition [30]. The 22.5° is the angle between incident beam and

the sample surface normal. The accelerating voltage was set to 500V and ion beam current 40mA, neutral current -002mA. The etching rate for Co is 121Å/min, Cu 234 Å/min, NiFe 120 Å/min, Ta 65 Å/min [26], SiO_2 70 Å/min.

During the ion milling process, a plasma containing Ar ions and electrons are accelerated and then neutralized by extracting electrons from a hot filament neutralizer. This neutralized beam etches materials on the surface of the wafer. The two main characteristics of the ion milling are anisotropy and low selectivity. A wide range of materials can be etched anisotropically, making steep wall angles.

6) Remove Photoresist

After the ion milling process, the remaining photoresist was removed by oxygen-plasma and ultrasonic vibration treatment in acetone. Using the IPC Plasma etcher (international plasma corporation), we first soften the remaining photoresist by exposing oxygen-plasma to the wafer. We loaded the wafer with a wafer holder into the etcher. At 1Torr, plasma was generated using oxygen gas. The acceleration voltage was 100 V and the process time was 2 min. We adjusted the impedance matching to make the reflectance voltage to be zero. This plasma process softens the photoresist, which was harden during the ion milling, thus promotes removing the photoresist in an acetone. After plasma treatment, the wafer was immersed in acetone with ultrasonic vibration treatment for 10 minutes to fully remove the photoresist.

After all, we successfully patterned the four-point probe structure of a spin-valve structured film, which is shown in Figure 3-6.

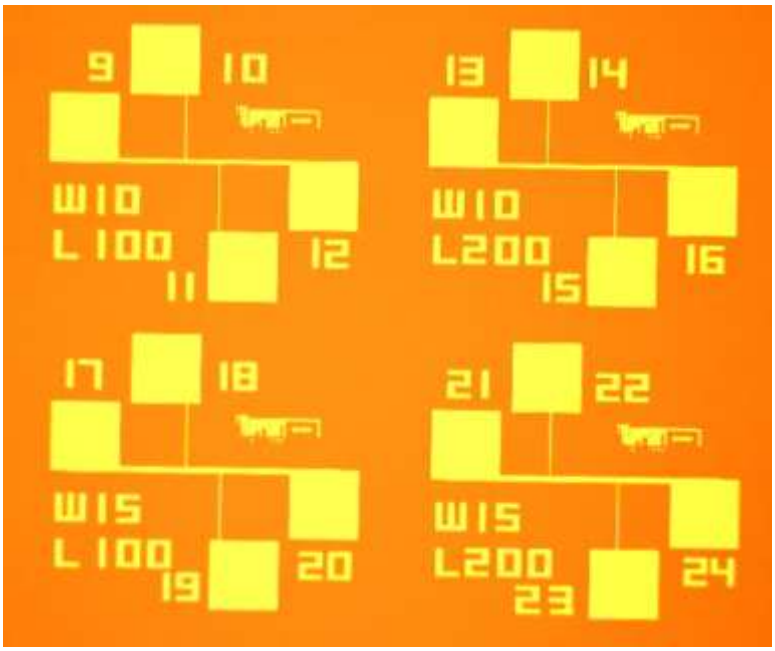

Figure 3-6 Optical image of four-point probe structure of the spin-valve structured film after ion milling

3.3 Procedures for bridge structure

For thermal measurement, we need a thermally isolate rod, so called a suspended bridge structure. For this purpose, we need two further processes. One is to deposit Au film onto the probe regions for wire bonding, and the other is to undercut Si to release the bridge from the Si substrate.

1) Au deposition onto the probe regions

Before undercut processing of Si, Au was deposited onto the probe regions of the four-point probe structure. The four-point probe structured wafer was spin-coated with AZ4210 photoresist (4000rpm, 2.1μm). The AZ4210 was spread at 600 rpm for 6 sec and spin-coated at 4000 rpm for 60 sec. This thicker photoresist makes easy for further lift-off process. After photoresist coating, the wafer was baked at 90°C for 20

min in an oven. Then, the sample was exposed for 0.18 seconds using the GCA4800 stepper with the second photomask. The second photomask has patterns of probe regions, as shown in Figure 3-7. The exposed wafer was developed with the 1:3 diluted AZ400K developer solution.

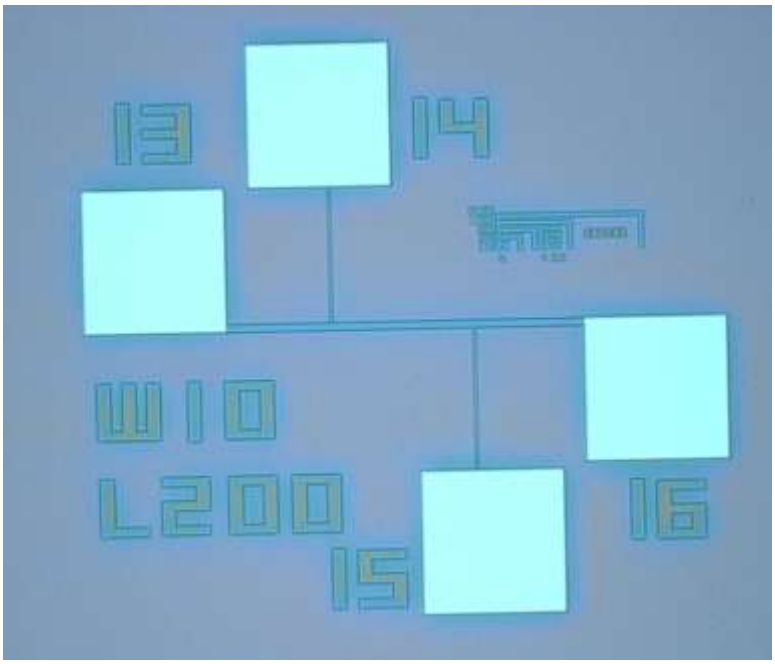

Figure 3-7 Second mask pattern, which is overlapped onto the 1st mask pattern

Then, Ti(5nm)/Au(200nm) was sputtered using Perkin Elmer 6J Sputtering System. The base pressure was 3×10^{-7} Torr and the process pressure was 5mTorr. The sputtering power was 100 Watt for Ti and 50 Watt for Au. The sputtering time was 20 seconds for Ti, 240 seconds for Au. The 5nm thick Ti works for an adhesion layer between Au and other materials. After depositing Au film, the wafer was ultrasonic vibration treatment in acetone for at least 3 hrs to wash off the photoresist with Au film. After this lift-off process, Au film located at the probe regions was

remained, where photoresist did not exist before the ultrasonic treatment in acetone. It is important to fully remove the photoresist on the probe regions before sputtering Au through the developing process. If the photoresist was remained there, the Au film would be also removed with the photoresist through ultrasonic treatment in acetone. Mild scrubbing with a cotton swab in acetone was performed to remove the side wall of the Au pad after the lift-off process. Overall processes are summarized using flow charts in Figure 3-8.

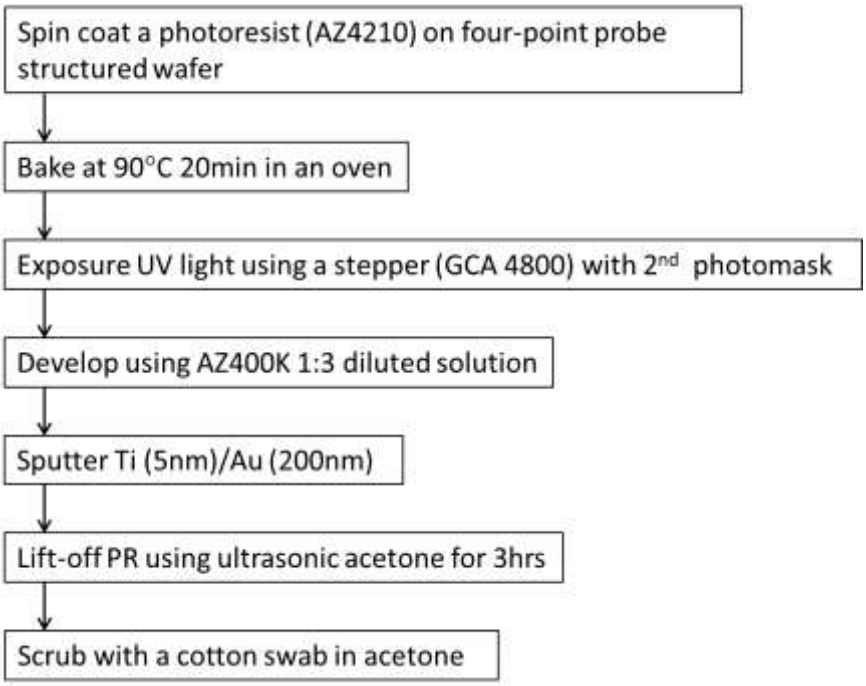

Figure 3-8 Procedure for Au sputtering on the pad area

2) Undercut Si using XeF_2

Following processing is to undercut Si substrate beneath the bridge regions. The wafer was spin-coated with AZ4110 photoresist. The AZ4110 was spread at 600 rpm for 6 sec and spin-coated at 4000 rpm for 30 sec. HMDS was not used for this

process. After PR coating, the sample wafer was baked at 90°C for 20 min in an oven. Then, the sample was exposed UV-light for 0.18 seconds by using the GCA4800 stepper with the third photomask. The pattern of the third photomask is shown in Figure 3-9. The exposed wafer was developed with the diluted solution with AZ400K developer. Then, ion milling process was performed to dig holes at the sides of the bridge area as shown in Figure 3-9.

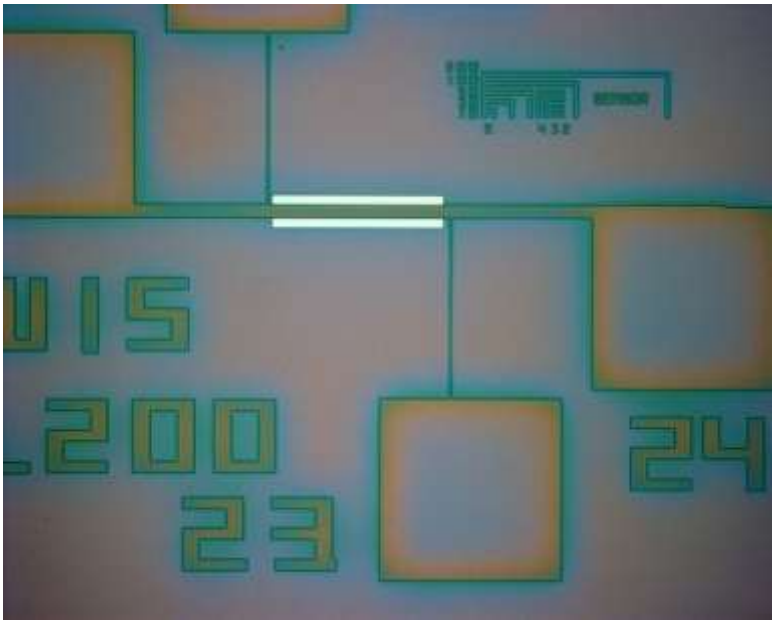

Figure 3-9 3rd mask pattern, which is overlapped to 1st mask pattern.

For making the holes, it is important to etch out both metal films and SiO_2 until Si exposed since XeF_2 has a high etching rate for Si but a low etching rate for SiO_2. After the ion milling process, Si beneath the bridge regions was undercut using Xenon diflouride (XeF_2) gas. Overall procedure for releasing the bridge structure is summarized using flow charts as shown in Figure 3-10.

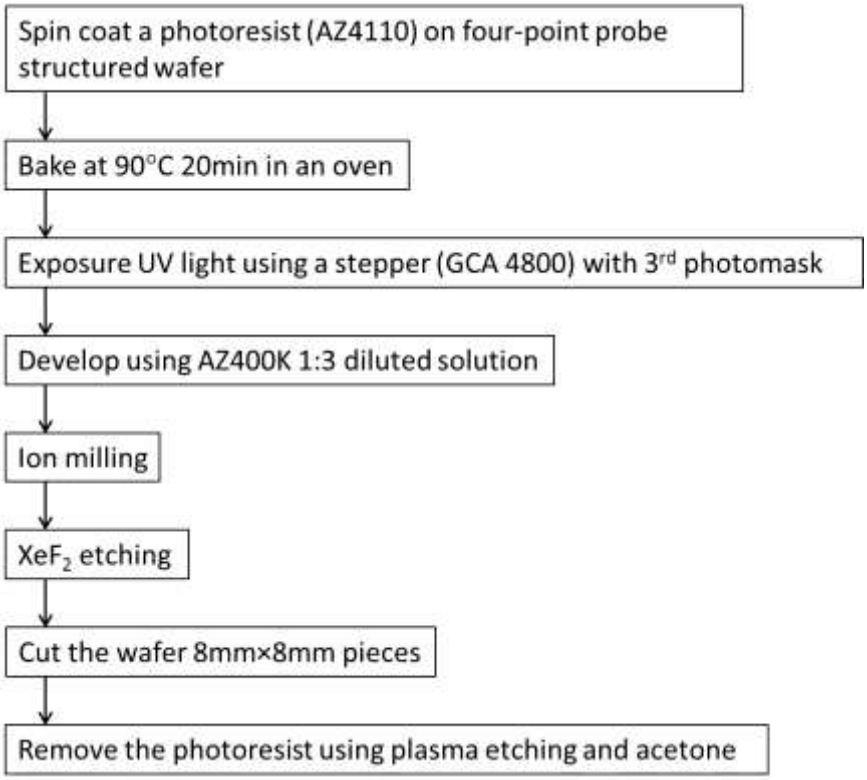

Figure 3-10 Procedure of undercutting Si substrate to release the bridge structure

The XeF_2 etching was performed using a e1 series Xetch® Xenon Difluoride Etching System [31]. The wafer was placed in the etching chamber and the system was a computer-controlled to the following settings:

Table 3-3 Etching settings for XeF_2 etching

Setting	Value
Number of Cycles	4
Etch Time	60 sec
XeF_2 Pressure	3.0 Torr
N_2 Pressure	0 Torr

We used a pulse method, which the wafer is alternatively exposed to XeF_2 gas

and vacuum. Since XeF_2 etching is isotropic, it etches out simultaneously vertical direction and horizontal direction. We need to set optimum etching condition to etch Si substrate underneath the bridge regions in order to release the bridge from Si substrate. The etching condition was controlled using the number of cycles.

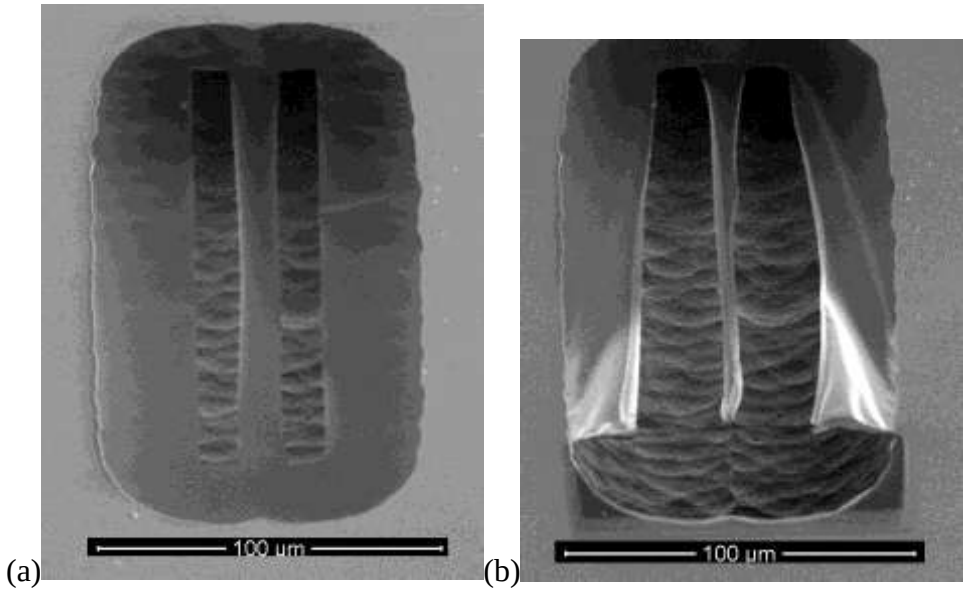

Figure 3-11 SEM images of 10µm wide two parallel holes after XeF_2 etching (a) top view before cross-cutting by Gallium ion and (b) cross-sectional view after the cross-cutting

Figure 3-11 shows the results of XeF_2 etching using a FEI NOVA 600 Focused Ion Dual Beam scanning electron microscopy (SEM). This etch-deposit system combines precise Focused Ion Beam (FIB) and ultra-high resolution field emission SEM. The sample was the 27nm thick oxide coated Si wafer. The wafer was patterned holes using the 3rd photomask and ion milling. Then, Si substrate was etched using XeF_2 as shown in Figure 3-11(a). Since the XeF_2 has high selectivity of Si with respect to SiO_2, only underneath Si was etched and SiO_2 films remained. In order to check

whether the bridge is released from the Si substrate, the hole was cross-cut by Gallium ion using the FIB as shown in Figure 3-11(b), which shows clearly that the bridge is released.

The bridges were designed with a width of 5μm, 10μm, 15μm and a length of 100μm and 200μm. The XeF_2 etching condition should be satisfied for all features. Figure 3-12 compares the etching results with different width when the XeF_2 etching is not fully completed. In the case of width 15μm, the bridge was not released, while the bridge of 10μm width was released.

(a)

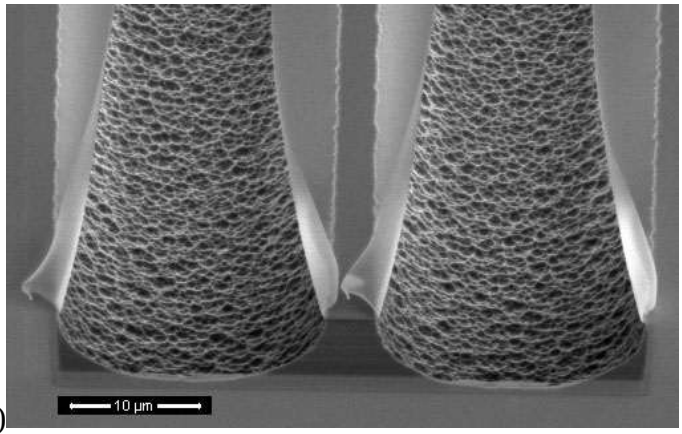

(b)

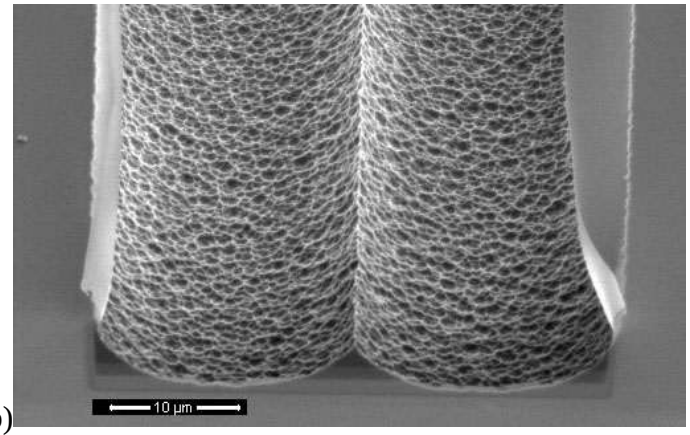

Figure 3-12 SEM images for (a) the distance of the two hole was 15μm and (b) the distance was 10μm. In the case of (a) the bridge area is still connected with the Si substrate, meanwhile in the case of (b) the bridge area is released from the Si substrate.

XeF_2 etching is highly selective to silicon with respect to metals, photoresist, and silicon dioxide [32]. The etching rate and selectivity for some materials are summarized in Table 3-4 After [32]. In addition, the XeF_2 etching is isotropic. The etching rate does not depend on the crystal plane of silicon. Primary chemical reaction between XeF_2 and silicon is following [32]:

$2\ XeF_2 + Si \rightarrow 2\ Xe\ (g) + SiF_4\ (g)$

The XeF_2 and SiF_4 gas are very dangerous for health. Breathing them can burn the respiratory tract.

Table 3-4 Etching rate and/or selectivity for XeF_2

Material	Etch rate and/or selectivity
Si	~2μm/min
SiO_2	Selectivity- 2000:1
Photoresist	Selectivity- ∞:1
Ta, Cu, Au	Etching rate is expected to be low, but no information
tape	Good masking layers

3) Remove remaining photoresist

The very last step is to remove the remaining photoresist from the wafer. Before removing the photoresist, the wafer was cut to 8mm×8mm pieces to fit into a chip carrier for wire-bonding. Since the bridge structure was released, the structure can be easily broken by any external stress. Therefore, we cannot use ultrasonic

vibration process in acetone to remove the photoresist, which will give mechanical stress to the bridge.

Another way to remove the photoresist is using plasma-etching process. The Oxygen-plasma etching at 250Watt for 15min or 150Watt for 30 min can remove fully the remaining photoresist. However, after the etching process, the bridges were broken. During the etching process, the temperature of the chamber was increased to 150 - 250°C. Thermal stress might be the cause for breaking the bridge.

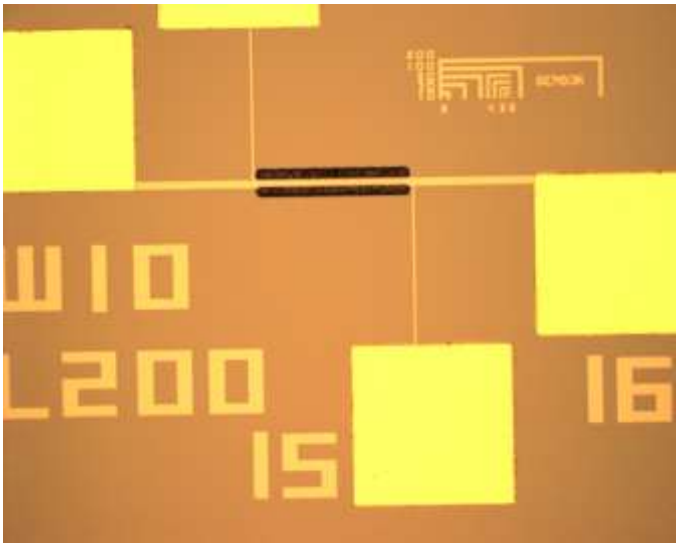

Figure 3-13 Optical microscope image of top view of the released bridge structure

We should not give any mechanical or thermal stress to the bridges while removing the remaining photoresist. For this purpose, oxygen-plasma at 100 Watt for 2min was exposed to soften the photoresist first. The temperature increase was about 20°C. Then the chips were put into the acetone for at least 3hrs without ultrasonic treatment. Then, the chip was dried softly using a nitrogen-gas gun. Using this process we successfully removed the photoresist without damage to the released bridge, which

is shown in Figure 3-13.

Figure 3-13 shows a top view of the optical microscope image of the four probe configuration and its bridge. The sample chip was placed in a 40-pin LCC chip carrier and wire-bonded to provide electrical access to the suspended beams. The LCC chip carrier was packaged in a socket that was attached to a circuit board, which is shown in Figure 3-14.

(a)

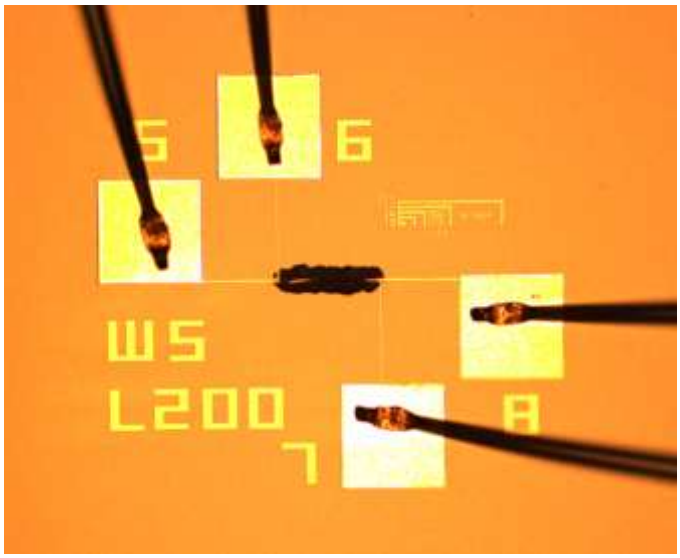

(b)

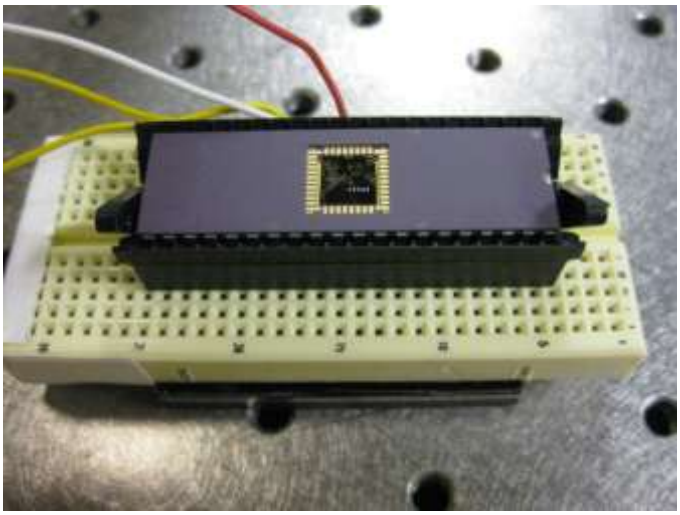

Figure 3-14 (a) A sample chip is wire-bonded to LCC chip carrier (b) The chip carrier is packaged in a socket which is attached to a circuit board.

3.4 Setup for Steady-state joule heating measurement

The electric resistance of the suspended beam was measured using a four-point probe measurement technique through current and voltage access pads. We used the four-point probe method to avoid measurement error due to contact resistance. After forcing a DC current to flow into the bridge structure, we measured the voltage drop across the bridge structure with a voltmeter. From the measurements of the voltage across the bridge, the resistance was determined using Ohm's Law.

The measurement was performed by placing the entire experimental setup inside the gap of an electromagnet, which provides a uniform magnetic field. The magnetic field was applied along the length of the bridge and its strength was swept from +650 Oe to -650 Oe. The field strength in the gap was monitored by placing a Hall probe above the sample. Figure 3-15 shows the measurement setup.

For both typical electrical resistance measurement and steady state joule heating measurement, DC current was applied to the bridge and the voltage was measured across the bridge using the four-point probe configuration. The difference between typical electric resistance measurement and steady-state joule heating measurement is that the bridge should be thermally isolated and electrical resistance be measured with a series of current intensity for the steady-state joule heating method. In another word, an I-V curve was measured for steady-state joule heating method. From the I-V curve, the resistance was calculated using Ohm's law. The

temperature increase stems from joule heating since electric current is applied to the bridge.

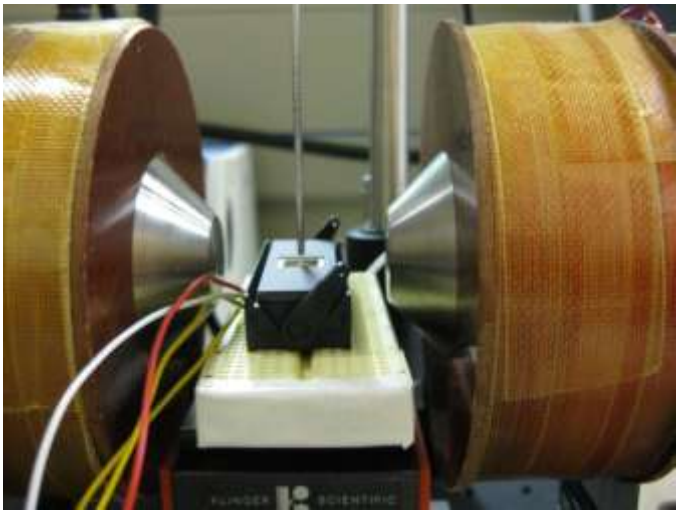

Figure 3-15 Electrical measurement setup inside an electromagnet; Hall probe is located just above the sample.

Figure 3-16 illustrates a schematic of the measurement setup for steady state joule heating method. Using Keithley 2400 Sourcemeter, DC current was applied between the two outside probes. The voltage between the two inside probes was measured using Agilent 34401A multimeter. Bipolar DC current was applied to a custom-made electromagnet to generate a magnetic field. The magnetic field was monitored using a Hall probe and Bell 620 Gaussmeter. While the magnetic field was gradually changed from -650 Oe to 650 Oe with 14 Oe step, a I-V curve was measured every magnetic field step. For the I-V curve, DC current was applied from 0.1mA to 1mA with 0.05mA step. In order to make steady-state, 10 msec was waited before voltage measurement after current was induced. Before calculating the electrical resistance using Ohm's law, the linear relationship of the I-V curve was

verified. Every measurement is computer controlled using a Labview program.

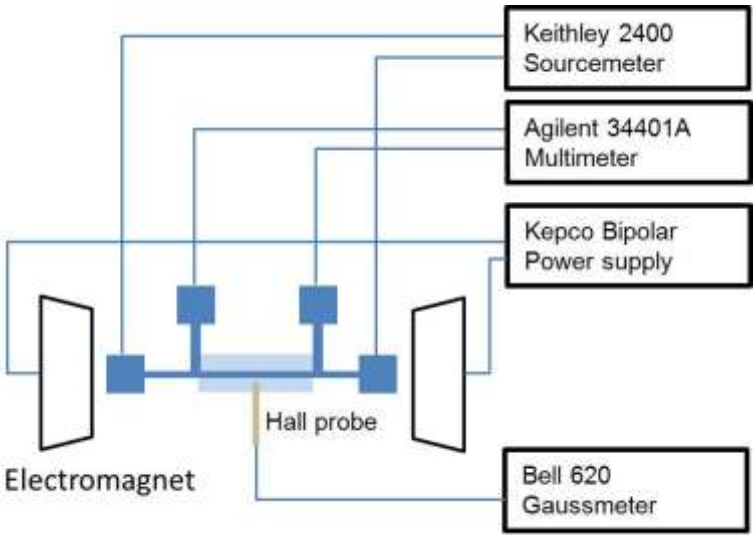

Figure 3-16 Schematic of steady-state joule heating measurement Setup

3.5 Analysis for Joule heating

The average temperature rise of the bridge can be calculated by solving a heat diffusion equation in the bridge structure. The calculation was conducted based on an one-dimensional heat conduction with the following boundary conditions. (1) The bridge between the two voltage probes is suspended to allow the temperature fluctuation, (2) The end-supports of the bridge are kept at the ambient temperature, and (3) Heat loss from the surface of the bridge, due to the thermal radiation and gas convection, are negligible. (4) The temperature of the cross-section of the bridge is uniform (lump approximation).

For the first boundary condition, we checked the bridge structure using an optical microscopy and SEM. In addition, we confirmed the suspended condition using an I-V curve. When the bridge structure is not suspended, the generated heat is

dissipated through a Si substrate. Therefore, the electric resistance does not increase with applied current but is saturated. If the bridge structure is suspended, the heat is dissipated only through the probe region. Therefore the electric resistance is linearly proportional to applied current square.

For the second boundary condition, we changed 1μm thick oxide to 27nm thick oxide since oxide layer plays a role of insulating heat transport.

For the third boundary condition, radial heat loss through radiation was calculated. The radial heat loss can be expressed as follows [33].

$$q = \varepsilon A\sigma(T_s^4 - T_\infty^4) = 1.3\times10^{-7} Watt \qquad 3\text{-}1$$

For the calculation, the emissivity of a black body was used.

Also, the heat loss through gas convection can be expressed as follows [33].

$$q = hA(T_s - T_\infty) = 3.0\times10^{-7} Watt \qquad 3\text{-}2$$

Here, the typical value of the convection heat transfer coefficient of air, h=15W/m^{2}K was used for the calculation. Under these assumptions, the following one-dimensional heat diffusion equation can be solved.

$$\rho C_p \frac{\partial}{\partial t}T(x,t) - K\frac{\partial^2}{\partial x^2}T(x,t) = \frac{I^2 R}{vol} \qquad 3\text{-}3$$

where ρ, C_p, K, and R represent the density, specific heat, thermal conductivity and electric resistance of the bridge, respectively. *vol* represents the volume of the bridge and I applied current.

If we assume steady-state, Equation 3-1 can be reduced [34] as follows.

$$K\frac{\partial^2}{\partial x^2}T(x,t)+\frac{I^2R}{vol}=0 \qquad 3\text{-}4$$

With the boundary condition

$$T(x\pm\frac{L}{2})=T_0 \qquad 3\text{-}5$$

where L is the length of the bridge and T_0 is ambient temperature.

Since the resistance of metals is linearly proportional to the temperature change [35], the resistance of the bridge can be expressed as follows.

$$R=R_0+\frac{dR}{dT}\Delta T \qquad 3\text{-}6$$

$$R=R_0[1+\frac{1}{R_0}\frac{dR}{dT}\Delta T] \qquad 3\text{-}7$$

Let's introduce a new variable θ.

$$\theta=1+\frac{1}{R_0}\frac{dR}{dT}\Delta T=1+\gamma(T-T_0) \qquad 3\text{-}8$$

Here, γ is the temperature coefficient of resistance.

$$\gamma=\frac{1}{R_0}\frac{dR}{dT} \qquad 3\text{-}9$$

If θ is substituted into Equation 3-2, Equation 3-2 becomes

$$\frac{\partial^2\theta}{\partial x^2}+m^2\theta=0 \qquad 3\text{-}10$$

With the boundary condition

$$\theta(x\pm\frac{L}{2})=1 \qquad 3\text{-}11$$

Here

$$m^2 = \frac{I^2 R_0 \gamma}{K \cdot vol} \qquad 3\text{-}12$$

The general solution of this 2nd order ordinary differential equation 3-7 is obtained [36] as follows

$$\theta = A\cos(mx) + B\sin(mx) \qquad 3\text{-}13$$

Constant A and B can be obtained by using the boundary condition 3-9.

$$\theta(x) = \frac{\cos(mx)}{\cos(mL/2)} \qquad 3\text{-}14$$

This solution indicates that temperature change along the length of the bridge follows a cosine function.

Since the measured resistance is the average resistance over the bridge, the average temperature of the bridge ought to be calculated. The average temperature can be calculated by integrating Equation 3-12 over the length of the bridge and then dividing by the length as follows.

$$\theta_{avg} = \int_{-L/2}^{L/2} \frac{\cos(mx)}{\cos(mL/2)} dx / L \qquad 3\text{-}15$$

Hence, the average temperature can be expressed as:

$$\theta_{avg} = \frac{2}{mL}\tan(mL/2) \qquad 3\text{-}16$$

From Equation 3-6,

$$\theta_{avg} = 1 + \gamma(T_{avg} - T_0) \qquad 3\text{-}17$$

$$T_{avg} = T_0 + \frac{\theta_{avg} - 1}{\gamma} \qquad 3\text{-}18$$

$$T_{avg} = T_0 - \frac{1}{\gamma}[1 - \frac{2}{mL}\tan(mL/2)] \qquad 3\text{-}19$$

Then, the temperature increase due to joule heating is as follows

$$\Delta T = T_{avg} - T_0 = \frac{1}{\gamma}[\frac{2}{mL}\tan(mL/2) - 1] \qquad 3\text{-}20$$

By substituting Equation 3-18 into Equation 3-5, the average resistance of the bridge can be obtained as follows.

$$R = R_0[1 + \gamma\Delta T] = R_0\frac{2}{mL}\tan(mL/2) \qquad 3\text{-}21$$

Also, by substituting Equation 3-18 into Equation 3-4, the resistance change can be obtained as follows.

$$\Delta R = R - R_0 = R_0[\frac{2}{mL}\tan(mL/2) - 1] \qquad 3\text{-}22$$

Equation 3-20 is the analytical solution for the steady-state joule heating. We can obtain the thermal conductivity K by fitting experimental electrical resistances with Equation 3-20 if we know R_0 and γ.

Equation 3-20 is obtained by neglecting time varying term of Temperature with assumption of steady-state. In order to verify this assumption, the temperature increase in unsteady-state condition is also examined as follows.

Let's introduce another variable *u(x, t)* = T(x, t) – T_0. Then, Equation 3-1 can be expressed as follows.

$$u_t - \alpha u_{xx} - C_1 u = C_2 \qquad 3\text{-}23$$

With the boundary conditions

$$u(0,t)=0, u(L,t)=0 \qquad (t \geq 0) \tag{3-24}$$

$$u(x,0)=0 \qquad (x \in (0,L)) \tag{3-25}$$

where α = $K/\rho C_p$, thermal diffusivity (m^2/s), C_1 = $(I^2/vol)(dR/dT)$, C_2 = I^2R_0/vol, respectively.

Equation 3-21 is a one-dimensional heat diffusion equation. However, the Laplace transformation method cannot be applied to solve this partial differential equation since the method of separation of variables cannot be applied here. For the Laplace transformation method, a partial differential equation ought to be transformed to two linear ordinary differential equations by applying the method of the separation variables [36]. In order to apply the method of separation of variables, C_1 and C_2 must be zero, but we cannot neglect them in this study.

Another way to get an analytical solution for a partial differential equation is the Fourier transformation method. The variable *u(x, t)* can be Fourier transformed as follows.

$$u(x,t)=\frac{1}{\sqrt{2\pi}}\int_{-L/2}^{L/2} U(\omega,t)e^{i\omega x}d\omega \tag{3-26}$$

$$U(\omega,t)=\frac{1}{\sqrt{2\pi}}\int_{-L/2}^{L/2} u(x,t)e^{-i\omega x}dx \tag{3-27}$$

Here, U(ω, t) is the Fourier transform of *u(x, t)*. Then Equation 3-21 becomes as follows.

$$\frac{1}{\sqrt{2\pi}}\int_{-L/2}^{L/2}\left[\frac{\partial U(\omega,t)}{\partial t}+\mu\omega^2 U(\omega,t)-C_1U(\omega,t)\right]e^{i\omega x}dx=C_2 \tag{3-28}$$

If C_2 can be neglected (C_2=0), Equation 3-26 can be simplified as follows.

$$\frac{\partial U(\omega,t)}{\partial t} + \mu\omega^2 U(\omega,t) - C_1 U(\omega,t) = 0 \qquad 3\text{-}29$$

Since Equation 3-27 is a linear ordinary differential equation, we can solve it. However, C_2 cannot be neglected in this study. Therefore, the Fourier transformation method also cannot be applied for this study. Instead, we tried to analyze the partial differential equation using a numerical method without any unreasonable assumption.

Finite difference methods are well established for the one-dimensional heat equation on a finite interval with internal heat source and Dirichlet boundary conditions at both ends [37]. If we discretize Equation 3-21 by using the forward difference formula for u_t and the central difference formulas for u_{xx}, we get the forward-time central-space scheme [37]:

$$\frac{u(x_i,t_{j+1}) - u(x_i,t_j)}{k} = \alpha \frac{u(x_{i+1},t_j) - 2u(x_i,t_j) + u(x_{i-1},t_j)}{h^2} + C_1 u(x_i,t_j) + C_2 \qquad 3\text{-}30$$

Here x- and t-coordinates are equally spaced with h and k, respectively. The forward-time central-space method is stable when the following stability condition is met.

$$\mu = \alpha \frac{k}{h^2} \le 0.5 \qquad 3\text{-}31$$

Using the parameter μ, Equation 3-28 can be expressed in the following simplified form:

$$u_{i,j+1} = (1 - 2\mu + C_1 k)u_{i,j} + \mu[u_{i+1,j} + u_{i-1,j}] + kC_2 \qquad 3\text{-}32$$

Using Equation 3-32 with Matlab, the temperature increase in the bridge due to joule heating was calculated. For simulation, thickness 50nm, width 5μm, length 200μm,

electric resistivity $3.31\times10^{-8}\Omega m$, K = 222W/m·K, C_v = $3.45*10^6 J/m^3 \cdot K$, and γ=0.0015Ω/K were used for a Cu bridge.

Figure 3-17 illustrates temperature increase of the bridge over space and time when a DC current 1mA is applied. As shown in Figure 3-17(b), temperature increases as time goes and is saturated at the characteristic diffusion time, which is defined as $\tau = L^2/\alpha$. Hence, we can assume steady-state after the characteristic diffusion time. In addition, temperature distribution along the length of the bridge shows a parabolic shape, which is consistent with Equation 3-12.

As illustrated in Figure 3-17, temperature increase due to joule heating is not uniform over space. The temperature distribution has a parabola shape. In addition, temperature increases with time until the characteristic diffusion time and becomes saturated.

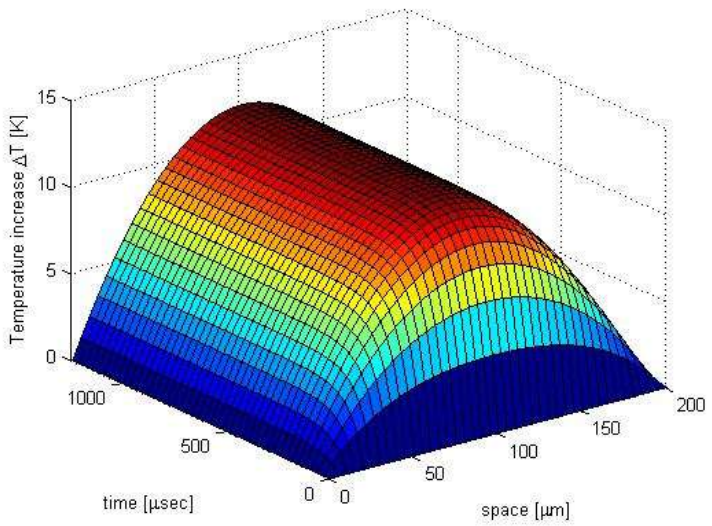

(a)

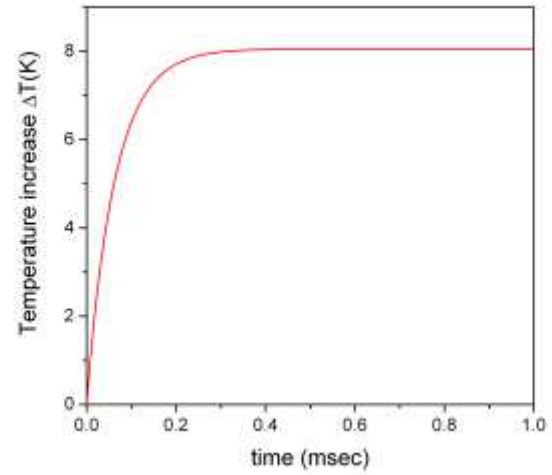

(b)

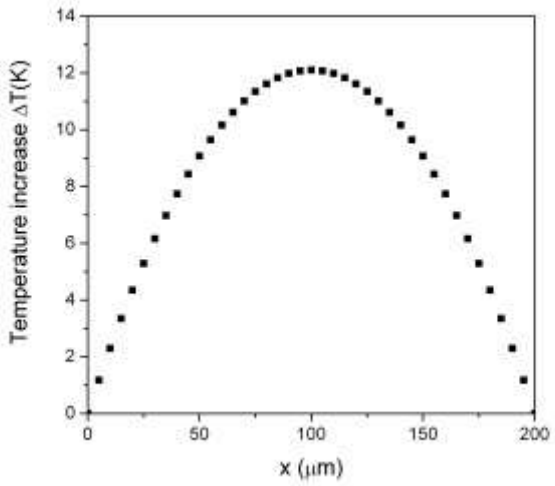

(c)

Figure 3-17 Simulation of temperature increase along a thin wire when a DC current 1mA is applied; (a) Illustration of temperature increase over space and time for the rod (b) Plot of temperature over time. The temperature is averaged over the length of a rod. Temperature increases with time and is saturated after the characteristic diffusion time τ=0.62ms. (c) Temperature distribution along the length of the rod after the characteristic diffusion time

Analysis of the relation between temperature increase verse applied current intensity is essential for further analysis of heat conduction using the steady-state joule heating and three-omega method. The average temperature over the length after steady-state is plotted in Figure 3-18. The calculated result using the analytical solution of steady-state in Equation 3-18 matched perfectly with the result using the

numerical method.

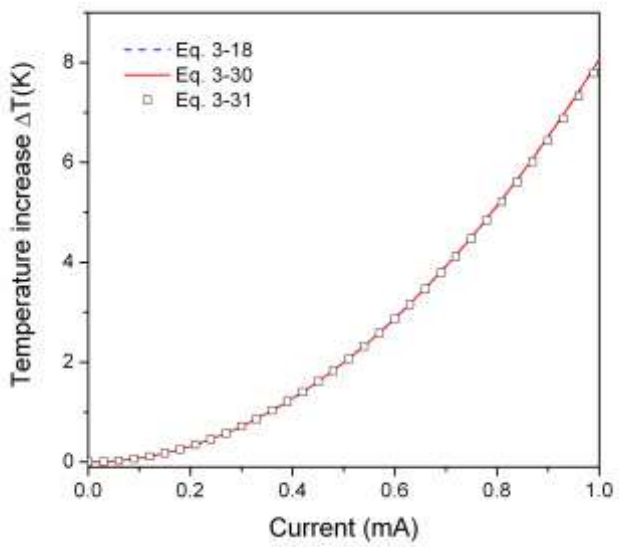

Figure 3-18 Temperature increase as a function of DC current: blue dot is the calculated result using Equation 3-18 the analytical solution in the steady-state, red solid line is the result using Equation 3-30 the numerical solution, open square is the result using Equation 3-31.

As shown in Figure 3-18, the temperature increase is linearly proportional to the square of the current intensity. Instead of Equation 3-18, the temperature increase can be approximated as follows.

$$\Delta T = \frac{1}{12}\frac{L}{A}\frac{R_0}{K}I^2 \qquad 3\text{-}33$$

Figure 3-18 compares the temperature increases which are calculated based on Equations 3-18 and 3-31. As shown in Figure 3-18, the two results are matched well unless the temperature increase is significant. At 1mA, the difference is 1.4%. The equation 3-31 shows that the temperature increase is linearly proportional to the

square of applied current. Also it is inversely proportional to the thermal conductivity.

By applying Equation 3-31, the resistance change due to joule heating can be expressed as:

$$\Delta R = \frac{dR}{dT}\frac{1}{12}\frac{L}{A}\frac{R_0}{K} I^2 \qquad 3\text{-}34$$

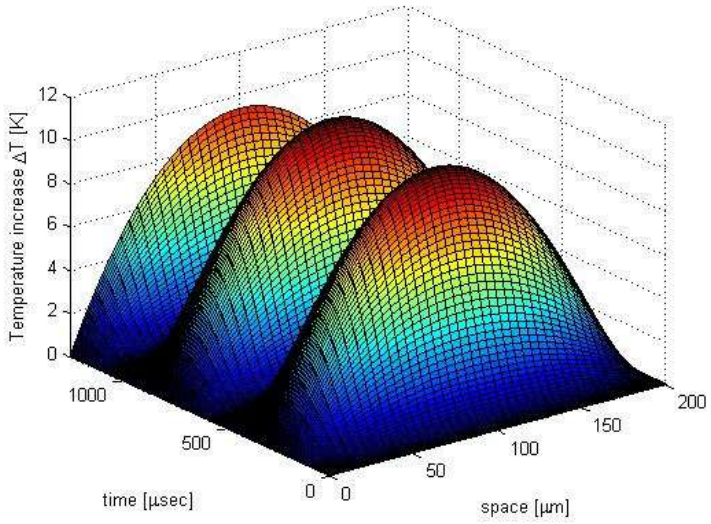

(a)

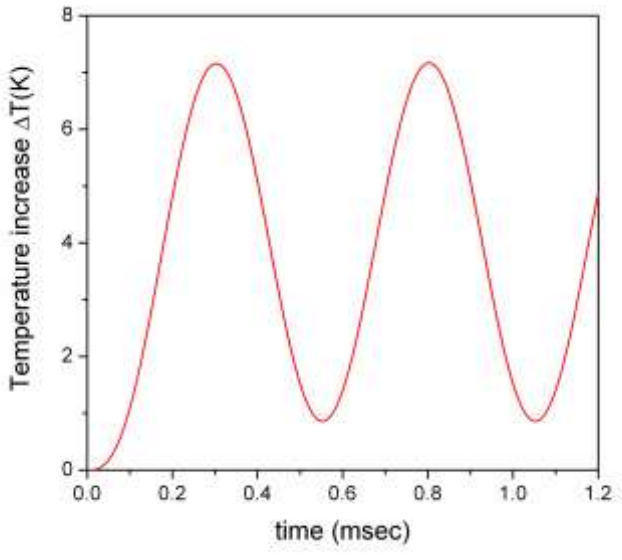

(b)

Figure 3-19 Simulation of temperature increase along the rod when an AC current is applied with 1mA amplitude and 1kHz frequency; (a) Illustration of temperature increase over space and time (b) Plot of temperature over time. The temperature oscillates with 2ω frequency.

In the case of AC current flows to the bridge, temperature distribution was calculated using the numerical method as shown in Figure 3-19. The parabola shape of the temperature distribution along the length of the bridge is the same with the DC joule heating. However, the temperature is oscillating with 2ω period in time coordinate.

3.6 Setup for three-omega measurement

Using the steady state joule heating method, we cannot measure the magnetic field-dependent thermal conductivity of Co/Cu multilayer. The detail reasons are addressed in chapter 4.3. Instead using the 3ω method, we measured spin-dependent electrical and thermal conductivities of the Co/Cu multilayer at different magnetic field intensities.

The concept of the 3ω method is illustrated in Figure 3-20 . When an AC current with 1ω frequency flows to a sample, heat is produced due to joule heating and supplied to the sample. Then, the temperature of the sample is increased and change with 2ω frequency. Then the resistance of the sample is also changed with 2ω frequency since the resistance is linearly proportional to the temperature change. The output voltage of the sample has 1ω and 3ω components since the voltage is the product of the 1ω current and the 2ω resistance.

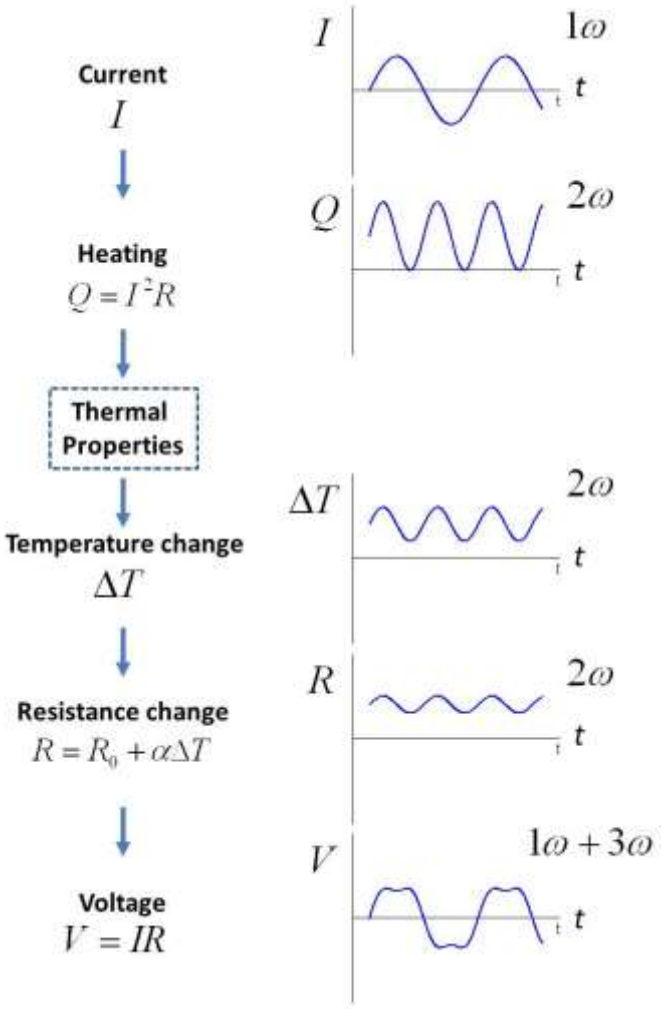

Figure 3-20 Concept of the three-omega method

The measurement was performed by placing a sample inside the gap of an electromagnet, which provided a uniform magnetic field. Then the 1ω AC current was applied to the sample and 3ω voltage signal was detected while external magnetic field is applying.

Figure 3-21 shows a schematic of the three-omega measurement setup. We use two lock-in amplifiers for generating and detecting signals. A sample is connected in series with a fixed resistor, which we know the exact resistance value. The Lock-in amplifiers are in this setup SR830 DSP Lock-in amplifiers made by Stanford research

system. Lock-in amplifier A is used for generating an input signal, reference signal, and measuring the third harmonic voltage. From the lock-in amplifier A, AC sine wave voltage (1ω component) signal is generated. The voltage signal is then converted to AC current signal using a resistor which has a high resistance value. For this study, 5kΩ resistor is used. The AC current flows through the sample bridge and a fixed resistor. The applied current value is monitored using the fixed resistor.

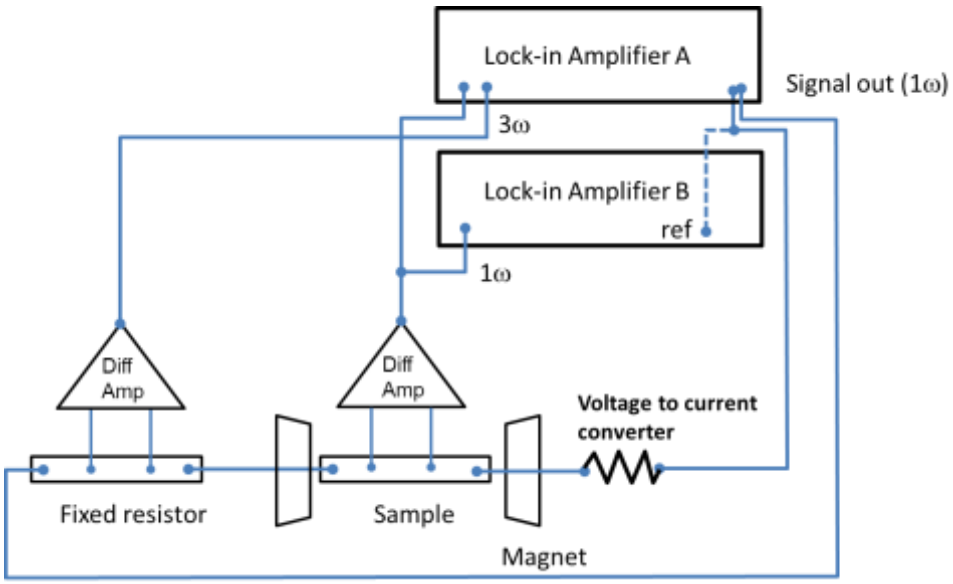

Figure 3-21 Schematic of 3ω measurement system: 1ω voltage signal was generated from lock-in amplifier A and converted to a 1ω current through a resistor, then passed through a sample resistor and a fixed resistor. The 1ω and 3ω voltage signal were generated from the sample. The 1ω signal is cancelled out using 1ω signal from the fixed resistor and only 3ω signal is detected using Lock-in amplifier A. 1ω voltage signal was detected using Lock-in amplifier B.

The voltage signal from the sample contained both 1ω and 3ω components, but the voltage signal from the fixed resistor has only 1ω component since the fixed resistor is nearly temperature independent to prevent generating a 3ω voltage

component. For the fixed resistor, a Bulk metal Z-Foil high precision resistor with temperature coefficient of resistance less than 0.2ppm/°C was used [38]. Since the 3ω voltage signal is deeply buried in the 1ω voltage signal, the voltage from the fixed resistor was subtracted from the voltage from the sample to remove the majority of the 1ω component. Then, the lock-in amplifier A was used to detect the 3ω component from the sample. In addition, the 1ω component from the sample also was measured using lock-in amplifier B.

4 Spin-dependent thermal conductivity in a Co/Cu/Co multilayer

4.1 Introduction

This study describes the thermal conductivity change in a Co/Cu/Co magnetic multilayer depending on the magnetic configuration of the ferromagnetic layers, i.e. spin-dependent heat transfer. It is worthwhile to point out recently reported the field-dependent thermal conductivity measurement, which was performed for a 144nm thick CoFe(12 Å)/Cu(21Å) multilayer using a steady-state Joule heating method with a suspended microbridge structure [39]. However, their measured thermal conductivity at room temperature showed both negative and positive change over a magnetic field. In addition, the position of the peaks for the thermal conductivity change did not match with that of electric resistance change. These trends could not be explained by the authors and are odd. In this study we got the similar trend of data using the steady-state Joule heating method, but later discovered that artifact included into the data in the measuring process. The steady-state Joule heating method and its results including the artifact is discussed in Chapter 4.3. After all, this suggests the necessity of an accurate measurement method for thermal conductivity.

In order to improve the sensitivity and accuracy of thermal conductivity measurement, the 3ω method [40] with a thermally isolated microscale bridge structure was employed. Since the 3ω method is a transient measurement technique,

the sensitivity and accuracy of the measurement in the current study is expected to be superior to the other methods, such as the static heat/sink four probe method [8], the steady-state Joule heating method [34], and even the recently developed micromachined thermal platform [41].

This chapter consists of five sections. In order to observe spin-dependent conduction, we developed a spin-valve structure, which shows 10% MR ratio. Section 4.2 explains the experimental procedure in detail to achieve the high MR ratio. Using this spin-valve structured film, we fabricated the thermally isolated microscale bridge structure. This thermally isolated bridge is required for both the 3ω and the steady-state Joule heating method. In Section 4.3, we addressed the experimental results by using the steady-state joule heating method and its practical and fundamental problems. In Section 4.4, we presented the experimental data of spin-dependent thermal conductivity change by using the 3ω method.

4.2 Development of a spin-value structure

In order to investigate spin-dependent heat transport, we need a spin-valve structured film with a high MR ratio. In order to develop the spin-valve structure, Co/Cu/Co and Co/Cu/NiFe multilayered structures were investigated. Figure 4-1 shows the MR ratio as a function of the thickness of Cu layer in the $[Co(15Å)/Cu(x)/Co(30Å)]_5$ structure. As expected, the MR ratio of Cu layer thickness 21Å is higher than that at 34Å and 40Å. Even though the data are not shown in Figure 4-1, the MR ratio of Cu layer thickness 18-24Å was lower than that of 21 Å.

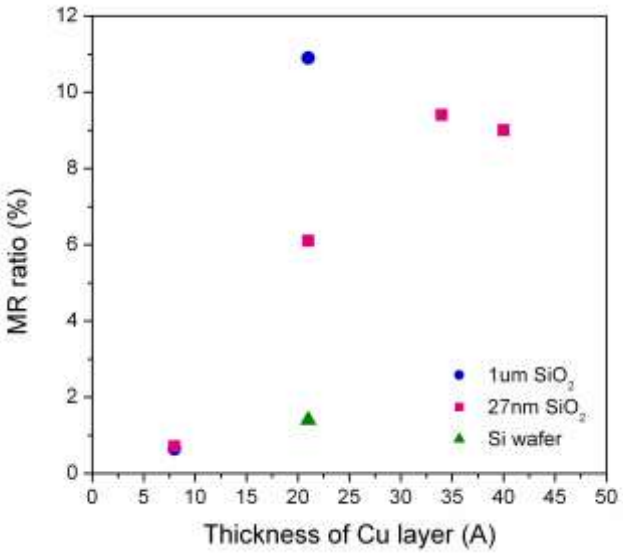

(a)

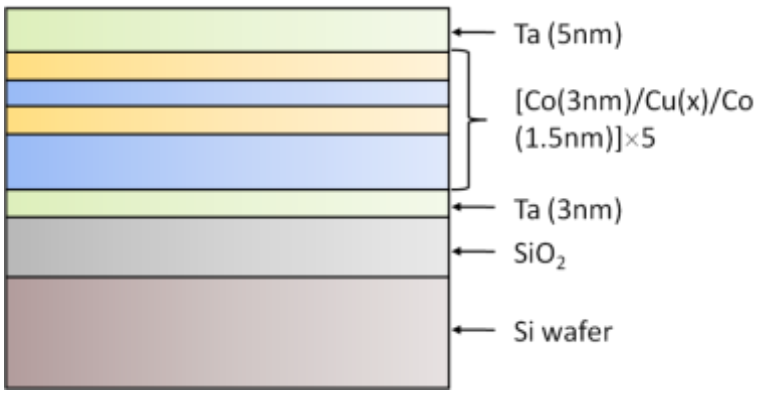

(b)

Figure 4-1 (a) MR ratio as a function of thickness of Cu layer in the $[Co(1.5nm)/Cu(x)/Co(3nm)]_5$ multilayer as shown in (b)

For Cu layer thickness 21 Å, three different substrates were compared: 1μm thick oxide, 27nm thick oxide, and bare Si substrate. Figure 4-2 plots MR behavior as a function of magnetic field for the three cases. In the case of using a 1μm thick oxide, 10.5% MR ratio was achieved. It is worthwhile to point out that the 10.5% MR ratio using typical sputtering process is incredible achievement. Meanwhile, the MR ratio is only 1.4% in the case of using a bare Si substrate. This indicates that there might be

serious current-leakage effect through the substrate. When the 27nm thick oxide was used as a substrate, 6.1% MR ratio was achieved. This indicates that the 27nm thick oxide cannot completely prevent current-leakage through the Si substrate. Interestingly, the leakage effect is not noticeable when the Cu thickness was increased to above 34Å. This can be explained that the resistance of the bridge would be smaller than that of the substrate when the Cu layer is thicker than 34Å. In this case, an applied current mainly flows through the bridge instead of the substrate.

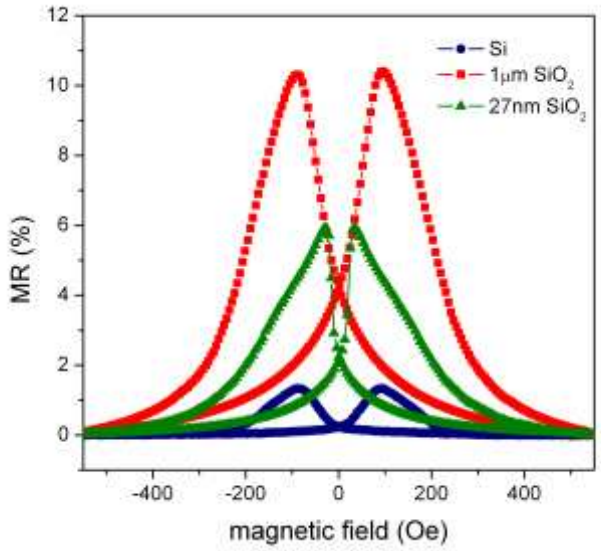

Figure 4-2 MR curve for $[Co(1.5nm)/Cu(2.1nm)/Co(3nm)]_5$ multilayer with 3 different substrates: bare Si, 1μm thick SiO_2, 27nm thick SiO_2

In the case of Cu layer thickness is 8Å, the MR ratio was much lower than that of the other thickness as shown in Figure 4-3. This unusually low MR ratio might be due to the discontinuity of 8Å thick Cu film. The 8 Å thick of Cu film might be not thick enough to form a continuous film since the exposed time to plasma is only 5

seconds.

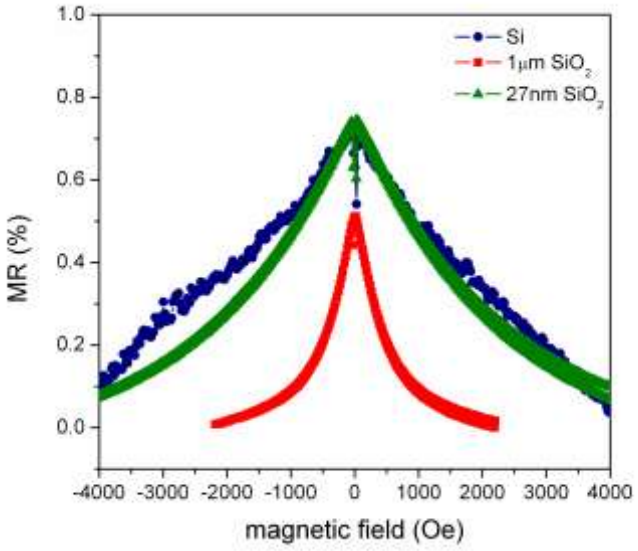

Figure 4-3 MR curve for $[Co(1.5nm)/Cu(0.8nm)/Co(3nm)]_5$ multilayer with 3 different substrates: bare Si, 1μm thick SiO_2, 27nm thick SiO_2

One of the easiest ways to improve the MR ratio is to increase the repeated number of the layers. Figure 4-4 shows the MR ratio as a function of the repeat number of stack for two cases: Si\Ta(3nm)\[Co(4nm)\Cu(4nm)\Co(.7nm)\NiFe(2nm) \Co(0.7nm)]$_N$\Ta(3nm) and Si\SiO_2(27nm)\Ta(3nm)\[Co(3nm)\Cu(3.4nm) \Co(1.5nm)]$_N$\Ta(5nm). From the Figure 4-4, the optimum repeated number for current study was 5. Meanwhile typical repeated numbers in literature is 20-30. The low repeated number could be stem from high interface roughness at the Co/Cu interface.

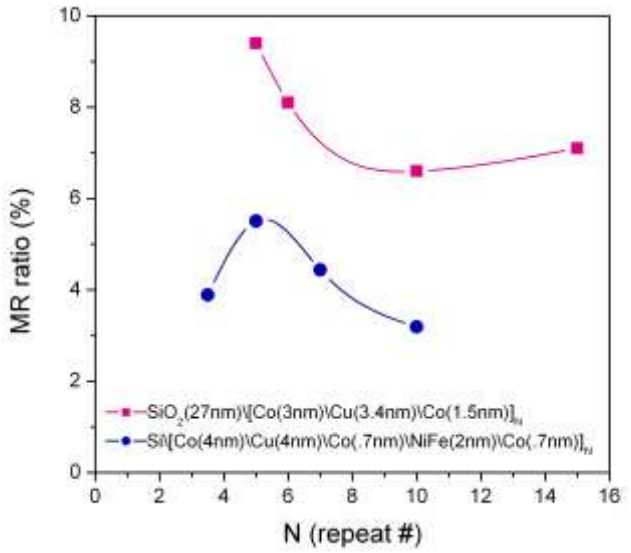

Figure 4-4 MR ratio(%) as a function of repeat number N of the stack for Si\Ta(3nm)\[Co(4nm)\Cu(4nm)\Co(.7)nm\NiFe(2nm)\Co(.7nm)]$_N$\Ta(3nm) and Si\SiO_2(27nm)\Ta(3nm)\[Co(3nm)/Cu(3.4nm)/Co(1.5nm)]$_N$\Ta(5nm)

After all, the layer structure for this study was selected to Ta (30Å)/[Co(30Å)/Cu(34Å)/Co(15Å)]$_5$/Cu(34Å)/Ta (50Å). The films were deposited on the top of a 27nm thermally grown silicon dioxide/silicon wafer using DC magnetron sputtering at room temperature. The 27nm dry thermal oxide wafer was provided from University wafer [42]. Four probe configuration and Au pads were patterned on the top surface of these layers. Then, the bridge part was released by removing Si beneath the bridge regions using XeF_2. Figure 4-5 shows a top view of the optical microscope image of the four probe configuration and its bridge and a side view of the scanning electron microscope image of the bridge. The bridge was designed with a width of 5μm and a length of 200μm. Then, the Au pads of the four probe configuration were wire bonded to a chip carrier for electric and thermal measurement.

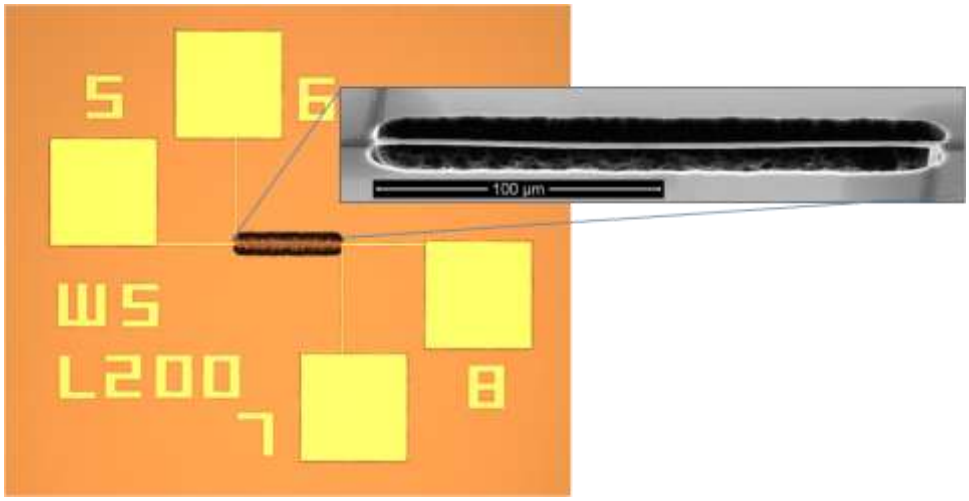

Figure 4-5 A top view of the optical microscopy image of the four probe configuration and a side view of the scanning electron microscope image of the suspended bridge

4.3 Results for the steady state joule heating measurement

We applied DC current to the bridge structure and measured the voltage across the bridge. Current was applied from 0.1mA to 1.0mA with 0.05mA step. Figure 4-6 shows the current-voltage (I-V) characteristic of the bridge. The data shows linear curve, which obey Ohm's law. From the I-V curve, the resistance of the bridge was calculated using Ohm's law.

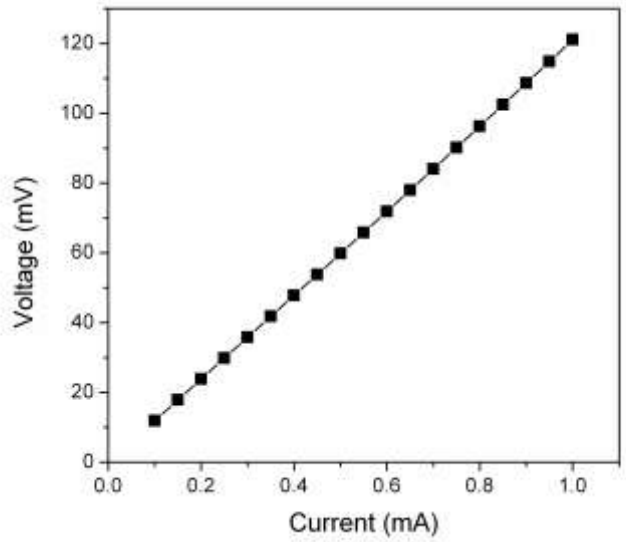

Figure 4-6 Current-Voltage (I-V) characteristic curve for the bridge; the solid line is a guide for eye.

Figure 4-7 plots the resistance as a function of current square. It shows linear curve as expected in Equation 3-21. The Data was fitted using the least square method. From the fitted line, the intercept represents R_0.

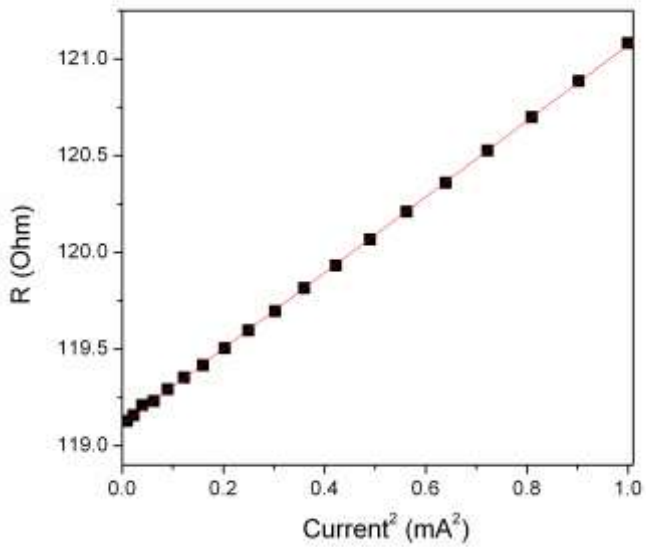

Figure 4-7 Plot of the resistance as a function of current square; the solid line is a fitted line using the least square method.

Figure 4-8 plots R_0 as a function of magnetic field, which shows spin-dependent electric resistance change, i.e. GMR behavior. The MR ratio is 8.0%. At the maximum magnetic field intensity, the electrical resistance has the lowest value. At this point, the two Co layers are aligned with the same direction of the external magnetic field. As the magnetic field intensity decreases, the electric resistance increases continually and has a peak value just after switching the direction of the magnetic field. The position of the largest resistance indicates that the magnetic orientation of the two Co layers is antiparallel. The magnetic field intensity of the antiparallel state is determined by the difference between the coercivity of the two Co layers. After the peak, the electrical resistance decreases continually and becomes saturated again as the magnetic field intensity increases to the maximum value. When the magnetic field intensity is applied the opposite direction, the same trend shows up. Hence two symmetrical peaks in electrical resistance exist at near zero magnetic field intensity, where the orientation of magnetization of the two ferromagnetic layers is antiparallel. Meanwhile at the maximum magnetic field intensity, the magnetic direction of two ferromagnetic layers is aligned with the same direction to the applied magnetic field direction and the resistance becomes lowest.

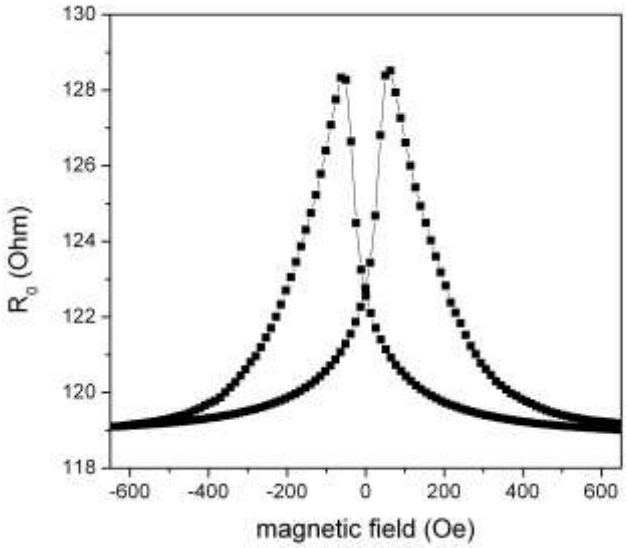

Figure 4-8 Plot of R_0 as a function of magnetic field for the rod from steady-state joule heating measurement. The MR ratio is 8.0%.

For the steady-state joule heating method, electric resistance change due to joule heating is measured. The resistance change, ΔR is plotted as a function of magnetic field in Figure 4-9. The difference of the electrical resistance was obtained by subtracting R_0 from the resistance value at 1mA. We should be very careful to interpret the curve. As the magnetic field intensity decreases from the maximum point, the electrical resistance difference slowly decreases. Right after switching the direction of the magnetic field, however, the resistance difference suddenly jumps up to the peak value then falls down. From the lowest resistance value, the resistance difference slowly increases until saturated. The magnetic field value representing the antiparallel state from Figure 4-8 is located in the middle between the two magnetic values representing the highest and the lowest resistance value of the curve. This cannot be explained with spin configuration and very odd. To verify the trend, we

measured several times with different samples and got the same trend.

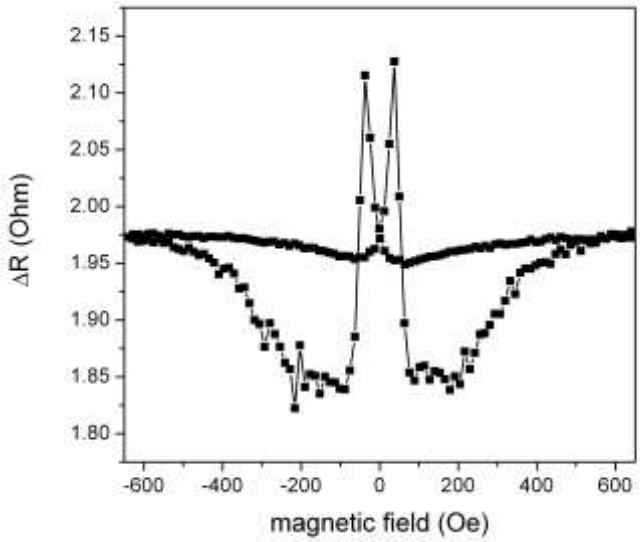

Figure 4-9 Plot of the electrical resistance difference due to joule heating as a function of magnetic field; I-V curve was measured as current increases.

However, this trend is not true. Some artifact was included during the measurement. For the measurement, external magnetic field was applied to the sample from 650 Oe to -650 Oe with 13Oe step. At each step, we measured the I-V curve. We assumed that the magnetic field intensity was kept the same during the I-V measurement. However, this assumption is not true. We noticed that magnetic field continuously increased a little bit at given set value. Therefore, the MR curve was shifted during measurement. In order to verify this argument, we shifted one step of the MR curve in Figure 4-8 and subtracted the original curve from the shifted curve, which is illustrated in Figure 4-10. This calculated result has the exactly same trend with the experimental data shown in Figure 4-9.

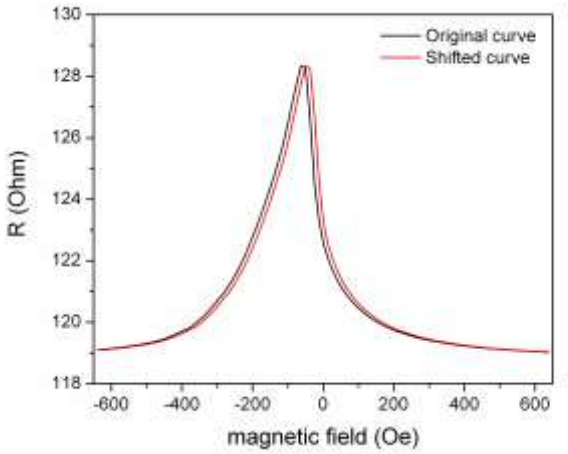

(a)

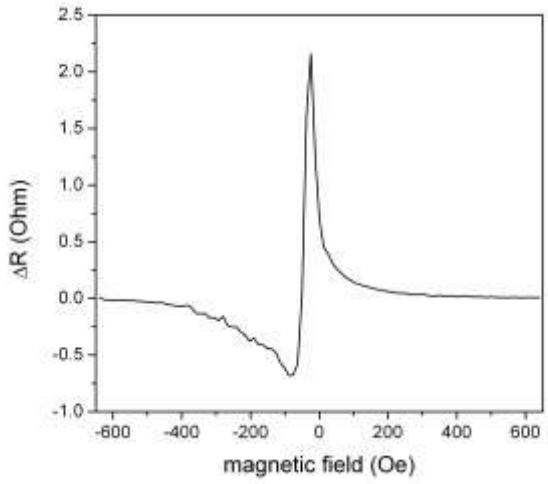

(b)

Figure 4-10 Illustration of (a) MR curve shifting during the I-V measurement and (b) its resistance difference

To further confirm the argument, we measured the I-V curve from 1.0mA to 0.1mA with 0.05mA step as shown in Figure 4-11. The measured resistance difference while current increases has the exactly opposite trend with the result while current decreases.

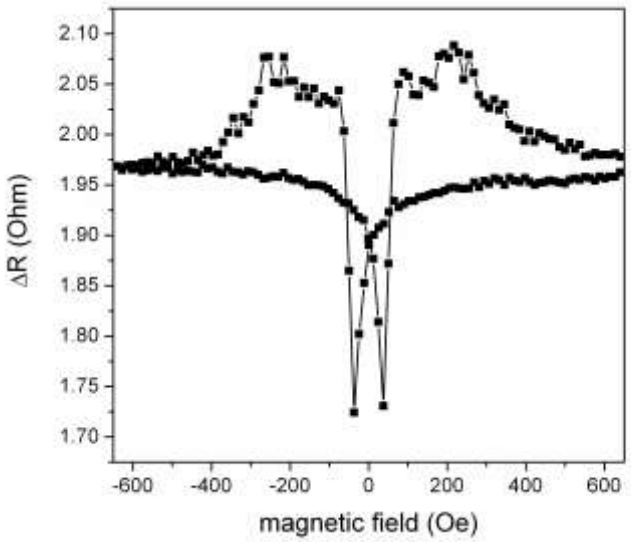

Figure 4-11 Plot of the electrical resistance difference due to joule heating as a function of magnetic field; I-V curve was measured as current decreases.

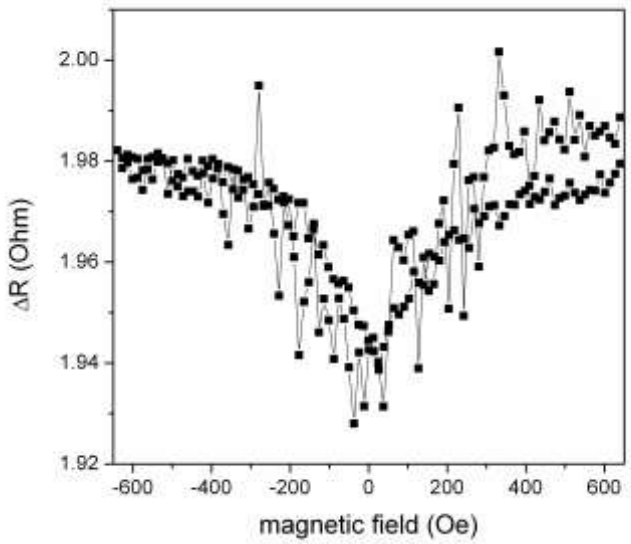

Figure 4-12 Plot of the difference of the electrical resistance of the rod due to joule heating as a function of magnetic field after compensating the artifact during the I-V measurement

In order to compensate this artifact, we averaged the above two data as shown in Figure 4-12. There is no abrupt change in the curve. As the magnetic field intensity

decreases from the maximum point, the resistance difference slowly decreases. At certain magnetic field intensity after the magnetic field switches the direction, the curve has the minimum value. Then, the resistance difference increases until saturated. But it is not clear whether the data matches with the spin configuration.

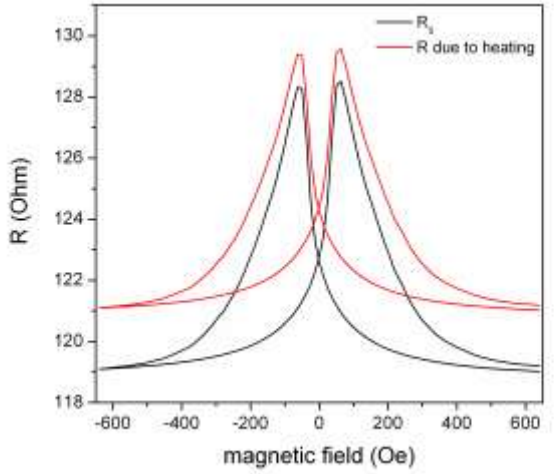

(a)

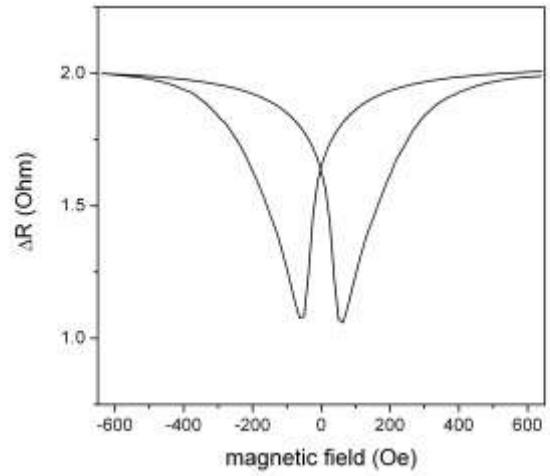

(b)

Figure 4-13 Illustration of (a) MR curve change due to heating effect and (b) the resulted in resistance difference; the red line in (a) is the resistance change due to heating effect.

It is necessary to know the dependency of ΔR upon spin configuration. It is

well known that the MR ratio decreases with temperature [8, 39, 43-45]. It caused by intermixing up- and down-spin in the ferromagnetic layers [46]. Figure 4-13 illustrates the resistance difference change due to a heating effect, which is calculated based on the observation that the resistance is increased to 2 Ω at 1mA and the MR ratio is decreased 10% from the original value.

From Figure 4-13(b), we got the proper trend of ΔR vs. H. The trend shows two valleys, corresponding to the antiparallel state of the ferromagnetic layers. However, we should be very careful to interpret the negative change in Figure 4-13(b).

Equation 3-21 can be normalized by dividing the equation at the parallel state.

$$\frac{\Delta R}{\Delta R_p} = \frac{R_0 / R_{0,p}}{K / K_p} \qquad 4\text{-}1$$

where p represents the parallel state of the ferromagnetic layers.

Equation 4-1 can be simplified as follows.

$$1 + \delta(\frac{\Delta R}{\Delta R_p}) = \frac{1 + \delta R_0 / R_{0,p}}{1 + \delta K / K_p} \qquad 4\text{-}2$$

$$\delta(\frac{\Delta R}{\Delta R_p}) = \frac{\delta R_0}{R_{0,p}} - \frac{\delta K}{K_p} \qquad 4\text{-}3$$

Here δ represents the change over magnetic field, while Δ represents the change due to joule heating. If the heat transport is affected by spin-dependent scattering mechanism, the relation of $\delta K/K_p \sim -\delta R/R_p$ would be held. Then, the $\delta(\Delta R/\Delta R_p)$ should be a positive change instead of a negative change since the $\delta R/R_p$ shows a positive change as shown in Figure 4-8. However, Figure 4-13(b) shows the negative change for $\delta(\Delta R/\Delta R_p)$. If the trend in Figure 4-13(b) is correct, Equation 4-3 is

wrong. When we derived Equation 4-1, we assumed that dR/dT is constant for the spin configuration. However, the dR/dT is not constant for the spin configuration. As mentioned previously, the MR ratio decreases as temperature increase. It indicates that dR/dT is dependent on spin configuration. Therefore, Equation 4-3 should be modified as follows.

$$\delta\left(\frac{\Delta R}{\Delta R_p}\right) = \frac{\delta(dR/dT)}{(dR/dT)_p} + \frac{\delta R_0}{R_{0,p}} - \frac{\delta K}{K_p} \qquad 4\text{-}4$$

From the steady-state joule heating measurement, we can get $\delta(\Delta R/\Delta R_p)$ and $\delta R/R_p$. But we cannot get $\delta K/K_p$ since the value of $\delta(dR/dT)/(dR/dT)_p$ is unknown.

In the case of Yizhang et al.[39] , they might assume that only R and K terms are dependent on a magnetic field and treat $\delta(dR/dT)/(dR/dT)_p$ as constant for a magnetic field. Then, they might calculate K. In this case, $\delta K/K_p$ is $\delta R/R_p$ - $\delta(dR/dT)/(dR/dT)_p$. Since $\delta R/R_p$ is relatively small compared to $\delta(dR/dT)/(dR/dT)_p$, the $\delta K/K_p$ would be similar to Figure 4-9. Obviously it is not correct data.

4.4 Results for the three-omega measurement

For the thermal conductivity measurement, the three-omega (3ω) method was employed. As described earlier, the sample was fabricated as a microscale bridge structure as shown in Figure 4-5. This thermally isolated structure allows one-dimensional heat transport along the length of the bridge. Since the bridge between the two voltage probes is suspended to allow temperature fluctuation and all the probes are thermally conductive to the heat sink, which is silicon substrate, the 3ω

data were analyzed with the relationship between 3ω voltage and thermal conductivity derived by Lu *et al*.[47] and Chris et al.[48].

3ω voltage signal V_{3w} is composed of in-phase component, X_{3w} and out-of phase component, Y_{3w}.

$$V_{3\omega} = \sqrt{X_{3\omega}^2 + Y_{3\omega}^2} \qquad 4\text{-}5$$

In particular, X_{3w} can be expressed as.

$$X_{3\omega} = -C_1 \frac{L}{A}\frac{dR}{dT}\frac{I^3 R}{K\sqrt{1+(2\omega\tau/10)^2}} \qquad 4\text{-}6$$

where C_1 is constant, L is the length and A is the cross-sectional area of the bridge structure; dR/dT is the ratio of an electrical resistance to temperature, K is the thermal conductivity, and R is the electrical resistance across the bridge structure; I is the amplitude, ω is the angular frequency of the applied AC current.

τ is the thermal diffusion time defined as.

$$\tau = L^2/\alpha = L^2 C_v / K \qquad 4\text{-}7$$

First of all, we do find that $|X_{3\omega}| \propto I^3$ and $|X_{3\omega}| \propto 1/\sqrt{1+(2\omega\tau/10)^2}$ as shown in Figure 4-14. This confirmed that our 3ω voltage data is reliable.

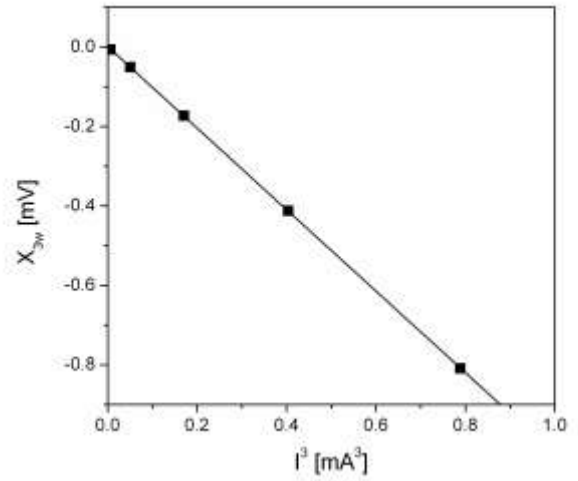

(a)

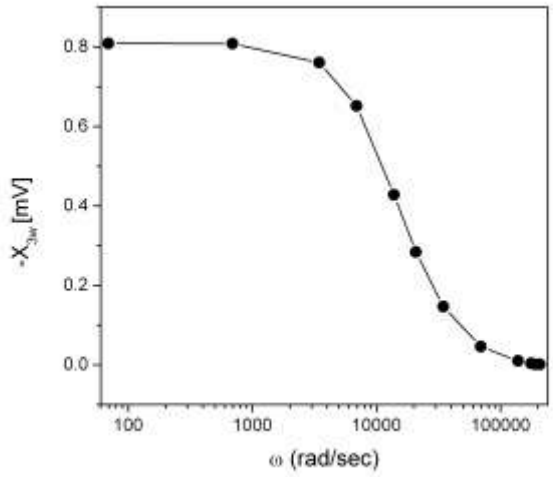

(b)

Figure 4-14 In-phase 3ω voltage (a) as a function of current intensity at f=11Hz, showing the relation $X_{3\omega} \sim -I^3$. The solid line is the least-square fitted curve, (b) as a function of angular frequency, showing $1/\sqrt{(1+(2\omega\gamma/10)^2}$ relation; the solid lines are to guide the eyes.

At low frequency ($\omega\tau << 1$), Equation 4-6 is reduced as follows.

$$X_{3\omega} = -C_1 \frac{L}{A}\frac{dR}{dT}\frac{I^3 R}{K} \qquad (\omega\tau << 1) \qquad 4\text{-}8$$

In order to see the relative change over the magnetic field, Equation 4-8 is normalized by dividing the equation at parallel state. Then the equation becomes:

$$\frac{X_{3w}}{X_{3w,p}} = \frac{dR/dT}{(dR/dT)_p}\frac{R/R_p}{K/K_p} \qquad (\omega\tau << 1) \qquad 4\text{-}9$$

where p represents the parallel state of the magnetization.

Using the 3ω measurement setup, we measured R and $X_{3\omega}$ simultaneously while sweeping the magnetic field from 650 Oe to -650 Oe. Figure 4-15 shows the measured electrical resistance change of the bridge over the magnetic field. The $\delta R/R_p$ is spin-dependent.

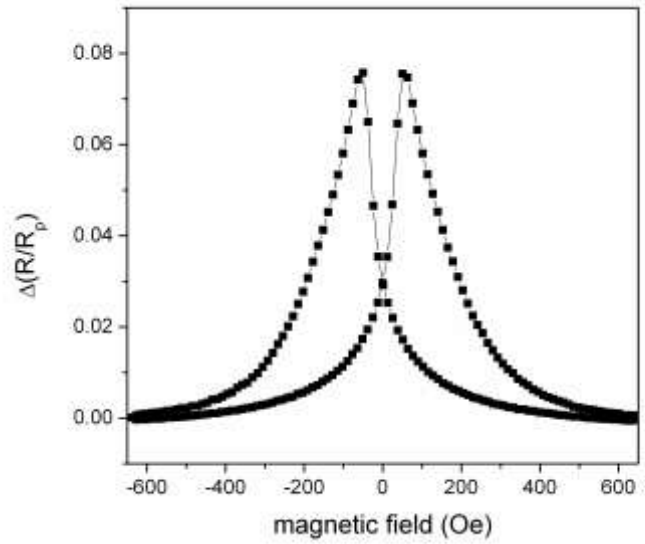

Figure 4-15 MR curve for a [Co (3 nm)/Cu (3.4 nm)/Co (1.5nm)] multilayer using AC current with frequency 11Hz and amplitude 1mA; the solid lines are to guide the eyes.

Figure 4-16 shows the in-phase 3ω voltage change over the magnetic field. From Equation 4-4 and 4-9, the result shown in Figure 4-16 should be the same as the result in Figure 4-12. Indeed, the two data are similar, but the data in Figure 4-16 is more precise.

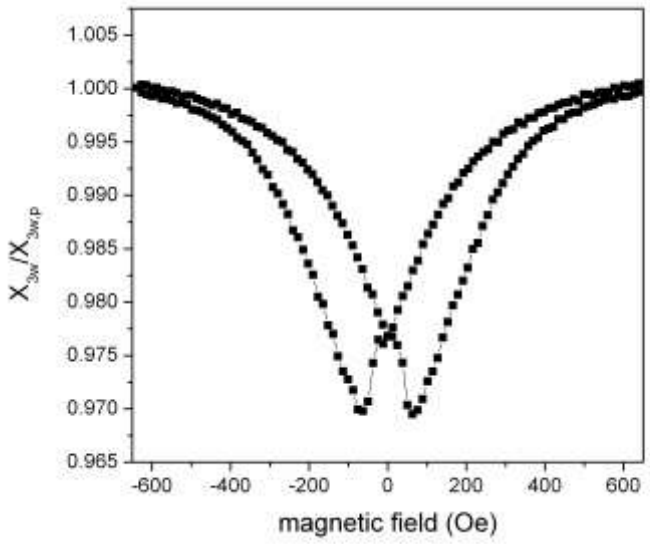

Figure 4-16 Relative variation of the in-phase 3ω voltage component as a function of the magnetic field for a [Co (3 nm)/Cu (3.4 nm)/Co (1.5nm)] multilayer using AC current with frequency 11Hz and amplitude 1mA; the solid lines are to guide the eyes.

As described in previous section 4-3, dR/dT is also spin-dependent. Hence, K/K_p cannot be obtained from the data in Figure 4-15 and Figure 4-16. In Equation 4-9, there are two unknown variables. It is worthwhile to remind that the steady state joule heating method has the same problem.

This problem can be solved frequency dependency in Equation 4-8. At high frequency, K term diminishes and substitutes to heat capacity C_v as follows.

$$X_{3\omega} = -C_1 \frac{L}{A}\frac{dR}{dT}\frac{I^3 R}{\omega L^2 C_v / 5} \qquad (\omega\tau >> 1) \qquad 4\text{-}10$$

Since the C_v is not dependent on magnetic field or spin direction, Equation 4-10 can be normalized as follows.

$$\frac{X}{X_p} = \frac{dR/dT}{(dR/dT)_p}\frac{R}{R_p} \qquad (\omega\tau >> 1) \qquad 4\text{-}11$$

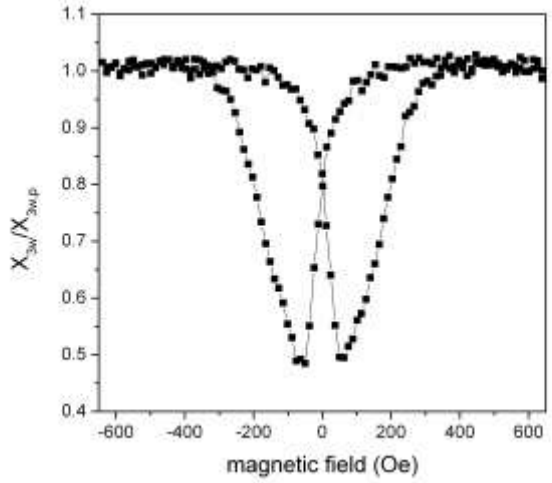

(a)

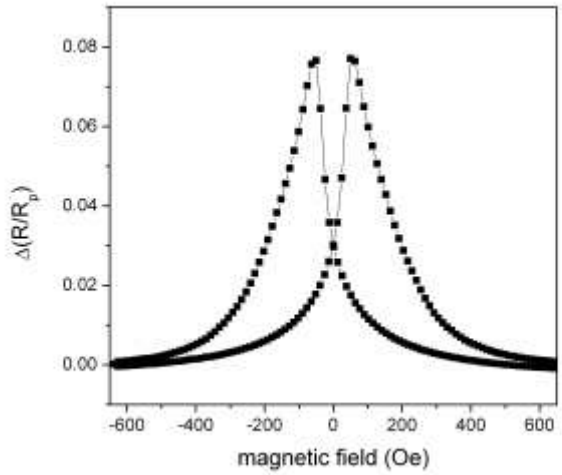

(b)

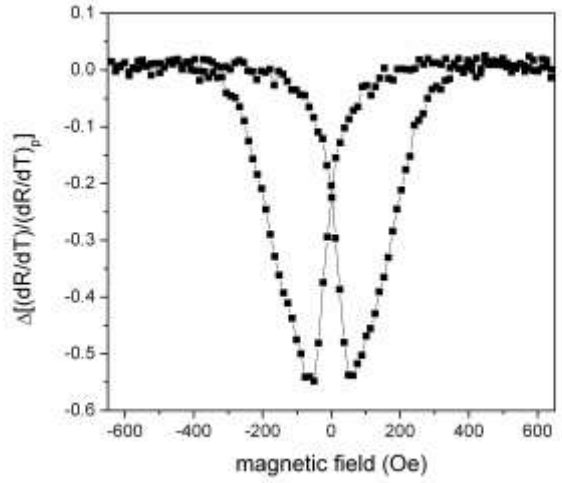

(c)

Figure 4-17 Relative variation of (a)$X_{3\omega}$, (b)R, and (c) dR/dT at 28 kHz, as a function of the magnetic field for a [Co (3 nm)/Cu (3.4 nm)/Co (1.5nm)] multilayer. The solid lines are to guide the eyes.

We measured X/X_p, R/R_p at 28kHz ($\omega\tau >> 1$). Then, $(dR/dT)/(dR/dT)_p$ was extracted using Equation 4-9 as shown in Figure 4-17 by assuming $(dR/dT)/(dR/dT)_p$ does not depend on frequency. It is worthwhile to point out that the spin-dependent change of $(dR/dT)/(dR/dT)_p$ is very similar to the data in Figure 4-13(b).

Since we already measured X/X_p, R/R_p at 11Hz ($\omega\tau << 1$), we can get K/K_p using Equation 4-9 with the data of $(dR/dT)/(dR/dT)_p$. Figure 4-18 shows the spin-dependent thermal conductivity change. The behavior of the thermal conductivity over the magnetic field intensity was similar to that of the electric conductivity. The thermal conductivity is saturated at the maximum magnetic field which the field intensity is large enough to align the magnetization of the two Co layers parallel each other. As the field intensity reduces, the thermal conductivity decreases and has a valley just after switching the direction of magnetic field intensity. Two symmetrical valleys are observed in the thermal conductivity dependence with the magnetic field, where the orientations of the magnetization of the two Co layers are antiparallel. The position of the two valleys matches to that of the peaks for the electric resistivity. The maximum ratio of the electrical resistivity and the thermal conductivity is 7.5%, 50.0% respectively.

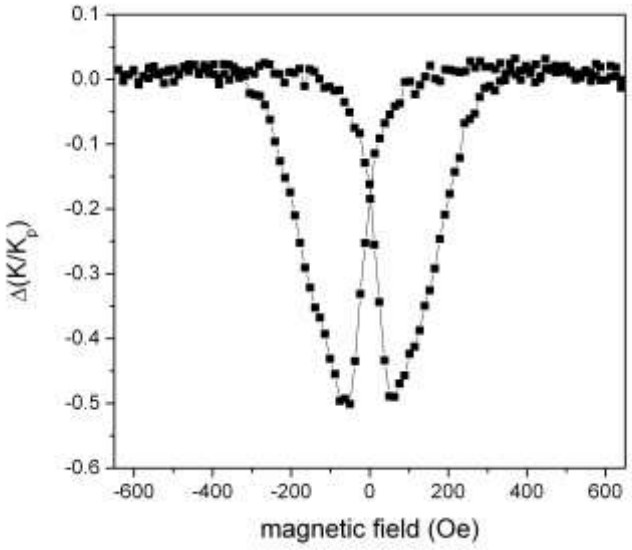

Figure 4-18 Relative variation of the thermal conductivity in CIP geometry at room temperature, as a function of the magnetic field for a [Co (3 nm)/Cu (3.4 nm)/Co (1.5nm)] multilayer; the solid lines are to guide the eyes.

4.5 Discussions

In pure metals, the electronic contribution to the thermal conductivity is dominant compared to the phonon contribution at all temperature including room temperature [2]. In a pure metal, the Pauli principal reduces the possible scatterings of electrons, while there is no empty state to scatter into for phonons [49]. Therefore, Weidemann-Franz law can be applied to metals at room temperature.

The difference between the ratio of the electric resistivity and the thermal conductivity indicates that the Lorenz number of Weidemann-Franz law is different between the parallel state and antiparallel state, which is consistent with the literature [9, 39]. For the current study, the Lorenz number of the antiparallel state is lower than that of the parallel state. The difference can be qualitatively explained by the

difference of the scattering rate for heat and charge transport by electrons.

The spin-dependent electron scattering in a CIP geometry for the current study can be explained by the interface scattering at Co/Cu interface due to the different band structure of the Co layers, which have the spin-dependent electronic band structure [7, 14]. When the spin direction of electron is different from the magnetic direction of the Co layer, the scattering rate of heat transport can be much larger than that of the charge transport due to inelastic electron-phonon and electron-magnon scattering [9, 39]. In the parallel state, electrons which have the same spin direction with the Co layer dominantly contribute heat and charge transport. Therefore the effect of severe scattering of heat transport is negligible. However, in the antiparallel state, the electrons in both spin directions are reflected from the anti-aligned Co layers and hence heat transport experiences much strong scattering and the thermal conductivity decrease significantly.

4.6 Summary

To summary, spin-dependent heat transport phenomenon was observed successfully in a magnetic multilayered structure. We developed a spin-valve structured film, which shows 10% MR ratio with a low saturation field. Using the films, we fabricated a microscale thermally isolated bridge structure. In order to measure the thermal conductivity of thin films, we built the three omega setup. Then we measured the spin-dependent thermal conductivity by using the three omega method with the spin-valve structured bridge. The thermal conductivity change

showed 50% difference depending on the magnetic configuration. The Lorentz number is also spin-dependent. Mechanisms responsible for the charge and heat transport may not be identical.

5 Experimental details for thermal boundary resistance

In addition to the spin-dependent heat transport, this thesis focused on heat transport of thin films in cross-sectional direction. In nanoscale multilayered structures, thermal boundary resistance could dominate the overall heat transport rather than the thermal properties of each individual layer. A temperature difference occurs when heat flows across an interface between dissimilar materials because a thermal boundary resistance exists in the region of the interface. This study investigates the thermal boundary resistance between metals and dielectrics using an optical pump-probe technique.

5.1 Introduction

Heat management is essential for the reliability in integrated circuits and related devices. An abrupt temperature rise can cause critical failure in electronic devices even if the temperature rise occurs in a local area for a very short time. As the sizes of electronic components in devices continue to decrease, the power density of electronic components increases exponentially. Thus, efficient heat removal from the active electronic components becomes a critical requirement [50]. Since most devices have thin-film structures, there has been a growing interest in the thermophysical properties of thin-film materials, which can be very different from bulk properties [51, 52].

In the case of thin-film structures, heat transport on a short length scale and time scale is often related to the properties of interfaces [53]. In most devices, metallic films play a role in dissipating heat. Meanwhile, dielectric films are used to isolate electrical or thermal transport from electronic components. Thus, determining the thermal properties of metal and dielectric thin films is very important. In addition, thermal boundary resistance between metal and dielectric thin films could dominate the overall heat transfer process rather than the thermal properties of each individual thin film [54]. Therefore, the thermal boundary resistance between metal and dielectrics is becoming critical to both the design and selection of materials in nanoscale devices.

The thermal boundary resistance can exist in interfacial regions between dissimilar materials [55]. The thermal boundary resistance causes temperature discontinuity across the boundary when heat flux is applied. Some reasons for the thermal boundary resistance are the presence of an extremely thin disordered region between the materials, scattering of the heat carrier at the interface, and the reflection of phonons due to differences in the phonon dispersion of the materials [55].

This study examines the thermal boundary resistance between metals and dielectrics, particularly at the Au/SiN_x and CoFe/SiN_x interface using a transient thermoreflectance (TTR) technique at room temperature. Gold, Au, is one of most widely used materials for integrated circuit technology. Cobalt Iron, CoFe, has been extensively used for magnetic data storages. Silicon Nitride, SiN_x, is often used as a gate dielectric layer in thin-film transistors. It is also used as a passivation layer to

protect semiconductor devices, as an insulator, and a chemical barrier in fabricating metal-nitride-oxide-silicon (MNOS) devices [56]. Therefore, these interfaces can be a generic metal-dielectric interface to investigate even though there is no specific application for current data storage or integrated circuit technology. The TTR technique has been used to measure the thermal boundary resistance between thin metal films and dielectrics [54, 57]. In this study, a nanosecond reflectance thermometry was used for the TTR. While temperature dependent transport properties are relevant and required to provide a full understanding of the underlying physics, the present work only focuses on room temperature component. Future work is directed at the systematic study of temperature dependent transport properties of metal-dielectric interfaces.

5.2 Setup for a pump-probe measurement system

The instrumentation and analysis fundamentally depend on the duration of the heating pulse and the detecting method. In this study, we used a nanosecond pulse for heating and a continuous time-domain laser-reflectance for thermometry. The energy from each pulse in the pump beam produced a sudden temperature rise at the surface of a sample. The cooling of the surface temperature was then examined by monitoring the reflectivity change of a probe beam because the reflectivity is linearly proportional to the temperature for most metals [58].

Figure 5-1 illustrates the concept of the pump-probe method. A laser pulse with 10ns duration pumps energy to a sample surface. The reflected beam of the

continuous-wave laser has the thermal response of the sample. The thermal response has the information of the thermal properties of the sample. The information can be decoded by analyzing a thermal model.

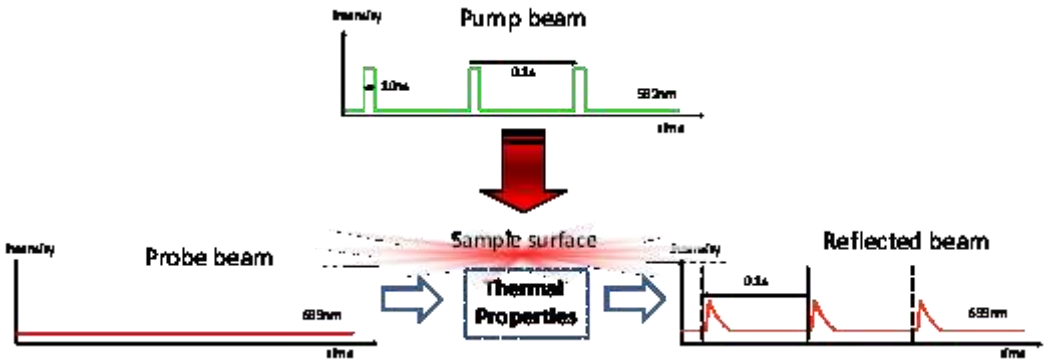

Figure 5-1 Illustration of a pump-probe technique

A schematic of the experimental setup for TTR is shown in Figure 5-2. The pump beam was guided onto the surface of a sample through an objective lens at normal incidence. Several mirrors and lenses were located in the path of the pump beam to control the position and size of the pump spot on the surface. The position and size were monitored by a CCD camera. The divergence of the pump beam and therefore the size of the focused pump spot were controlled by adjusting the distance between the lenses.

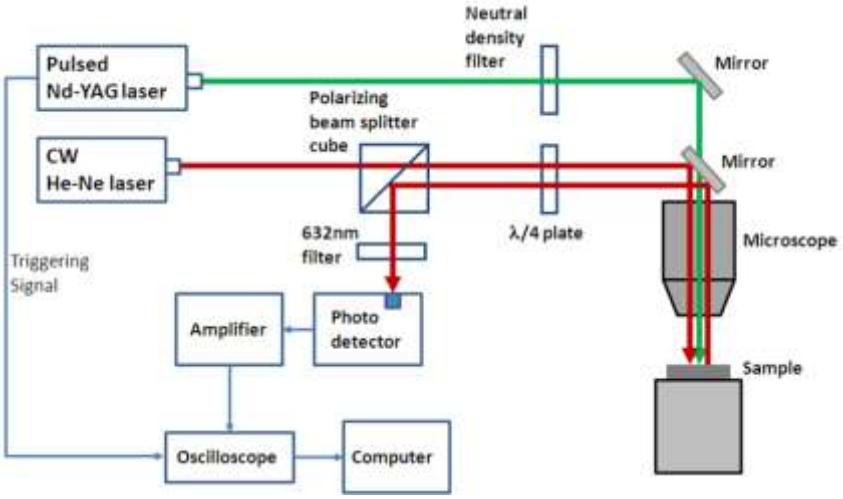

Figure 5-2 Schematic of the pump-probe measurement setup using a nanosecond pulse laser for pumping and a continuous-wave laser for probing.

The high power light pulses were produced by a frequency-doubled Nd doped YAG laser operating at a 532 nm wavelength. The Nd:YAG laser for the current study is a Quanta-Ray® Lab -130 laser made by Spectra-Physics, which is now Newport. The pulse duration was about 10 ns at full width half maximum (FWHM), and the repetition rate was 10Hz. Since the time interval between pulses was a relatively long 100ms, the residual heating of a sample was negligible.

Figure 5-3 shows the pulse shape of the Nd:YAG laser. The intensity of the laser pulse was measured 100 times using a PDA10A amplified photodetector and a DSO6102A oscilloscope, and then averaged. The pulse shape shows a Gaussian profile.

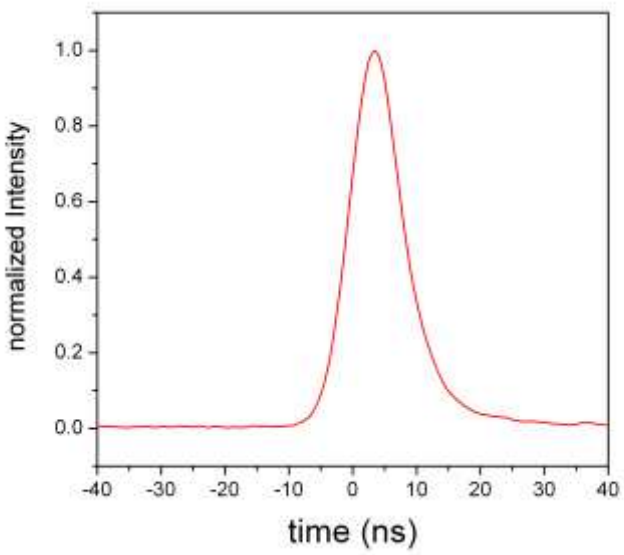

Figure 5-3 Pulse shape of the Nd:YAG laser which shows a Gaussian profile

Since the laser pulse of the Nd:YAG laser has a Gaussian shape, the intensity and FWHM of the laser pulse were measured depending on the power level, which is shown in Figure 5-4. As expected, the intensity of the laser pulse increases as the power level increases. But the intensity is not stable at the power level 1 and 2. Figure 5-4(a) shows how much intensity vary at a given power level. The ratio of the intensity variation is high at the power level 1 and 2 but becomes down to almost zero above the power level 3. This indicates that the laser power becomes stable above the power level 3. In addition, the FWHM decreases as the power level increases and become less than 12ns above the power level 3. According to the specification of the Nd:YAG laser, the FWHM will be 8 ~ 12ns. Based on the above observation, we can conclude that the laser pulse is stable and reliable above the power level 3, which range has been used in the current study.

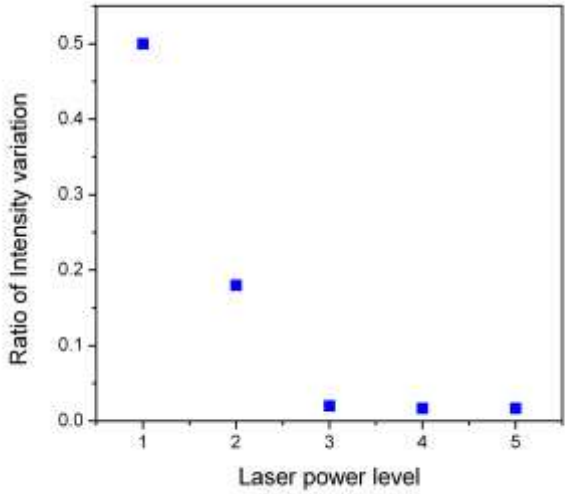

(a)

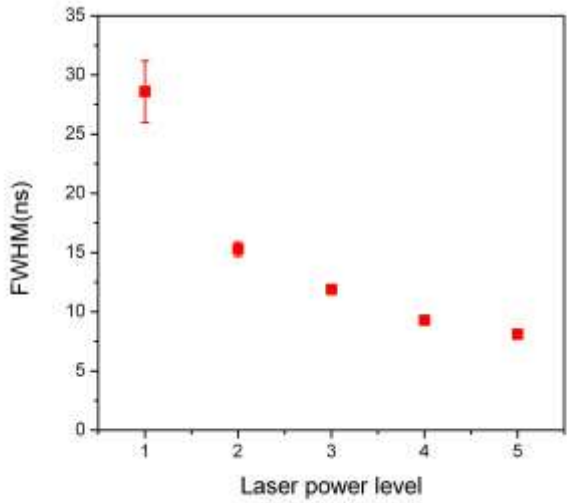

(b)

Figure 5-4 (a) The ratio of intensity variation and (b) FWHM of the laser pulse as a function of the laser power level in the Nd:YAG laser

A low-power continuous laser was used for the probe beam and a fast photodiode detector was used to sense the change in reflectivity induced by the heating pulse. A linearly polarized continuous light was produced from a 2mW He–Ne laser at a 633 nm wavelength, which model is 1122p made by JDSU. The probe beam was passed through a polarizing beam splitter (PBS) and a quarter-wave plate and directed to a sample at normal incidence to minimize the illuminated area. Since

the wavelengths of the pump beam and the probe beam were different, a coaxial geometry was used. The pump and the probe beam were passed through the same objective lens, which simplified the alignment and produced less distorted Gaussian spots.

The reflected probe beam from the surface was aimed toward the quarter-wave plate and the PBS. After crossing the quarter wave plate twice, the polarization plane of the reflected beam was rotated 90 degrees. Then the beam was reflected by the PBS and focused by a lens onto a silicon photodetector, connected to an oscilloscope. For the photodetector, a PDA10A amplified photodetector was used, which is a Si Detector for 200-1100 nm wavelength made by Thorlabs. For the oscilloscope, DSO6102A Oscilloscope was used, which has 2-channel, bandwidth 1 GHz, sample rate 4 GSa/s made by Agilent. A laser line filter was positioned in front of the photodiode to prevent scattered light from the pump beam interfering with detection of the reflected probe beam.

The reflected beam should be guided to a photodetector in order to monitor the reflectivity change of a sample. A low-power laser was used to minimize the heating of a sample. In order to maximize the sensitivity of the reflective signal at a photodetector, we used a linearly polarized laser and a cubic polarizing beam splitter (PBS) and a quarter-wave retardation plate.

In order to explain the roles of the PBS and the quarter-wave plate, Figure 5-5 illustrates two optical configurations. In the case of Figure 5-5(a), a non-polarizing beam splitter is used. With this configuration, the reflected as well as the incident

beam will be split half by the beam splitter, resulting in loss of the intensity of the laser into the photodetector. Therefore, a photodetector collects only one-quarter of the intensity of the incident laser. In the case of Figure 5-5(b), the combination of a polarizing beam splitter (PBS) and a quarter-wave plate is used to maximize the sensitivity. The vertically polarized incident laser transmits through the PBS and is converted into a left-handed circularly polarized wave by the λ/4 plate whose angle is 45°. The light reflected from a sample surface is a right-handed circularly polarized wave, which in turn is converted into a horizontally polarized wave by the same λ/4 plate. Therefore, the vertically polarized incident laser is converted into a horizontally polarized reflected laser after passing through the λ/4 plate twice [59]. The horizontally polarized wave is reflected by the PBS to a photodetector.

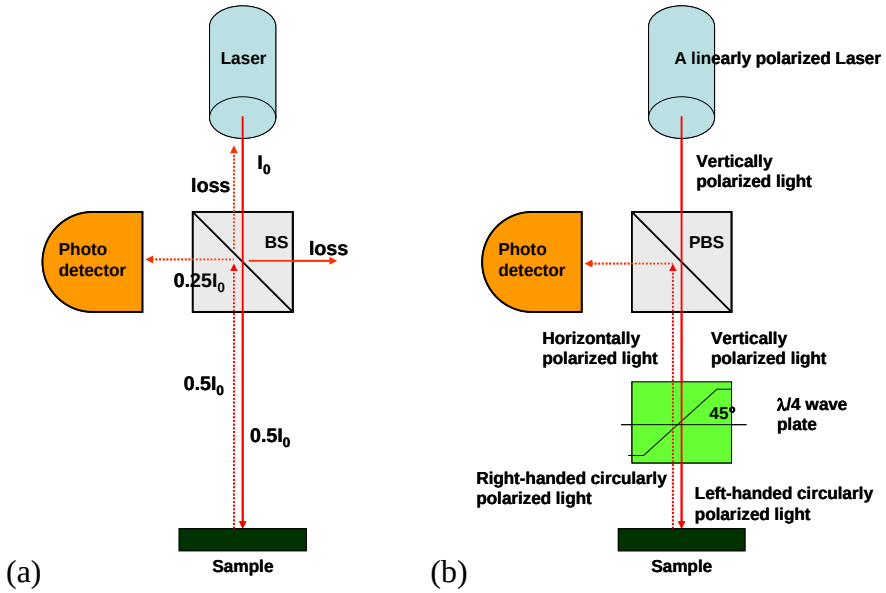

Figure 5-5 Comparison between two types of optical configuration: (a) using a non-polarizing beam splitter and (b) using a polarizing beam splitter and a quarter-wave plate

The overlap of the probe spot and the pump spot on the surface is essential for detecting the thermoreflectance signal. If the pump spot and the probe spot do not overlap at all, the reflectivity change will be zero. In other words, no thermoreflectance signal can be detected without overlapping. The pump spot was expanded to cover a large area and the probe spot was focused to be a small spot. Then, the position of the probe spot was adjusted to be located at the center of the pump spot on the sample surface. The overlap of the probe spot and the pump spot was confirmed by the CCD camera. This large ratio of the pump-probe spot eliminates the effect of varying overlap between the two laser spots.

Another merit of the large ratio of the pump-probe spot is to avoid radial heat spreading effect and to ensure a one dimensional heat transfer [60]. Generated heat from the pump beam can be transported not only at cross-plane direction but also at in-plane direction. This radial heat spreading will make faster thermal decay curve and lower thermal resistance than the true values. The size of the probe spot was minimized through focusing the probe beam exactly on the surface of the sample by adjusting the height of an objective lens. In this setup, the diameter of the probe spot on the surface was measured to be about 25μm using a CCD camera. The size of the pump spot was also expanded to about 250μm. Therefore the ratio of the pump-probe spot size is 10:1, which reduces significantly the radial heat spreading effect [60].

5.3 Sample preparation

Sample structure for the TTR measurement is illustrated with a pump beam

and probe beam in Figure 5-6. The typical sample structure is Au/thin film/Si substrate. Heat is generated at the surface of the Au top layer and passed through the thin film to be measured until Si substrate. The Si substrate plays a role of a heat sink. In current TTR experiments, a metal film on top of the material absorbs the majority of the laser pulse energy near the surface of the film. An Au film was selected as a top absorption layer because its thermoreflectance coefficient is relatively large [61], and its reflectivity is linearly proportional to its temperature in wide temperature ranges [58], and is hardly oxidized in air.

Since gold has high diffusivity as 1.2×10^{-4} m^2s^{-1}, radial heat spreading effect might be severe. In this setup, the duration of heating event was only 10ns. Hence, the thermal spreading distance is 1.1μm, which is much smaller than the pump spot size of 250μm. Therefore, the condition for one-dimensional transport is well satisfied.

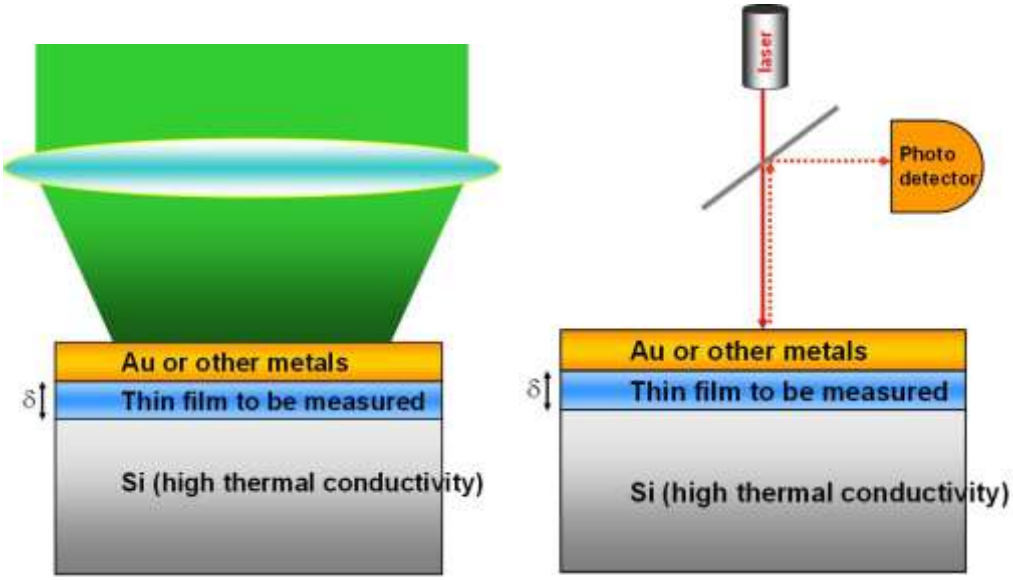

Figure 5-6 Sample structure for the TTR measurement

Two series of samples were made to study the thermal conductivity of the SiN_x films and the thermal boundary resistances at Au/SiN_x and $CoFe/SiN_x$ interfaces. The $Au/SiN_x/Si$ substrate structured samples were made to measure the thermal conductivity of SiN_x films and the thermal boundary resistance at the Au/SiN_x interface. The $Au/CoFe/SiN_x/Si$ substrate structured samples were made to measure the thermal conductivity of SiN_x films and the thermal boundary resistance at the $CoFe/SiN_x$ interface.

The SiN_x films with the thickness range of 50 - 200nm were deposited on Si (100) wafers by RF reactive sputtering using a Si target with an Ar and N_2 atmosphere. The 121nm thick CoFe film was subsequently deposited on the SiN_x film by DC magnetron sputtering using a composite target with a composition of Co 90at% and Fe 10at%. The sputtering of SiN_x and CoFe films was conducted using a RF/DC magnetron sputtering system located in the cleanroom at Carnegie Mellon University [24]. The base pressure of the chamber was less than 5×10^{-7} Torr. A 529nm thick Au film was deposited on the CoFe film or on the SiN_x film by DC sputtering. The Au film was deposited using a Perkin Elmer 6J Sputtering System [24].

6 Analytical solutions for heat diffusion equation

In order to extract the thermal properties from the measured thermoreflectance signals, thermal modeling is required. Analytical solutions were obtained using the analogies between thermal conduction and electrical conduction and applying the transmission-line theory. The detailed procedure to derive the analytical solutions in frequency domain is presented here.

6.1 Introduction

Using the pump-probe method, we can measure the time-resolved reflectance change at the surface of a sample. In order to extract the thermal properties of a thin film from its thermal response, an analytical solution is required. If the temperature of both end of a sample is given, it is straightforward to get the analytical solution for the heat diffusion equation which is described in section 3.5. However in the case of the pump-probe method for the current study, the temperature of the surface of a sample is an unknown variable, which varies in time. In addition, a sample is not a standing alone single film, but has a multilayered structure. In this case, it is very difficult to get an analytical solution for the heat diffusion equation.

Another way to solve the heat diffusion equation for a multilayered structure is to use a numerical method such as a finite differential method. However, a numerical method requires a lot of computing time, which is not appropriate for fitting the

experimental data. Instead, a frequency-domain solution for the multilayered structure can be easily solved using a transmission-line theory. The frequency-domain solution, then, is transformed to the time-domain solution by performing an inverse Laplace transformation. This time-domain solution can be used to fit the experimental data to extract the thermal properties of a film. This work is based on the work by Chen [62].

6.2 Analogies between thermal conduction and electric conduction

The heat flux is proportional to the temperature gradient. In the case of one dimensional heat transport in an isotropic material, the heat flux can be expressed as [33]

$$q_x = -k\frac{\partial T}{\partial x} \qquad 6\text{-}1$$

where q is the heat flux density (W/m^2), T is the temperature (K), k is the thermal conductivity of the material (W/mK). The equation is called as Fourier's law.

Likewise, electric current density is proportional to electric field, which is called Ohm's law [2]. In the case of one dimensional electric transport in an isotropic material, the Ohm's law can be expressed as follows.

$$J_x = \sigma E_x \qquad 6\text{-}2$$

where J is the electric current density (A/m^2), E electrical field (V/m), σ electric conductivity ($1/\Omega m$) of the material.

It is clear that there is an analogy between the heat and electrical conduction expressed by equation 6-1 and 6-2. Based on the analogy, Table 6-1 summarizes the corresponding quantities and properties. The analogy is useful in the analysis of heat transport problems from property measurement to modeling. In modeling, a complicated heat transfer analysis can be simplified by creating an electric circuit.

Table 6-1 Analogies between thermal conduction and electrical conduction

Thermal conduction	Electrical conduction
Temperature, T [K]	Electrical potential, V [V]
Temperature gradient, $\Delta T/\Delta x$ [K/m]	Electrical field, $V/\Delta x$ [V/m]
Heat flux density, q [W/m^2]	Electric current density, J [A/m^2]
Thermal conductivity, k [W/mK]	Electrical conductivity, σ [$1/\Omega m$]

6.3 Apply transmission-line technique

In electric circuits, the length of the wires connecting the components is generally ignored. The voltage on the wire at a given time is commonly assumed to be the same at all points. However, this assumption is not true if the voltage is an AC signal and its wavelength is comparable to or less than the length of the wire. In this case, the length of the wire must be treated as a transmission line, where the phase and the interference with reflection are considered [63, 64].

From the analogies between the heat conduction and electric conduction, temperature T is equivalent to voltage V, and heat flux is equivalent to current density, J(x) or current, I(x) in the case of one dimensional transport.

Then, we can rewrite temperature gradient in the term of voltage and current as follows.

$$\frac{\partial V(s,x)}{\partial x} = -\frac{1}{k} I(s,x) \qquad 6\text{-}3$$

Differentiating Equation 6-3 yields the following equation.

$$\frac{\partial^2 V(s,x)}{\partial x^2} = \frac{\rho c s}{k} V(s,x) \qquad 6\text{-}4$$

where ρ is the density, c is the specific heat of a material, and s is frequency.

Above equation becomes further simplified using a propagation constant, γ.

$$\frac{\partial^2 V(s,x)}{\partial x^2} = -\gamma^2 V(s,x) \qquad 6\text{-}5$$

The propagation constant, γ is defined as $\gamma^2 = s/\alpha$ with diffusivity $\alpha = k/\rho c$.

The general solution for above equation can be expressed as follows [63, 64].

$$V(x) = V^+(0)\exp(-\gamma x) + V^-(0)\exp(\gamma x) \qquad 6\text{-}6$$

where the superscripts + and − represent forward and backward traveling waves, respectively.

Since $I = -k\partial V/\partial x$,

$$I(x) = k\gamma[V^+(0)\exp(-\gamma x) - V^-(0)\exp(\gamma x)] \qquad 6\text{-}7$$

Using the characteristic impedance, $Z_c = 1/k\gamma$, Equation 6-7 can be expressed

as follows.

$$I(x) = \frac{1}{Z_c}[V^+(0)\exp(-\gamma x) - V^-(0)\exp(\gamma x)] \qquad 6\text{-}8$$

Here, the characteristic impedance is defined as the ratio of the amplitude of voltage to current at x=0 without reflections.

$$Z_c = \frac{V^+(0)}{I^+(0)} \qquad 6\text{-}9$$

Since the transmission line is terminated at a load impedance Z_L at x=0 as shown in Figure 6-1, the load impedance must be the ratio of voltage to current at x=0. i.e., $Z_L = V(0) / I(0)$.

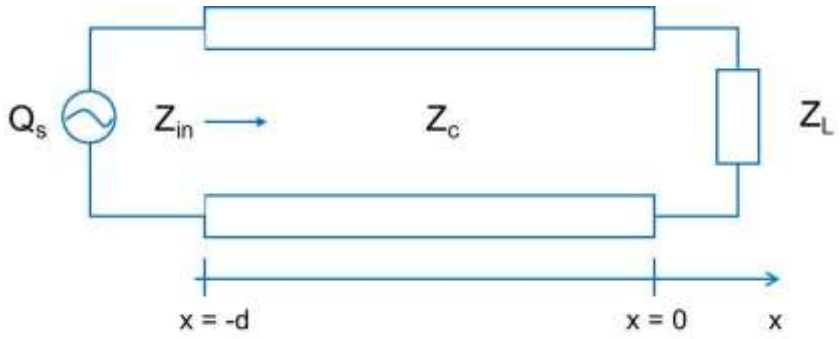

Figure 6-1 Illustration of transmission line for a single layered film; Transmission line with current source Qs is terminated at a load impedance Z_L.

By using Equation 6-6 and 6-8 with x=0, Z_L can be expressed as:

$$Z_L = \frac{V^+(0)+V^-(0)}{V^+(0)-V^-(0)} Z_c \qquad 6\text{-}10$$

Let's introduce a reflection coefficient, Γ which is defined as the amplitude of the reflected voltage wave to the amplitude of the incident voltage wave, i.e., $\Gamma = V^-/V^+$. Then, the reflection coefficient Γ at x = 0 can be expressed from Equation 6-10.

$$\Gamma(0) = \frac{Z_L - Z_c}{Z_L + Z_c} \qquad 6\text{-}11$$

Also, the reflection coefficient Γ at x = -d becomes:

$$\Gamma(-d) = \frac{V^-(0)\exp(-\gamma d)}{V^+(0)\exp(\gamma d)} \qquad 6\text{-}12$$

$$\Gamma(-d) = \Gamma(0)\exp(-2\gamma d) \qquad 6\text{-}13$$

Then, input impedance at x = -d can be expressed as:

$$Z_{in}(-d) = \frac{V(-d)}{I(-d)} \qquad 6\text{-}14$$

$$Z_{in}(-d) = Z_c \frac{V^+(0)[\exp(\gamma d) + \Gamma(0)\exp(-\gamma d)]}{V^+(0)[\exp(\gamma d) - \Gamma(0)\exp(-\gamma d)]} \qquad 6\text{-}15$$

$$Z_{in}(-d) = Z_c \frac{1 + \Gamma(-d)}{1 - \Gamma(-d)} \qquad 6\text{-}16$$

Equation 6-16 can be converted to a following expression with Z_c and Z_L using Equation 6-11 and 6-13.

$$Z_{in}(-d) = Z_c \frac{Z_L[1 + \exp(-2\gamma d)] + Z_c[1 - \exp(-2\gamma d)]}{Z_L[1 - \exp(-2\gamma d)] + Z_c[1 + \exp(-2\gamma d)]} \qquad 6\text{-}17$$

This Equation can be simplified using the hyperbolic tangent function.

$$Z_{in}(-d) = Z_c \frac{Z_L + Z_c \tanh(\gamma d)}{Z_c + Z_L \tanh(\gamma d)} \qquad 6\text{-}18$$

Here the hyperbolic tangent *tanh(x)* is defined as [1-exp(-2x)]/[1+exp(-2x)].

The Equation 6-18 is the input impedance in frequency-domain for a single layered film, which is required for the analytical solution. The load impedance, Z_L,

corresponds to the thermal impedance at the bottom of the film.

6.4 A two-layered model

Since a film is generally required a substrate to support it, usual sample has a film/substrate structure. This two-layered structure is equivalent to a two-component transmission-line as shown in Figure 6-2.

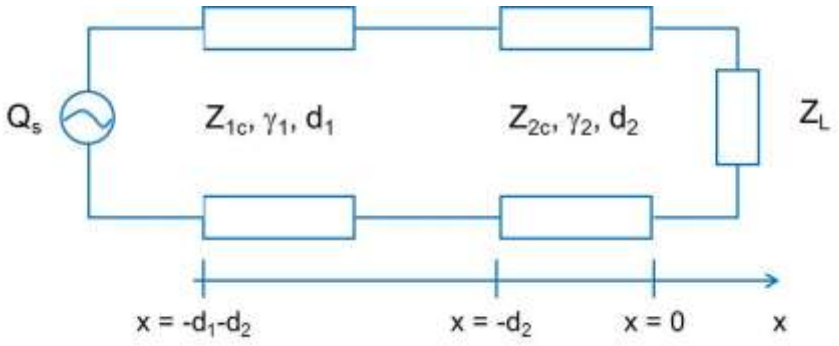

Figure 6-2 Illustration of transmission line for the two-layered structure

In this case, the input impedance $Z_{in}(-d_1-d_2)$ can be expressed from Equation 6-18.

$$Z_{in}(-d_1-d_2) = Z_{1c}\left(\frac{Z_L^{'} + Z_{1c}\tanh\gamma_1 d_1}{Z_{1c} + Z_L^{'}\tanh\gamma_1 d_1}\right) \qquad 6\text{-}19$$

Here,

$$Z_L^{'} = Z_{2c}\left(\frac{Z_L + Z_{2c}\tanh\gamma_2 d_2}{Z_{2c} + Z_L\tanh\gamma_2 d_2}\right) \qquad 6\text{-}20$$

Hence,

$$Z_{in}(-d_1-d_2)=Z_{1c}\left(\frac{\begin{array}{l}Z_{2c}(Z_L+Z_{2c}\tanh\gamma_2 d_2)\\+Z_{1c}(Z_{2c}+Z_L\tanh\gamma_2 d_2)\tanh\gamma_1 d_1\end{array}}{\begin{array}{l}Z_{1c}(Z_{2c}+Z_L\tanh\gamma_2 d_2)\\+Z_{2c}(Z_L+Z_{2c}\tanh\gamma_2 d_2)\tanh\gamma_1 d_1\end{array}}\right) \quad 6\text{-}21$$

However, in many cases a thermal resistance exists located at the interface between the two layers. This thermal resistance can be treated as an extra element R_{th} in series between the two components in the transmission line as shown in Figure 6-3.

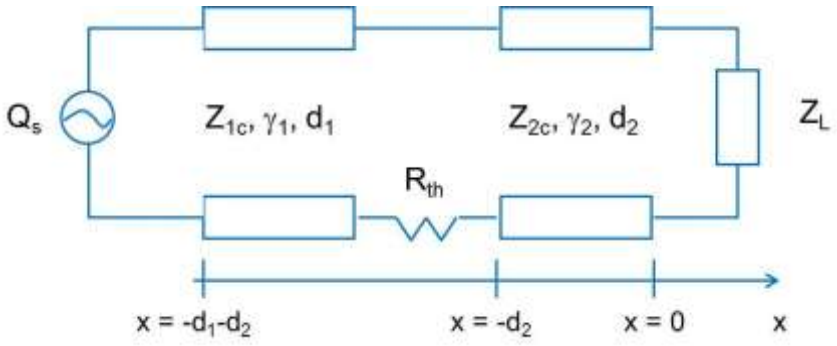

Figure 6-3 Illustration of transmission line for the two-layered structure with a thermal resistance at the interface between a film and a substrate

In this case, R_{th} component is added to Equation 6-20.

$$Z_L^{'}=Z_{2c}\left(\frac{Z_L+Z_{2c}\tanh\gamma_2 d_2}{Z_{2c}+Z_L\tanh\gamma_2 d_2}\right)+R_{th} \quad 6\text{-}22$$

Then, the input impedance $Z_{in}(-d_1-d_2)$ becomes:

$$Z_{in}(-d_1-d_2)=Z_{1c}\left(\frac{\begin{array}{l}Z_{2c}(Z_L+Z_{2c}\tanh\gamma_2 d_2)\\+(R_{th}+Z_{1c}\tanh\gamma_1 d_1)(Z_{2c}+Z_L\tanh\gamma_2 d_2)\end{array}}{\begin{array}{l}Z_{2c}(Z_L+Z_{2c}\tanh\gamma_2 d_2)\tanh\gamma_1 d_1\\+(Z_{2c}+Z_L\tanh\gamma_2 d_2)(Z_{1c}+R_{th}\tanh\gamma_1 d_1)\end{array}}\right) \quad 6\text{-}23$$

Since the thickness of the substrate is infinity thick compared to the thickness

of the film, we can assume isothermal condition at the bottom of the substrate (at x=0). In addition, the thickness of the substrate can be treated to infinity ($d_2=\infty$) compared to the film thickness. Hence, $\tanh(\gamma_2 d_2)= 1$.

Using the above the two boundary conditions, Equation 6-23 can be further simplified.

$$Z_{in}(-d_1 - d_2) = Z_{1c}\left(\frac{Z_{2c} + R_{th} + Z_{1c}\tanh\gamma_1 d_1}{Z_{2c}\tanh\gamma_1 d_1 + Z_{1c} + R_{th}\tanh\gamma_1 d_1}\right) \qquad 6\text{-}24$$

where Z_{1c} and Z_{2c} are the characteristic impedance of layer 1 and layer 2 respectively. d_1 and d_2 are the thickness of layer 1 and layer 2, respectively. γ_1 is the propagation constant of layer 1, defined as $(s/D_1)^{-1/2}$ and s is frequency, $D_1 = k_1/C_v$ the thermal diffusivity with k_1 is the thermal conductivity of layer 1.

For the current study, the film between Au and Si substrate is treated to a thermal resistance, R_{th} in the 2-layered model. This thermal resistance includes the thermal boundary resistance and the volume resistance (d/K) due to the film. The heat capacitance of the film is neglected for this model. The advantage of the 2-layered model is that the information for physical properties of the film, such as the thickness, the density, the heat capacity, and the thermal conductivity, are not required for the modeling. By plotting R_{th} with a few different thickness of the film, the thermal conductivity of the film and the thermal boundary resistance between Au and the film can be extracted.

6.5 A three-layered model

The two-layered model is only valid if the thickness of a film is very thin therefore can be negligible. If the thickness of the film is thick enough, the heat capacity of a film cannot be neglected. In this case, three-component transmission-line model corresponding Au/film/Si substrate is necessary. In this case, the thermal boundary resistance at each interface should be considered too. Three-component transmission-line with 2 resistances is shown in Figure 6-4 for a 3-layered structure.

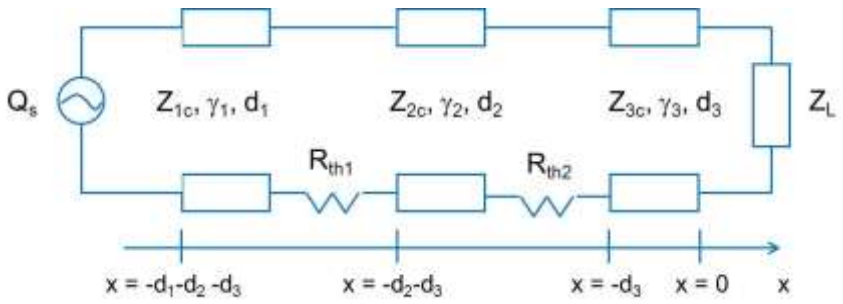

Figure 6-4 Illustration of transmission line for the three-layered structure with thermal resistances

When there is no thermal resistance, the input impedance $Z_{in}(-d_1-d_2-d_3)$ can be expressed as follows.

$$Z_{in}(-d_1-d_2-d_3)=Z_{1c}\left(\frac{Z_L^{'}+Z_{1c}\tanh\gamma_1 d_1}{Z_{1c}+Z_L^{'}\tanh\gamma_1 d_1}\right) \qquad 6\text{-}25$$

Here

$$Z_L^{'}=Z_{2c}\left(\frac{Z_L^{''}+Z_{2c}\tanh\gamma_2 d_2}{Z_{2c}+Z_L^{''}\tanh\gamma_2 d_2}\right) \qquad 6\text{-}26$$

and

$$Z_L^{"} = Z_{3c}\left(\frac{Z_L + Z_{3c}\tanh\gamma_3 d_3}{Z_{3c} + Z_L\tanh\gamma_3 d_3}\right) \qquad 6\text{-}27$$

If the isothermal boundary condition and infinite thick substrate assumption are applied, Equation 6-25 becomes:

$$Z_{in}(-d_1 - d_2 - d_3) = Z_{1c}\left(\frac{\begin{array}{l} Z_{2c}(Z_{3c} + Z_{2c}\tanh\gamma_2 d_2) \\ + Z_{1c}\tanh\gamma_1 d_1(Z_{2c} + Z_{3c}\tanh\gamma_2 d_2) \end{array}}{\begin{array}{l} Z_{1c}(Z_{2c} + Z_{3c}\tanh\gamma_2 d_2) \\ + Z_{2c}\tanh\gamma_1 d_1(Z_{3c} + Z_{2c}\tanh\gamma_2 d_2) \end{array}}\right) \qquad 6\text{-}28$$

In the case of thermal resistance existing, Equation 6-26 and 6-27 should be modified as follows.

$$Z_{L}^{'} = Z_{2c}\left(\frac{Z_L^{"} + Z_{2c}\tanh\gamma_2 d_2}{Z_{2c} + Z_L^{"}\tanh\gamma_2 d_2}\right) + R_{th1} \qquad 6\text{-}29$$

and

$$Z_L^{"} = Z_{3c}\left(\frac{Z_L + Z_{3c}\tanh\gamma_3 d_3}{Z_{3c} + Z_L\tanh\gamma_3 d_3}\right) + R_{th2} \qquad 6\text{-}30$$

Then, the input impedance $Z_{in}(-d_1\text{-}d_2\text{-}d_3)$ can be obtained as follows.

$$Z_{in}(-d_1 - d_2 - d_3) = Z_{1c}\left(\frac{\begin{array}{l} Z_{2c}[(Z_{3c} + R_{th2}) + Z_{2c}\tanh\gamma_2 d_2] \\ + (R_{th1} + Z_{1c}\tanh\gamma_1 d_1) \\ [Z_{2c} + (Z_{3c} + R_{th2})\tanh\gamma_2 d_2] \end{array}}{\begin{array}{l} Z_{1c}[Z_{2c} + (Z_{3c} + R_{th2})\tanh\gamma_2 d_2] \\ + \{Z_{2c}[(Z_{3c} + R_{th2}) + Z_{2c}\tanh\gamma_2 d_2] \\ + R_{th1}[Z_{2c} + (Z_{3c} + R_{th2})\tanh\gamma_2 d_2]\}\tanh\gamma_1 d_1 \end{array}}\right) \qquad 6\text{-}31$$

From the above input impedance, the characteristic impedance and propagation constant are needed to be transformed to a frequency form.

The characteristic impedance Z_c can be expressed using an effusivity.

$$Z_{1c} = \frac{1}{e_1\sqrt{s}}, \quad Z_{2c} = \frac{1}{e_2\sqrt{s}}, \quad Z_{3c} = \frac{1}{e_3\sqrt{s}}$$

Here the effusivity for each layer is defined as follows.

$$e_1 = \frac{k_1}{\sqrt{\alpha_1}}, \quad e_2 = \frac{k_2}{\sqrt{\alpha_2}}, \quad e_3 = \frac{k_3}{\sqrt{\alpha_3}}$$

And

$e_{21} = e_2/e_1$, $e_{31} = e_3/e_1$, $e_{32} = e_3/e_2$.

In addition, the propagation constant for each layer can have the following relations:

$$\gamma_1 d_1 = \eta_1\sqrt{s}, \quad \gamma_2 d_2 = \eta_2\sqrt{s}, \quad \gamma_3 d_3 = \eta_3\sqrt{s}$$

Then, the input impedance for the two-layered model can be converted to a frequency-domain form from Equation 6-24.

$$Z_{in}(-d_1 - d_2) = \frac{1}{e_1\sqrt{s}}\left(\frac{\cosh\eta_1\sqrt{s} + e_{21}\sinh\eta_1\sqrt{s} + R_{th}e_2\sqrt{s}\cosh\eta_1\sqrt{s}}{\sinh\eta_1\sqrt{s} + e_{21}\cosh\eta_1\sqrt{s} + R_{th}e_2\sqrt{s}\sinh\eta_1\sqrt{s}}\right) \quad 6\text{-}32$$

In addition, the input impedance for the three-layered model can be converted to a frequency-domain form from Equation 6-31.

$$Z_{in}(-d_1 - d_2 - d_3) = \frac{1}{e_1\sqrt{s}}$$
$$\left(\begin{array}{l} \cosh\eta_1\sqrt{s}(\cosh\eta_2\sqrt{s} + R_{th2}e_3\sqrt{s}\cosh\eta_2\sqrt{s} + e_{32}\sinh\eta_2\sqrt{s}) \\ + R_{th1}\cosh\eta_1\sqrt{s}[e_3\sqrt{s}\cosh\eta_2\sqrt{s} + (1 + R_{th2}e_3\sqrt{s})e_2\sqrt{s}\sinh\eta_2\sqrt{s}] \\ + \sinh\eta_1\sqrt{s}[e_{31}\cosh\eta_2\sqrt{s} + (e_{21} + R_{th2}e_{21}e_3\sqrt{s})\sinh\eta_2\sqrt{s}] \\ \hline \sinh\eta_1\sqrt{s}(\cosh\eta_2\sqrt{s} + R_{th2}e_3\sqrt{s}\cosh\eta_2\sqrt{s} + e_{32}\sinh\eta_2\sqrt{s}) \\ + R_{th1}\sinh\eta_1\sqrt{s}[e_3\sqrt{s}\cosh\eta_2\sqrt{s} + (1 + R_{th2}e_3\sqrt{s})e_2\sqrt{s}\sinh\eta_2\sqrt{s}]) \\ + \cosh\eta_1\sqrt{s}[e_{31}\cosh\eta_2\sqrt{s} + (e_{21} + R_{th2}e_{21}e_3\sqrt{s})\sinh\eta_2\sqrt{s}] \end{array}\right) \quad 6\text{-}33$$

7 Thermal boundary resistance of Au/SiN_x and CoFe/SiN_x

As mentioned previously, thermal boundary resistance will be a dominant factor for heat conduction in thin films. This study investigates the thermal boundary resistance between metals and dielectrics, particularly at the Au/SiN_x and CoFe/SiN_x interface using an optical pump-probe method based on a TTR technique. In detail experimental setup and sample preparation were addressed previous chapters. Here we presents the thermal modeling based on the analytical solutions derived previous chapter and the experimental results of the thermal conductivity of SiN_x and the thermal boundary resistance at the interface of Au/SiN_x and CoFe/SiN_x.

7.1 Thermal modeling

Here we present overall procedure of implementing thermal models to experimental data, which is based on the work by Chen [62].

The time-resolved thermoreflectance signal represents the transient temperature change since the thermoreflectance signal is linearly proportional to the temperature [58]. Temperature change at the surface of a film in a frequency domain, T(s,-d) is given as [62]

$$T(s,-d) = Q(s)Z_{in}(-d) \qquad 7\text{-}1$$

where Q(s), a heating source, corresponds to the shape of a laser pulse in a

frequency domain. $Z_{in}(-d)$ is the input impedance at the surface and d is the thickness of a film.

Here, we assume that heat is generated at the surface of a sample. In order to verify this assumption, an optical penetration depth is resumed. Light cannot penetrate far into a metal. The intensity decreases exponentially as light propagates through a metal.

$$I = I_0 \exp(-\alpha z) \qquad 7\text{-}2$$

where z is the distance from the surface of a metal and α is the absorptivity of a metal, which is defined as

$$\alpha = \frac{4\pi k}{\lambda} \qquad 7\text{-}3$$

where λ is the wavelength of a light and k is the imaginary part of the refractive index of a metal at the same wavelength.

At 532nm, the refractive index n = 0.467 and k = 2.41 for Au.

Then, $\alpha = 4\pi * 2.41/532 = 0.0569$ [1/nm]

The optical skin depth is defined as the distance δ through which the intensity of a light decreases by a factor 1/e (~36.8%) and can be calculated as:

$\delta = 1/\alpha = 18$nm

Therefore, the assumption of surface heat generation is justified by the fact that the optical skin depth of Au is 18nm at 532nm, which is much less than the thickness of Au layer, 500nm in the current study.

For frequency-domain heating source Q(s), a Gaussian function was used

since the pulse shape of the YAG laser shows a Gaussian profile as shown in Figure 5-3. The Gaussian profile in time-domain and frequency-domain are given respectively [65]:

$$f(t) = \frac{1}{\sigma\sqrt{2\pi}} \exp\left[-\frac{(t-\mu)^2}{2\sigma^2} \right] \qquad 7\text{-}4$$

$$F(s) = \frac{1}{2}\exp(-s\mu + \frac{1}{2}s^2\sigma^2) erfc\left[\frac{1}{\sqrt{2}}(s\sigma - \frac{\mu}{\sigma}) \right] \qquad 7\text{-}5$$

where μ is the time mean value of the peak for a pulse, variance σ is the statistic distribution and is related to the FWHM with $FWHM = 2\sqrt{(2ln2\sigma)}$. The FWHM and μ were measured from the actual pulse shape of the Nd:YAG laser as shown in Figure 5-3.

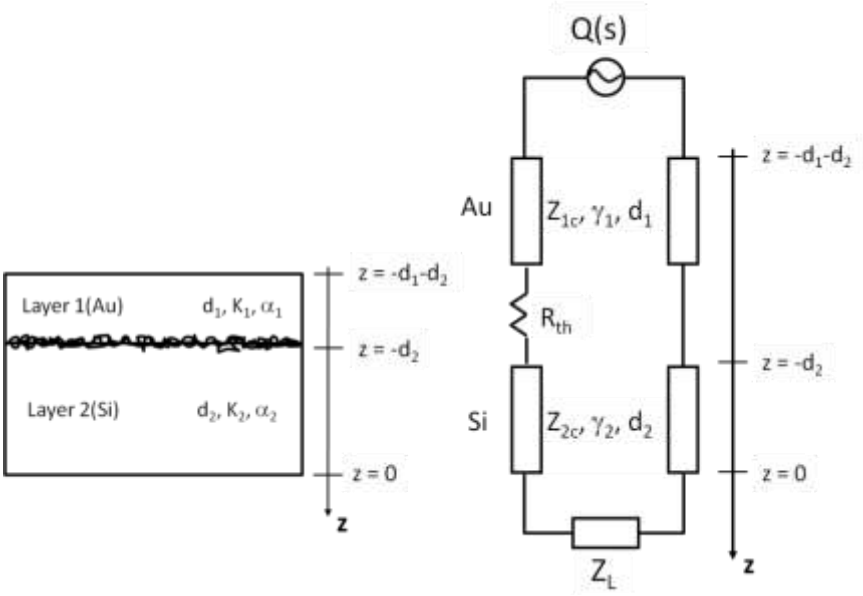

Figure 7-1 Schematic of a layer structure for 2-layer model and its transmission line diagram. Current source, Q(s) corresponds to a heating pulse which hits a sample's surface. Load impedance, Z_L corresponds to a thermal impedance of the bottom of a sample after [62].

If we treat a film as a thermal resistance between Au cap layer and Si substrate as shown in Figure 7-1, the input impedance $Z_{in}(-d_1-d_2)$ is given by Equation 6-24.

$$Z_{in}(-d_1-d_2)=Z_{1c}\left(\frac{Z_{2c}+R_{th}+Z_{1c}\tanh\gamma_1 d_1}{Z_{2c}\tanh\gamma_1 d_1+Z_{1c}+R_{th}\tanh\gamma_1 d_1}\right) \qquad 6\text{-}24$$

Since Q(s) and Zin(-d) are given, the temperature at the surface T(s,-d) can be obtained from Equation 7-1. Since T(s,-d) is a frequency-domain solution, it needs to be inversely Laplace transformed into a time-domain solution since the experimental data are in the time-domain form. This inverse Laplace transformation was performed using Stehfest numerical approximation [66] since there is no exact transformation equation for T(s,-d).

The mathematical formula of the Stehfest approximation is given by [66]

$$f(t)=\frac{\ln 2}{t}\sum_{n=1}^{N}C_n F(s)=\frac{\ln 2}{t}\sum_{n=1}^{N}C_n F\left(\frac{n\ln 2}{t}\right) \qquad 7\text{-}6$$

F(s) is the Laplace transform of f(t).

The coefficient C_n is given by [66]

$$C_n=(-1)^{n+N/2}\times\sum_{k=(n+1)/2}^{\min(n,N/2)}\frac{k^{N/2}(2k)!}{(N/2-k)!k!(k-1)!(n-k)!(2k-n)!} \qquad 7\text{-}7$$

In order to verify the Stehfest method and its implemented algorithm in Matlab, the Gaussian profiles were compared between the exact solution in a time-domain and the converted form from a frequency-domain using the Stehfest method, which results are shown in Figure 7-2. The accuracy of the transformation depends on the N value. Larger N is more accurate, but the transformed result can diverge if N is too large. In all of computation in this study, N=22 were used.

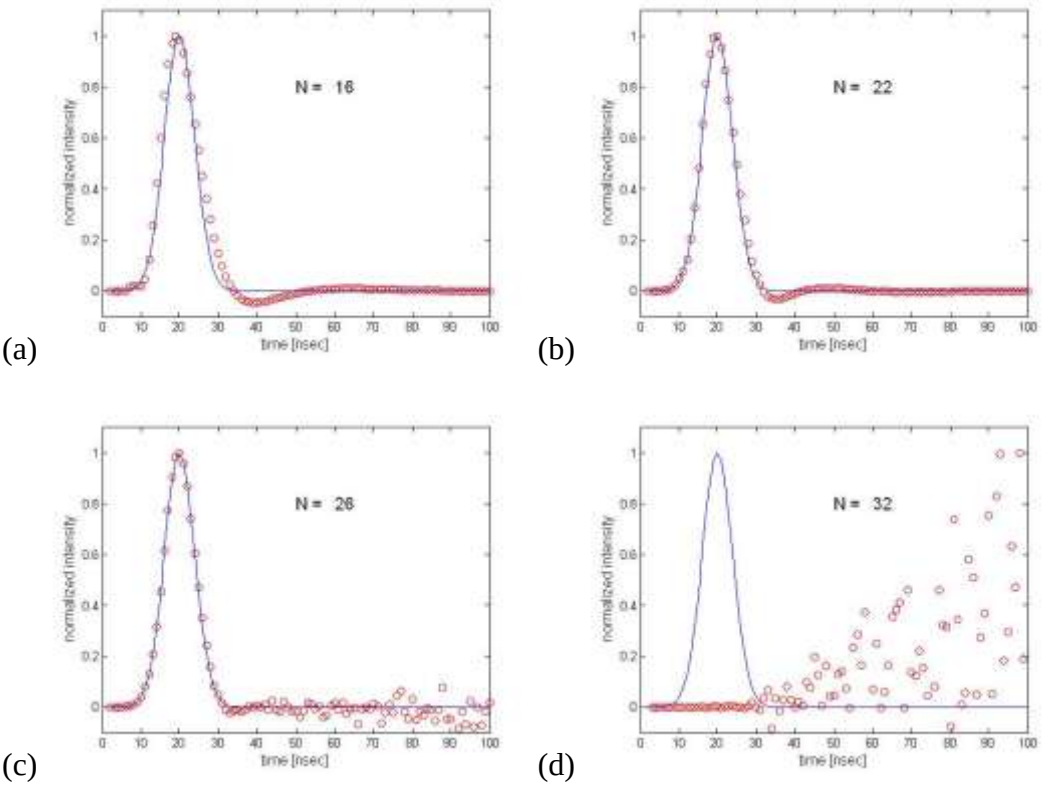

Figure 7-2 Comparison between Gaussian profiles in a time-domain (blue line) and the converted profile from a frequency-domain using the Stehfest method (red circle) with different N values

This transmission-line solution is basically same as the solution described elsewhere [62]. In addition, Kading et al. [67]'s experiment setup is similar to our setup. So we fitted their thermal decay curve with our model and got the same result.

7.2 Experimental results

The thermal decays of the SiN_x films were obtained by performing the thermoreflectance measurement at different thicknesses of the SiN_x films. Figure 7-3 and Figure 7-4 show the experimental data for thermal decay profiles in the Au/SiN_x/Si

substrate structure and the Au/CoFe/SiN_x/Si substrate structure, respectively. For the both figures, the thermal decay slows with increasing SiN_x thickness, indicating increasing thermal resistance.

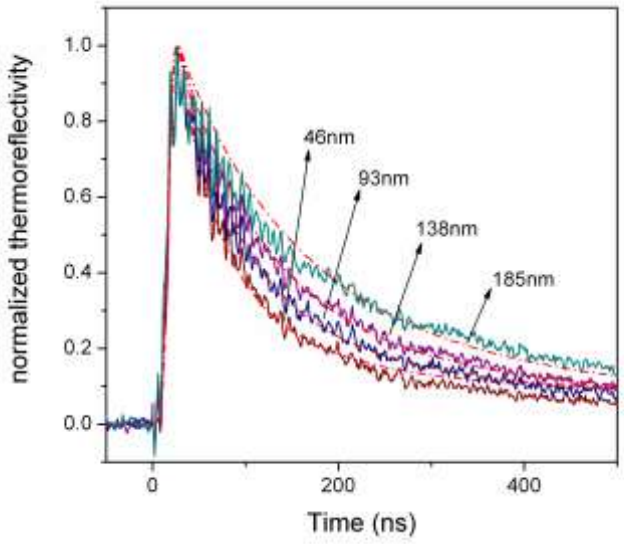

Figure 7-3 Measured transient thermoreflectance signals of Au/ SiNx/ Si substrate for different thickness of SiN_x layer. The solid line is experimental data and the dash line is the fitting curve using the 2-layered thermal model.

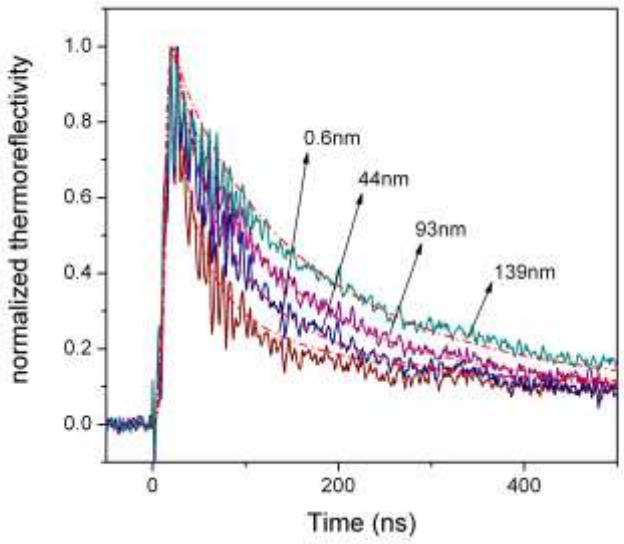

Figure 7-4 Measured transient thermoreflectance signals of Au/ CoFe/ SiNx / Si substrate for different thickness of SiN_x layer. The solid line is experimental data and the dash line is the fitting curve using the 3-layered thermal model.

The thermal resistance of each sample was obtained by fitting the experimental data to thermal models. In order to extract the thermal properties of a thin film from its measured TTR response, analytical solutions were used. For modeling, one-dimensional heat transport and no lateral heat spreading were assumed. In order to confirm one-dimensional transport, the pump-probe spot size ratio of 10:1 and a small thermal spreading distance were employed.

The time-domain solution was fitted with the experimental data to extract the thermal properties of the film. The thermal resistance was the only free parameter of the fitting. For fitting, K = 148W/m·K and C_v = 1.65×10^6J/m^3·K were used as the values of the thermal conductivity and specific heat of the Si substrate, K = 317W/m·K and C_v = 2.49×10^6J/m^3·K as the value of the thermal conductivity and specific heat of the Au film, and K = 90W/m·K and C_v = 3.71×10^6J/m^3·K as the value of the thermal conductivity and specific heat of the CoFe film. There is no appropriate information for thermal properties of CoFe alloy. Thus, the thermal properties of CoFe were assumed between that of Co and that of Fe. The thickness dependence of the thermal conductivity of CoFe was not considered.

The mean free path of CoFe can be roughly estimated using the following equation [2].

$$K = \frac{1}{3} Cvl \qquad 7\text{-}8$$

where C is the electron heat capacity, *v* is the Fermi velocity, and *l* is the mean

free path of an electron.

If the values of C = 1.5×10^4 J/m^{3}K, v = 1×10^6 m/s, K =100W/m·K are substituted into Equation 7-8, the mean free path of CoFe is calculated to about 10nm [68]. Since the mean free path is much smaller than the thickness of the CoFe film, there will be no size effect for the thermal conductivity of CoFe.

In the case of the Au/SiN_x/Si substrate structure, the thermoreflectance signals were fitted using the 2-layered model, which is consisted of 2 layers, Au and Si, and a thermal resistance between them. The thermal resistance consists of the volume resistance of the SiN_x layer, and the boundary resistances at the Au/SiN_x interface and the SiN_x/Si interface.

In the case of Au/SiN_x interface, the primary heat carriers are changed from electrons to phonons at the interface. Thus, electron scattering will occur at the interface and a significant thermal boundary resistance is expected. Meanwhile, in the case of SiN_x/Si interface, the primary heat carriers are phonons. Also, the phonon density of crystalline Si will be much higher than that of amorphous SiN_x. Therefore, the reflection of phonons at the interface will be negligible. Hence, the thermal boundary resistance at SiN_x/Si interface was neglected. Only the boundary resistances at the Au/SiN_x interface and the volume resistance of the SiN_x layer were considered for the thermal resistance in this analysis.

The thermal resistance was plotted as a function of the SiN_x film thickness in Figure 7-5. A linear relationship between the thermal resistance and the SiN_x layer thickness was observed. This linear relationship indicated that there was no thickness

dependence of the thermal conductivity of the SiN_x films. The thickness-independent result of the thermal conductivity is agreed well with a literature [69]. The thickness-independent result indicated that the phonon mean free path is much smaller than the thickness of the SiN_x layer. This indication is reasonable since the thickness ranges of 50nm ~ 200nm of the SiN_x films are much larger than the phonon mean free path of amorphous SiN_x, which is of the order of 1 nm at room temperature [35, 69].

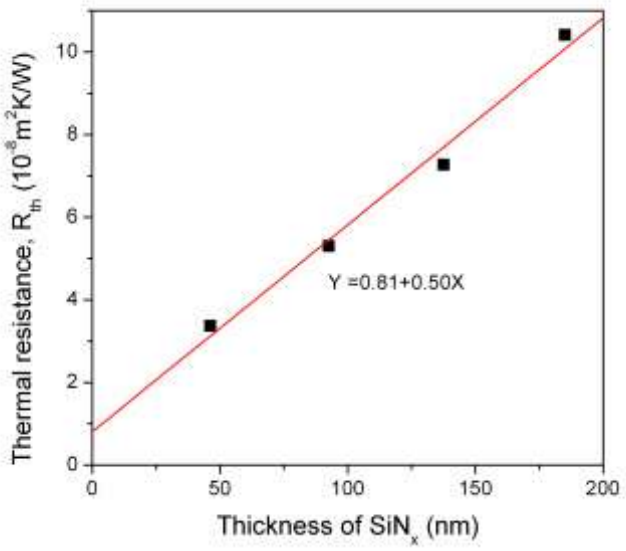

Figure 7-5 Plot of thermal resistance as a function of the thickness of SiN_x layer for Au/ SiN_x / Si substrate structure

Since the thermal resistance was independent of the thickness, the thermal resistance data was then fitted as a linear curve using the least square fitting method. From the linear curve, the value of the thermal conductivities of the SiN_x layers was deduced as the inverse of the slope. The deduced thermal conductivity of the SiN_x film was 2.0 W/m·K at room temperature. This value is quite consistent with the

previous reported value of 2.0 W/m·K for amorphous SiN_x films [69]. From the linear curve, we can get the information of not only the thermal conductivity but also the boundary resistance. When the linear curve is extrapolated to a zero, the intercept value corresponds to the boundary resistance. From the intercept in Figure 7-5, the boundary resistance was calculated as 0.81×10^{-8} m^2K/W for Au/SiN_x.

In the case of the $Au/CoFe/SiN_x/Si$ substrate structure, the 3-layered model was used for the fitting. The model included Au, CoFe, and Si for the 3-layered components and two thermal resistances at the Au/CoFe interface and $CoFe/SiN_x$ interfaces. Since the Au and CoFe are metals, the main carriers for heat transport are electrons. Thus, the thermal boundary resistance between them will be much smaller than that of $CoFe/SiN_x$ [70] and was neglected in this analysis.

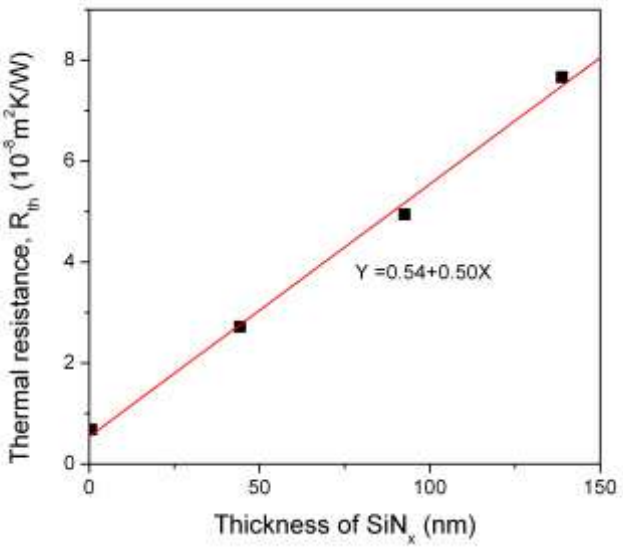

Figure 7-6 Plot of thermal resistance as a function of the thickness of SiN_x for Au/ CoFe/ SiN_x / Si substrate structure

As shown in Figure 7-6, the thermal resistance of $Au/CoFe/SiN_x/Si$ structure

also had a linear relationship with the thickness of the SiN_x layer. From the slope of the linear fitting curve, the thermal resistivity of SiN_x was measured to 2.0 W/m·K. Even though the interfaces are different, the thermal conductivity of the SiN_x layer for both structures remains the same. In addition, from the intercept value of the linear curve, the boundary resistance of CoFe/SiN_x was measured to 0.54×10^{-8} m^2K/W. This value is in the same scale, but a bit smaller than that of Au/SiN_x.

7.3 Discussions

To predict the thermal boundary resistance of interfaces, the acoustic mismatch model (AMM) and the diffuse mismatch model (DMM) have been conventionally used. The AMM assumes perfect interface and elastic scattering at an interface. Meanwhile, the DMM assumes diffusive scattering at an interface [71]. In the DMM, the probability of transmission depends on the ratio of the density of phonon states on both sides of the interface. This diffusive scattering of the DMM is more related to a rough interface or elevated temperature.

In order to calculate thermal boundary resistance at room temperature, a detailed knowledge of the phonon dispersion relationship over the entire Brillouin zone is required [72]. Simplified Debye approximation can be applied only below 30K [55]. Even though it is important to understand the underlying physics by comparing the experimental results with these predictions, this is beyond the scope of this study.

The thermal boundary resistances of various metal-dielectrics are reported in

literatures with the range from 0.1 to 1×10^{-8} m^2K/W at room temperature [70, 71, 73, 74]. The thermal boundary resistance values of 0.81×10^{-8} m^2K/W for Au/SiN_x and 0.54×10^{-8} m^2K/W for CoFe/SiN_x for the current study are located within the literature range.

Within the knowledge of the authors, there is no literature for the thermal boundary resistance between Au and SiN_x. Instead we compared the thermal boundary resistance between Au and the other dielectrics. In the case of the interface between Au and SiO_2, 0.8×10^{-8} m^2K/W was reported for good contact and 4.3×10^{-8} m^2K/W for incomplete contact [67]. Another experiment showed the thermal boundary resistance as 1.8×10^{-8} m^2K/W, but this result did not match with their prediction using the DMM [57]. In the case of the interface between Au and alumina(Al_2O_3) substrate, 1.1×10^{-8} m^2K/W was reported [75].

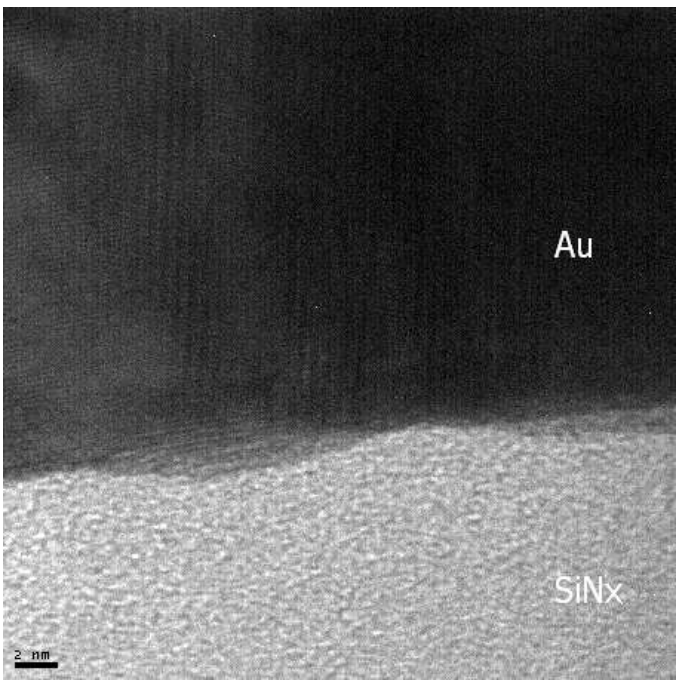

Figure 7-7 Cross-sectional TEM image of Au/ SiN_x interface

Our measured thermal boundary resistance value of 0.81×10^{-8} m^2K/W for Au/SiN_x is very close to the value of Au/SiO_2 for good contact. The cross-sectional TEM image of the Au/SiNx interface in Figure 7-7 confirmed that the interface has good contact.

In the case of CoFe, there is no literature for the thermal boundary resistance for CoFe even though CoFe is one of common materials for magnetic recording. Since CoFe is a transition metal alloy, we compared it with Cr, another transition metal. The thermal boundary resistance of Cr has the range from 0.44 to 0.53×10^{-8} m^2K/W with AlN, Al_2O_3, GaN, and Si [54]. Our measured value of the thermal boundary resistance of 0.54×10^{-8} m^2K/W for $CoFe/SiN_x$ is also agreed well with the literature values. Therefore, the difference of the thermal boundary resistances between Au/SiN_x and $CoFe/SiN_x$ will be caused by the different phonon dispersion of Au and CoFe [72].

Another reason for the different value of the thermal boundary resistance might be different interface roughness [55, 72, 76-78]. The effect of roughness on the thermal boundary resistance has been extensively studied. The influence of roughness to the thermal resistance is positive. The roughness usually increases the resistance [78]. However, quantitative analysis of the relation between the roughness and the resistance is very complicated. We need to find an appropriate method to quantify interface roughness between films. When the characteristic dimension of the roughness is comparable to the wavelength of phonons, phonons scatter most strongly

[55]. Hence, phonon scattering factor, p can be introduced as a function of the ratio of the roughness η to the wavelength λ [79]. The value of p represents elastic or diffusive scattering at the interface. Using p, the influence of roughness on the mean free path and thermal conductivity can be quantized.

The interface roughness of Au/SiN_x and CoFe/SiN_x were examined using cross sectional TEM images. The cross-sectional image of Au/SiN_x interface is already shown in Figure 7-7. Figure 7-8 shows the cross-sectional image of CoFe/SiN_x interface. The both interfaces show similar roughness. It is hardly quantify the roughness difference between the two interfaces.

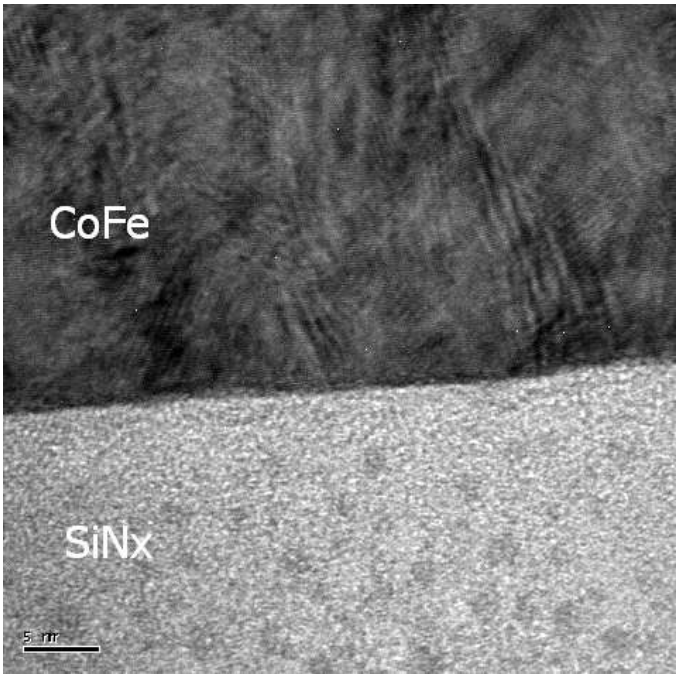

Figure 7-8 Cross-sectional TEM image of CoFe/SiN_x interface

7.4 Summary

The thermal conductivity of SiN_x dielectric layer and the thermal boundary

resistance of Au/SiN_x and CoFe/SiN_x were measured using the transient thermoreflectance technique. We built an optical pump-probe measurement system using a nanosecond pulse laser and a continuous-wave probe laser. The thermal analysis of the experimental data was performed by fitting them with the analytical solutions which are based on the transmission-line theory.

The results of the thermal conductivity and thermal boundary resistance are consistent with the literature values. In addition, the thermal boundary resistance at the metal/SiN_x interface was found to be important for the heat transport. The thermal conductivity of SiN_x does not depend on the thickness in the thickness range of 50 ~ 200nm. The thermal boundary resistance at metal/SiN_x interfaces will impact overall thermal conduction in electronic devices when the thickness of SiN_x thin films is reduced. For example, apparent thermal conductivity of SiN_x film becomes half of the intrinsic thermal conductivity when the thickness decreases to 16nm. Therefore, it is advised that the thermal boundary resistance between metal and dielectrics should be counted in nano-scale electronic devices.

The thermal boundary resistance of Au/SiN_x and CoFe/SiN_x is different. The difference could be come from the different phonon dispersion of Au and CoFe.

8 Size effect of Cu films

The thickness of each layer in the spin-valve structured multilayer in the current study is a few nanometers. Meanwhile electron mean free path for each metal layer of the spin-valve is usually 10 times larger than the thickness of each layer. Hence, the electric conduction is under the size effect. In this chapter, the size effect is reviewed and the preliminary results for Cu films are presented.

8.1 Introduction

Electric conduction phenomena in metals have been widely studied in the case of metals' physical dimension is comparable to the electron mean free path. As the physical dimension decreases of the order of the mean free path of electrons, the electric resistivity rapidly increases. This classical size effect [80] could be crucial in the evolution of micro- or nano-electronics since the dimension of the Cu interconnected lines approach of the same order of the electron mean free path.

The classical size effect of electric resistivity was observed in copper films at room temperature. In order to analyze the experimental data, electric resistivity models were carefully reviewed. Electron mean free path, surface and grain-boundary scattering effect of copper films were interpreted through appropriate models and compared with some published data.

8.2 Overview of size effect

The mean free path or the size effects in the electric transport properties of thin metal films have been studied extensively. The size effect was first analyzed by Thomson by using a mean free path and film thickness [80]. This model has been modified and extended by others, including Fuchs [81] and Sondheimer [82]. The Fuchs-Sondheimer (F-S) model [81, 82] added the distribution functions of the conduction electrons and the character of the scattering at the film surface. The scattering can be diffuse or elastic (specular) with a probability of 1-p, where p is the specular scattering coefficient. However, the F-S model ignores the grain-boundary scattering effect.

The effect of grain-boundary on the resistivity of metals may be little if the grain size is much larger than the mean free path. However, in the case of polycrystalline thin films, the grain size usually scales with the film thickness. Therefore, in a certain thickness range, the distance between grain boundaries becomes smaller than the mean free path and the grain-boundary scattering cannot be ignored. The contribution of grain-boundary scattering to the resistivity was included in the model proposed by Mayadas and Shatzkes [83]. This Mayadas-Shatzkes (M-S) model [83] treated a grain-boundary as an internal surface with grain boundary reflection coefficient R. Here the grain boundary is assumed to lie perpendicular to the film plane. Since the grain-boundary scattering term is added to the M-S model, the resistivity will increase more rapidly with decreasing thickness than what would be predicted from the F-S model.

8.3 Experimental procedure

The mean free path can be determined by an analysis of the thickness-dependent resistivity. In order to observe the size effect, copper films of thickness ranging from 10 to 500nm were prepared by DC sputtering a high purity (99.999%) copper target onto a glass substrate at room temperature. The films were prepared using sputtering facilities in a cleanroom at Western Digital by Dr. Kageeporn Wongpreedee. The base pressure of the chamber was less than 4×10^{-5} Pa. Subsequently, 2nm thick carbon film was deposited on the top of the copper film to protect the copper film from oxidation.

(a) 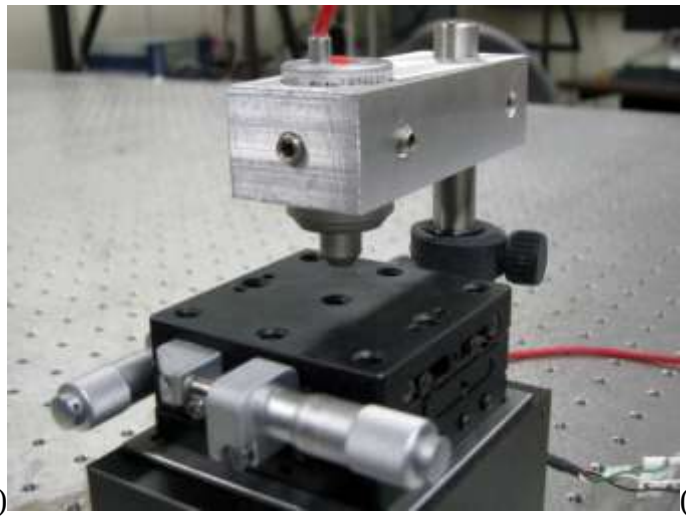 (b) 

Figure 8-1 (a) Four-point measurement setup for wafer resistivity and (b) its four-point probe

The electric resistivity of the copper films was measured using four point probe configuration and DC current input at Carnegie Mellon University. Figure 8-1

shows the photo of the four-point measurement of wafer resistivity with the probe, which was made by Jandel [84]. 10mA as input current was applied to samples to avoid power dissipation. At least 4 different positions of samples were measured.

For the measurement of wafer resistivity, sheet resistance (ohm/square) was measured using the following equation [85].

$$R_s = \frac{\rho}{d} = \frac{\pi}{\ln 2}\frac{V}{I} \qquad 8\text{-}1$$

where ρ is the resistivity and d is thickness of a film. V is an output voltage and I is an applied current.

8.4 Results and discussions

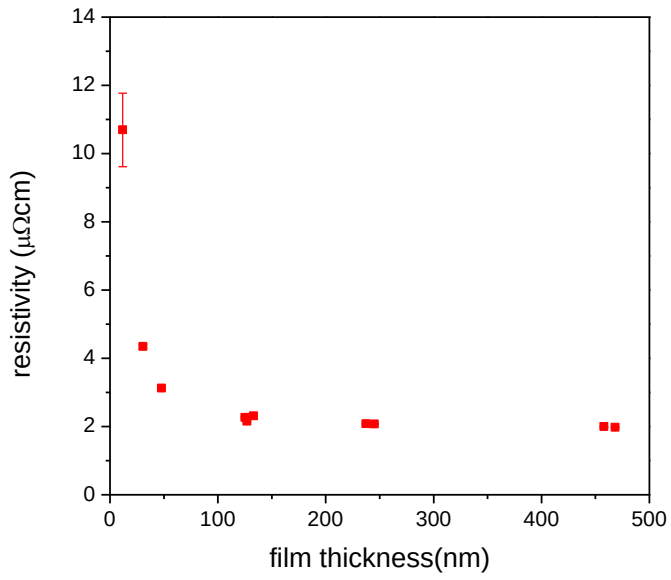

Figure 8-2 Plot of electric resistivity as a function of the thickness of the copper films at room temperature

Figure 8-2 shows the electric resistivity as a function of the copper films at

room temperature. The electric resistivity increases as the thickness decreases. This thickness-dependent electric conduction is commonly called the size effect of metals.

In order to interpret the size effect, the F-S model was employed here. The F-S model can be expressed as following equation [81, 82].

$$\rho_f = \rho_i \left\{ 1 - \frac{3(1-p)}{2k} \int_1^\infty \left(\frac{1}{x^3} - \frac{1}{x^5} \right) \frac{1-\exp(-kx)}{1-p\exp(-kx)} dx \right\}^{-1} \qquad 8\text{-}2$$

where ρ_f is the apparent resistivity of a film and ρ_i is the intrinsic resistivity. The variable k is $d\backslash\lambda_i$ and d is the thickness and λ_i is the intrinsic mean free path of a film. Intrinsic means here as infinitely thick thus thickness-independent. The variable x is $1/\cos\theta$. p is the specularity parameter, representing the fraction of electrons specularly reflected at the film surface ($0 \le p \le 1$). p=1 indicates specular (elastic) scattering at the surface of films and no size effect for resistivity. p=0 indicates completely diffuse scattering of electrons at the surface of films [86-88].

If the thickness of a film is much larger than the intrinsic mean free path ($k >> 1$), Equation 8-2 can be simplified as follows [89, 90].

$$\rho_f = \rho_i \left[1 + \frac{3}{8}(1-p)\frac{\lambda_i}{d} \right] \quad (k >> 1) \qquad 8\text{-}3$$

For the analysis of the experimental data, Equation 8-3 is multiplied by d to get the following expression.

$$\rho_f d = \rho_i \left[d + \frac{3}{8}(1-p)\lambda_i \right] \qquad 8\text{-}4$$

From Equation 8-4, plotting of (ρ_fd, d) gives us the information of ρ_i and λ_i. The slope of the straight line represents the intrinsic resistivity ρ_i and the intercept of

the y-axis represents $\frac{3}{8}(1-p)\frac{\lambda_i}{d}$. Figure 8-3 shows the plot of the ($\rho_f d$, d) for the experimental data of the copper films in the current study.

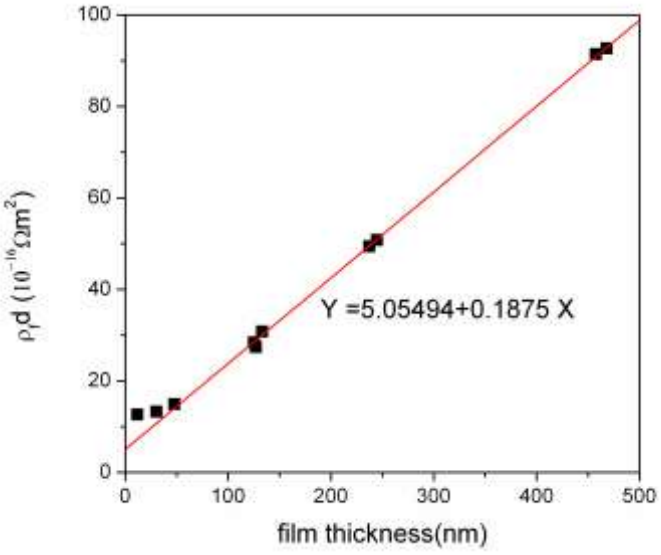

Figure 8-3 Plot of $\rho_f d$ as a function of the thickness d for Cu films at room temperature

From the slope, the intrinsic resistivity is obtained to 1.875×10^{-8}ohm·m for these films. According to Matthiessen's rule [91], many kinds of electron-scattering processes will contribute to the resistivity and be additive. Therefore the film resistivity can be expressed as

$$\rho_i = \rho_L + \rho_{extra} \qquad 8\text{-}5$$

ρ_L is the resistivity due to electron-phonon (lattice) scattering. ρ_{extra} is an extra resistivity due to scattering from impurities, defects, or grain boundaries.

The ρ_L resistivity of a copper is reported as 1.70×10^{-8}ohm·m at room temperature [2], which considers only the contribution of electron-phonon scattering

and excludes impurities contribution. If the value of ρ_L is applied to Equation 8-5, the resistivity contributed from the others is 0.175×10^{-8}ohm·m, which is approximately 9% of the total resistivity. This 9% does not contribute to the size effect of the resistivity.

From the intercept of the y-axis, the intrinsic mean free path λ_i can be obtained with the assumption of completely diffused scattering (p=0).

$$\lambda_i = \frac{8}{3}\frac{5.055\times10^{-16}\Omega m^2}{\rho_i(=1.875\times10^{-8}\Omega m)} \approx 71.9nm \qquad 8\text{-}6$$

Since the values of the intrinsic resistivity and intrinsic mean free path were obtained, the experimental data were fitted using the F-S model with p=0 in Figure 8-4. In Figure 8-4, the thickness-dependent resistivity of the Cu film was plotted by using the Full version of the F-S model expressed in Equation 8-2. The simplified version of the F-S model in Equation 8-3 may not be appropriate since the thickness range of the films for the current study is comparable to the intrinsic mean free path.

Figure 8-4 shows that the fitting curve matches well with the experimental data. The F-S model predicted that the resistivity would increase when the thickness of the films decreases. However, it is worthwhile to point out that the experimental data in Figure 8-3 start departure from the fitted straight line when the thickness is less than 50nm. Equation 8-4 and the straight line are only valid when the thickness of films is larger than the mean free path. Therefore, the departure from the straight line might indicate the mean free path. In addition, the mean free path of copper films was reported as 45.0nm [92] or 39nm [93].

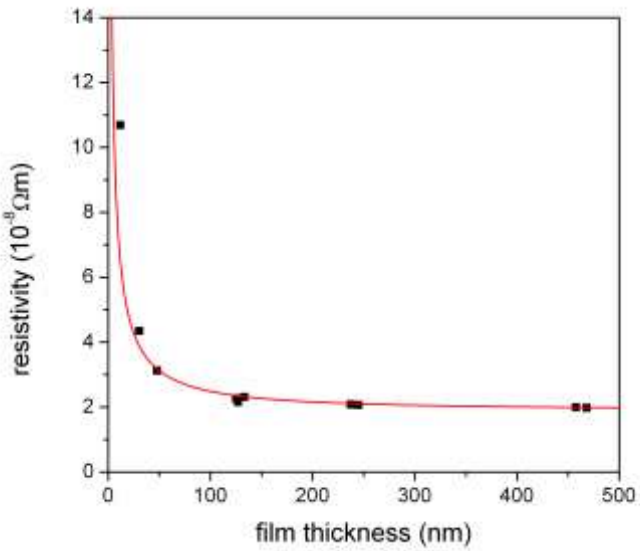

Figure 8-4 Fitting the thickness dependent resistivity of Cu films using the F-S model with p=0

In order to verify the mean free path, we calculated the intrinsic mean free path using another way. According to the free-electron-gas theory of Drude-Sommerfeld [2, 94], the intrinsic mean free path and the intrinsic electric resistivity are not independent. The product of the intrinsic mean free path and the intrinsic electric resistivity can be expressed as follows.

$$\rho_i \lambda_i = \frac{h}{2e^2}\left(\frac{3}{\pi n^2}\right)^{1/3} \qquad 8\text{-}7$$

where h is Planck's constant, e is the electronic charge, n is electron concentration.

Since the electron concentration of copper at room temperature is $8.45\times10^{28}/m^3$ [2], $\rho_i\lambda_i$ of copper is calculated as $6.6002\times10^{18}\Omega m^2$ at room temperature.

If we use the intrinsic resistivity ρ_i =1.875×10^{-8}ohm·m which is obtained from Figure 8-3, the mean free path is calculated as 35.2nm. Even we use the lattice resistivity ρ_L=1.70×10^{-8}ohm·m, the mean free path is calculated as 38.8nm. The obtained mean free path is almost two times larger than the calculated value using the intercept. Meanwhile the 39nm is a commonly used value for the mean free path of copper.

If 35 ~ 39nm is used as the mean free path value, the prediction of the F-S model is considerably departure from the experimental data. The failure of the F-S model was reported elsewhere [93, 95]. The reason for the failure could be that the F-S model does not include the grain-boundary scattering as mentioned in the previous section.

The resistivity due to the grain-boundary scattering ρ_{gb} can be expressed [83]:

$$\rho_{gb} = \rho_{in}\left\{3\left[\frac{1}{3}-\frac{1}{2}\alpha+\alpha^2-\alpha^3\ln(1+1/\alpha)\right]\right\}^{-1} \qquad 8\text{-}8$$

where $\alpha = \frac{\lambda_i}{d}\frac{R}{1-R}$ and R is the reflection coefficient related to the reflection from a grain boundary.

Grain-boundary scattering term is included in the M-S model, which is expressed as [83]:

$$\rho_f = \left\{\frac{1}{\rho_{gb}} - \frac{6(1-p)}{\pi k\rho_{in}}\int_0^{\pi/2} d\phi\int_1^{\infty}\frac{\cos^2\phi}{H^2}\left(\frac{1}{x^3}-\frac{1}{x^5}\right)\frac{1-\exp(-kxH)}{1-p\exp(-kxH)}dx\right\}^{-1} \qquad 8\text{-}9$$

Here,

$$H(t,\phi) = 1 + \frac{\alpha}{\cos\phi\sqrt{1-\frac{1}{x^2}}} \qquad 8\text{-}10$$

Mayadas and Shatzkes [83] formulated the analytical expression for the grain-boundary resistivity and applied it to the Boltzmann equation. The resultant expression is the sum of grain-boundary resistivity and the resistivity from the F-S model. It is worthwhile to point out that Equation 8-9 is not simple addition of the two resistivities. Actually, the grain-boundary resistivity cannot be simply added to the lattice resistivity. Since the film thickness and the grain size is interrelate and dependent, Matthiessen's rule [91] cannot be hold here. Simply adding Equation 8-9 into equation 8-2 or 8-3 is not appropriate, which often mistaken in many papers.

To conclude, there is much uncertainty about the mean free path of copper films even though large amount of published papers. For the current study, we observed thickness-dependent electric resistivity change for copper films. The mean free path of copper film in the current study was calculated to 35nm. The experimental data was interpreted using the F-S model. However, for appropriate interpretation, the effect of grain-boundary scattering should be included using the M-S model, but it is out of scope for the current study.

9 Conclusions and future work

The present work has considered the possibility of spin-dependent heat transport in a magnetic nanostructure. Specifically, Co/Cu/Co multilayered spin-valve structure has been studied. In this investigation, both thermal conductivity change and electric resistance change as a function of magnetic field were studied at the same time. In order to measure the thermal conductivity of thin films, a three-omega method was employed. For this method, a thermally isolated rod in microscale was fabricated and was wire-bonded. In addition, other thermal conductivity measurement methods such as a steady-state joule heating method and a transient thermoreflectance method were examined. The variations in the thermal conductivity and electric resistance were measured by sweeping a magnetic field from a positive maximum strength to a negative maximum strength. Issues of correlation between spin-dependent thermal conduction and electric conduction were examined. The key scientific and engineering implications will be discussed and summarized below, followed by future works.

9.1 Conclusions

The first study in this thesis was to develop a reliable technique to measure the change in the thermal conductivity with different magnetic configurations of multilayered thin films. Different techniques were explored including a three-omega technique, a transient thermoreflectance (TTR) technique, and a steady-state joule

heating technique. The TTR technique in this study gave the information of the thermal conductivity of thin films, but the measurement resolution is not good enough to detect the change in the thermal conductivity with different magnetic configuration. In the case of the steady-state joule heating technique, there are some practical and fundamental issues for measuring the change in the thermal conductivity with different magnetic configuration. The practical and fundamental issues were discussed in detail in Chapter 4. For the case of the three-omega technique, there is no practical and fundamental problem. The technique uses electric resistance change due to joule heating as the steady-state joule heating method does. However, the three-omega technique is a transient method, which detects a frequency component of the resistance change. Therefore, the three-omega technique has much higher sensitivity than that of the steady-state method and the TTR method, and provides the most reliable data. Another benefit of the three-omega method is to able to measure electric conduction at the same time.

Another study in this thesis was to develop a spin-valve structure, which has a high MR ratio and a low saturation field. The Co/Cu/Co multilayered structure was investigated for this purpose. Different layered structures with different materials were explored including Co/Cu/NiFe, Co/Cu/[Co/NiFe/Co], Co/Cu/CoFe, CoFe/Cu, Co/Cu, and Co/Ru. Some of them were patterned to a four-point probe structure, and some of them were not patterned. All of the above layered structures gave MR curves and some MR ratios, but the Co/Cu structure gave the highest MR ratio.

For the Co/Cu structure, the thickness of the Cu layer was a critical factor to

affect the MR ratio and the saturation field. The effect of the thickness of Cu layer was examined intensively. 21Å thick Cu layer gave the highest MR ratio but had a leakage problem with a 27nm thick oxide coated Si substrate. On the 27nm thick oxide coated Si substrate, 34Å thick Cu layer gave the best result.

The low saturation field for the Co/Cu structure was achieved by using different coercivity of the two ferromagnetic layers. In this study, the second Co layer was two times thicker than that of the first one. The thick Co layer has larger magnetic moment and coercivity than the thin one.

As pointed out earlier, the sample should be a thermally isolated rod for the three-omega technique. A four-point probe bridge structure was patterned by using an optical lithography process. Then, Au films were deposited on pad regions using a lift-off process. Next, two trenches were made at the side of the bridge regions. Then, Si substrate under the bridge regions was undercut by XeF_2 etching. After removing the remaining photoresist, the Au pads were wire-bonded for electric contact. The release of the bridge was physically examined by optical microscopy and SEM.

The spin-valve sample was fabricated as a form of a thermally isolated bridge with a Co/Cu/Co multilayer. The 3ω voltage signal of the sample was measured with gradually changing a magnetic field from 650 Oe to -650 Oe and vice versa. The frequency dependency of the measurement was conducted at a wide range of frequency.

From the experimental data, the information of the thermal conductivity was obtained by performing thermal analysis. For the thermal analysis, the closed form of

the analytical solution, which was developed by the Lu et al. [47] and Dames et al. [48], was employed. This solution shows the relation between 3ω voltage and applied current, and the frequency dependence of the 3ω voltage. These relations were used to verify the reliability of the measured 3ω voltage signals in this study. Using the frequency dependence, the fundamental issue from DC joule heating was solved.

Finally, we observed significant change in the thermal conductivity depending on the magnetic configuration. The relative ratio of the magneto thermal conductivity was 50%, which is much higher than 8.0% of the magnetoresistance. The observed thermal conductivity change is closely correlated with that of the electric conductivity in terms of the magnetic configurations, but the thermal conductivity is much more sensitive than that of the electric conductivity. This suggests that the scattering mechanism is different for heat or charge transport [9, 39]. Also the results show that the Lorentz number is spin-dependent.

In addition to the spin-dependent heat transport, this thesis focused on heat transport of thin films in cross-sectional direction. In nanoscale multilayered structures, thermal boundary resistance could dominate the overall heat transport rather than the thermal properties of each individual layer. This study investigates the thermal boundary resistance between metals and dielectrics, particularly at the Au/SiN_x and $CoFe/SiN_x$ interface using a TTR technique.

The merit of the TTR method is that a sample is not required of a patterning process, which needs a lot of effort for fabricating process. We built an optical pump-probe measurement system based on the TTR technique. Energy or heat was

pumped to a sample for a very short time by a pump laser and the resulting transient thermal response of the sample was monitored by a probe laser. A number of TTR systems can exist depending on the pulse width or modulation frequency of the pump laser and the scheme of probing. In this study, a nanosecond pulse laser was used as the pump beam and the resulting transient thermal response was monitored by detecting a time-resolved thermoreflectance signal using a continuous-wave laser and an oscilloscope.

One of the first tasks for the thermal boundary resistance study was to build the pump-probe measurement system. The two laser beams should be overlapped on the surface of a sample in order to produce a thermoreflectance signal. In order to detect the transient thermal response, the reflected probe beam ought to be guided to a photodetector without blocking any optical path. The overlapping of the two beams was possible by using two dichroic mirrors or two semitransparent mirrors. The guiding of the reflected beam was feasible by using a polarizing beam splitter and a quarter wave plate with high efficiency.

In order to extract thermal properties from the transient thermal response, a thermal analysis is required. For the thermal analysis and its modeling, one-dimensional heat flow in cross-sectional direction is assumed. Generated heat from the pump beam can be transported not only in a cross-plane direction but also in an in-plane direction. If only the cross-plane directional heat flow is considered for the thermal analysis, analyzed thermal properties would be different from the true values. The radial heat spreading will make thermal decay curve faster and thermal

resistance lower than the true values. In order to minimize the radial heat spreading effect, the ratio of the spot size of the pump beam and probe beam should be considered. In this study, the ratio of the pump-probe spot size was 10:1 by expanding the pump spot size. This reduces significantly the radial heating effect [60].

For the thermal modeling, a transmission-line concept was employed. In the transmission-line concept, voltages on the wire are not treated as the same over all locations. In addition, the transmission-line concepts consider the phase and reflection of the voltage signals. Since there is an analogy between heat and electric conduction, the transmission-line concept can be applied to heat conduction. Using the concept, analytical solutions of a two-layered structure and a three-layered structure with thermal resistances were derived in a frequency-domain. Then, the frequency-domain solution was transformed to a time-domain solution by performing an inverse Laplace transformation using Stehfest numerical approximation [66]. Using the thermal models, experimental data were fitted to obtain the thermal conductivity of a film and the thermal boundary resistance at an interface.

Time-resolved thermoreflectance signals from Au/SiN_x and $CoFe/SiN_x$ were measured using the pump-probe system. By fitting the experimental data with the thermal models, the thermal conductivity of SiN_x dielectric layer and the thermal boundary resistance of Au/SiN_x and $CoFe/SiN_x$ were obtained. The thermal conductivity of SiN_x films was measured to 2.0 W/mK for both structures. In the case of the thermal boundary resistance, it was 0.81×10^{-8} m^2K/W at the Au/SiN_x interface and 0.54×10^{-8} m^2K/W at the $CoFe/SiN_x$ interface, respectively. The measured values

of the thermal conductivity and thermal boundary resistance are consistent with the literature values.

As pointed out earlier, the thermal boundary resistance at the metal/SiN_x interface would be critical when heat is transport in thin film structures. The thermal conductivity of SiN_x does not depend on the thickness in the thickness range of 50 ~ 200nm. However, the thermal boundary resistance at metal/SiN_x interfaces will impact overall thermal conduction when the thickness of SiN_x thin films is in a nanometer order. For example, apparent thermal conductivity of SiN_x film becomes half of the intrinsic thermal conductivity when the thickness decreases to 16nm. Therefore, it is advised that the thermal boundary resistance between metal and dielectrics should be counted in nano-scale electronic devices.

The thermal boundary resistance at Au/SiNx and CoFe/SiNx was different. In order to understand the origin of the difference, literature survey and cross-sectional TEM analysis were conducted. The difference could be come from the different phonon dispersion of Au and CoFe.

9.2 Future works

Using the three-omega system, we observed spin-dependent heat transport. The ratio of the thermal conductivity is much higher than the ratio of electric resistivity. This result indicates that the Lorentz number in Weidemann-Franz law is also spin-dependent. However, this experiment was performed at room temperature. Since the electric resistivity and the Lorentz number are temperature dependent [4,

43-45], the spin-dependent heat transport will be temperature dependent. At low temperature, the GMR effect increases due to limiting spin intermixing [46]. Therefore, GMTR effect is also expected to be increased.

In order to use the three-omega method, a sample is required to be fabricated as a form of a thermally isolated rod. In addition, the measured electric and thermal conduction is in an in-plane direction. A current-in-plane (CIP) geometry spin-valve was already substituted by a current-perpendicular-to-the-plane (CPP) geometry spin-valve [96, 97]. Also the non-magnetic metal space layer was substituted by an oxide layer such as MgO_x, AlO_x, and TiOx, which is called a magnetic tunnel junction (MTJ) [98]. Magnetoresistance using the MTJ is called tunneling magnetoresistance (TMR) effect. Therefore spin-dependent heat transport at a CPP geometry TMR structure is demanded for wide applications.

For the cross-sectional conduction in the TMR, the pump-probe system has more benefit. However, the nanosecond pump laser with a time-resolved probing thermometry has a limitation for the resolution and sensitivity. In order to improve the resolution and sensitivity, a modulated femtosecond laser pumping with a delay system [99, 100] can be one solution. Here we present the possible schematic for the pump-probe system with a femtosecond laser and a delay line in Figure 9-1. A 100fs pulse laser with 800nm wavelength is shined on a sample surface to generate heat. The transient thermal response will be detected by using a pulse laser with 400nm wavelength. Using a delay line, the probing time is controlled. By using the modulation of the laser with a lock-in amplifier, the sensitivity can be improved a lot.

The other benefits of this system are that no gold cap layer or no patterning is needed.

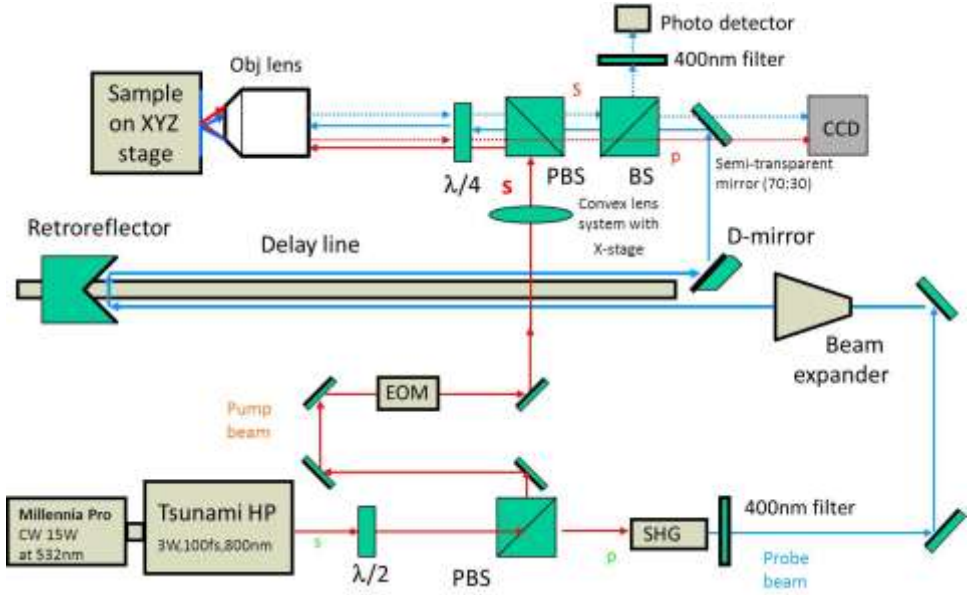

Figure 9-1 Schematic for an optical pump-probe system using a femtosecond laser and a delay line

Thermal properties of a thin film can be anisotropic. Hence, the thermal characterization in a film plane direction is also needed since the thermal conductivity can be different with directions. The value of the thermal conductivity in a lateral direction would be essential to control heat flow for heat/energy assisted magnetic recording.

Figure 9-2 descries lateral thermal characterization using two laser beams. If the position of heating pulse laser and probe laser were separated and precisely controlled, the transient temperature change due to lateral heat transfer can be measured. The sample structure is a metal film on a glass substrate. In this case, the lateral heat conduction should be much faster than the vertical heat conduction through a glass substrate. This might be possible since the thermal diffusivity of a glass is one or two

order smaller than that of a metal.

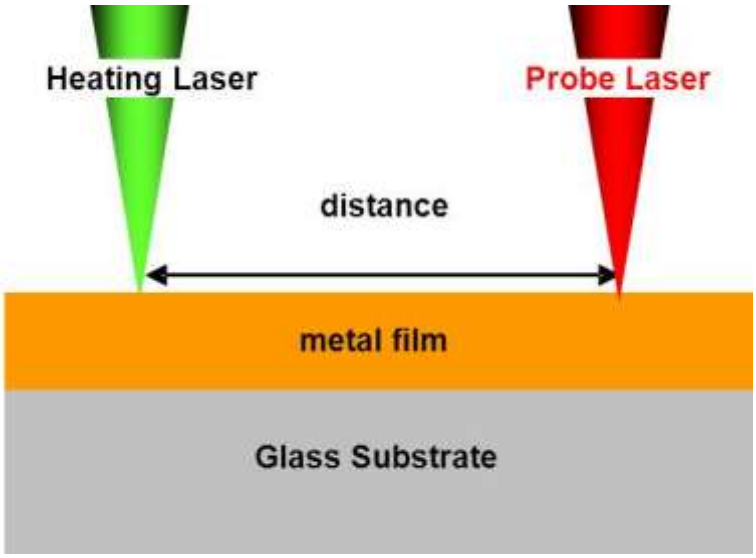

Figure 9-2 Schematic drawing for lateral thermal characterization using two laser beams

However, there are practical problems for this setup. The signal to noise ratio of the probe laser will be very small since the heat will propagate all direction. Another problem is that it is not easy to control the exact position of the two laser spots.

In order to solve the above problems, a converging wave configuration can be suggested [101]. The converging wave configuration using an axicon lens is showed in Figure 9-3. Axicon is a rotationally symmetric prism and a lens composed of a flat surface and a conical surface.

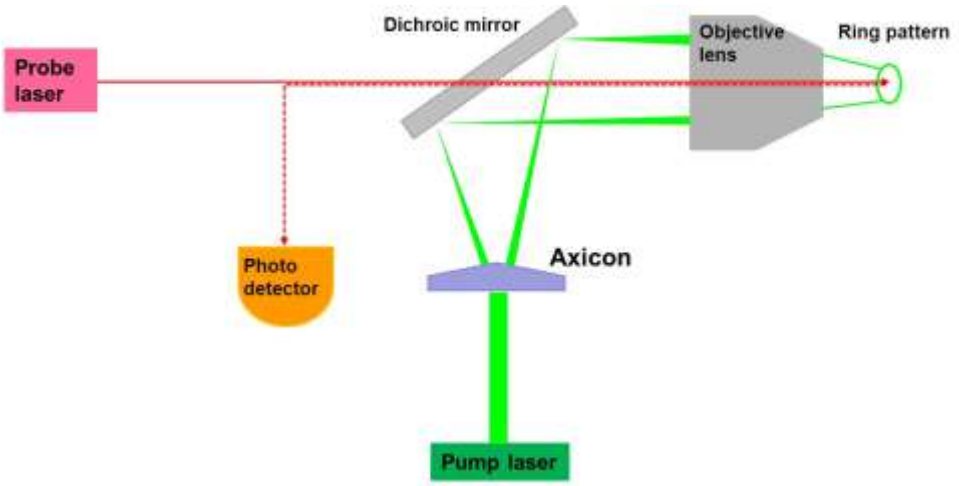

Figure 9-3 Schematic drawing for converging wave configuration using an axicon

Thermal conductivity of a thin film can be measured in lateral direction using the converging wave configuration. Using an axicon, a pump laser beam can be formed as a ring shape. The transient temperature change of the center of the ring can be measured using a probe laser beam. In order to improve the signal to noise ratio, the modulation of a pump laser and a lock-in amplifier can be used. The advantage of this configuration compared with a conventional lateral thermal measurement is to enhance the signal intensity by the factor of $2\pi R$. Here R is the radius of the ring of the pump laser.

Figure 9-4 shows a ring pattern by using an axicon and an objective lens. Figure 9-4(a) is a ring itself for a pulse green laser on a sample surface and Figure 9-4(b) is a probe red laser at the center of the ring. The axicon lens is made using a UV grade Fused Silica with BBAR coating by Del Mar Photonics.

(a)

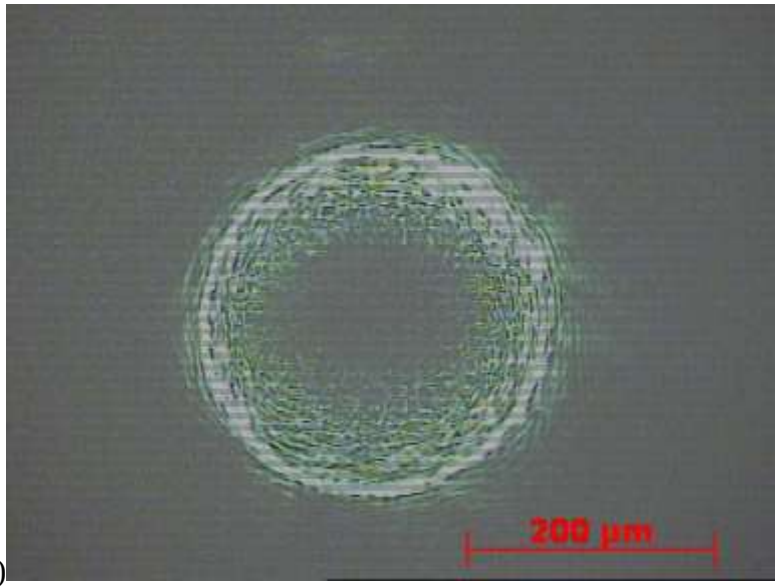

(b)

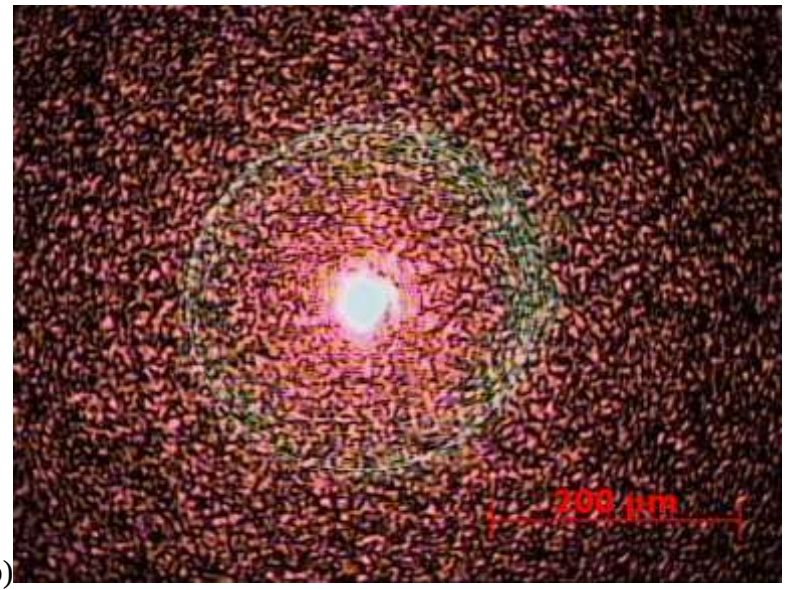

Figure 9-4 Photos of (a) the ring pattern of a green pulse laser (b) a red probe beam at the center of the ring

Reference

1. Franz, R. and G. Wiedemann, *Ueber die Wärme-Leitungsfähigkeit der Metalle*. Annalen der Physik, 1853. **165**(8): p. 497-531.
2. Kittel, C., *Introduction to solid state physics*. 8th ed. 2005, Hoboken, NJ: Wiley. xix, 680 p.
3. Zhang, Y., et al., *Determining the Wiedemann-Franz ratio from the thermal Hall conductivity: Application to Cu and YBa2Cu3O6.95.* Physical Review Letters, 2000. **84**(10): p. 2219-2222.
4. Kumar, G.S., G. Prasad, and R.O. Pohl, *Experimental Determinations of the Lorenz Number.* Journal of Materials Science, 1993. **28**(16): p. 4261-4272.
5. Baibich, M.N., et al., *Giant Magnetoresistance of (001)Fe/(001) Cr Magnetic Superlattices.* Physical Review Letters, 1988. **61**(21): p. 2472-2475.
6. Binasch, G., et al., *Enhanced Magnetoresistance in Layered Magnetic-Structures with Antiferromagnetic Interlayer Exchange.* Physical Review B, 1989. **39**(7): p. 4828-4830.
7. Tsymbal, E.Y. and D.G. Pettifor, *Perspectives of giant magnetoresistance*, in *Solid State Physics*, E. Henry and S. Frans, Editors. 2001, Academic Press. p. 113-237.
8. Sato, H., et al., *Giant Magnetoresistance Related Transport-Properties in Multilayers and Bulk Materials (Invited).* Journal of Applied Physics, 1994. **76**(10): p. 6919-6924.

9. Shi, J., et al., *Field-dependent thermoelectric power and thermal conductivity in multilayered and granular giant magnetoresistive systems.* Physical Review B, 1996. **54**(21): p. 15273.

10. Tsui, F., et al., *Heat conduction of (111) Co/Cu superlattices.* Journal of Applied Physics, 1997. **81**(8): p. 4586-4588.

11. Rausch, T. and T.E. Schlesinger, *Experimental and theoretical investigation of heat assisted magnetic recording*. 2003, Carnegie Mellon University, 2003.: Pittsburgh, Pa. p. xix, 179 p.

12. Kryder, M.H., et al., *Heat Assisted Magnetic Recording.* Proceedings of the Ieee, 2008. **96**(11): p. 1810-1835.

13. Chappert, C., A. Fert, and F.N. Van Dau, *The emergence of spin electronics in data storage.* Nature Materials, 2007. **6**(11): p. 813-823.

14. Dieny, B., *Giant Magnetoresistance in Spin-Valve Multilayers.* Journal of Magnetism and Magnetic Materials, 1994. **136**(3): p. 335-359.

15. Mott, N.F., *Electrons in Transition Metals.* Advances in Physics, 1964. **13**(51): p. 325.

16. Onishi, M., et al., *GMR effect of [Co(Fe)/Cu] multilayer prepared by MBE and IBS methods.* Journal of Magnetism and Magnetic Materials, 2004. **272**: p. E1413-E1415.

17. Parkin, S.S.P., *Systematic variation of the strength and oscillation period of indirect magnetic exchange coupling through the 3d, 4d, and 5d transition metals.* Physical Review Letters, 1991. **67**(25): p. 3598.

18. Dieny, B., et al., *Magnetotransport properties of magnetically soft spin-valve structures (invited).* Journal of Applied Physics, 1991. **69**(8): p. 4774-4779.

19. Parkin, S.S.P. and D. Mauri, *Spin engineering: Direct determination of the Ruderman-Kittel-Kasuya-Yosida far-field range function in ruthenium.* Physical Review B, 1991. **44**(13): p. 7131.

20. Marrows, C.H., et al., *Giant magnetoresistance and oscillatory exchange coupling in disordered Co/Cu multilayers.* Journal of Physics-Condensed Matter, 1999. **11**(1): p. 81-88.

21. Sakakima, H. and M. Satomi, *Oscillations in Low-Field Giant Magnetoresistance in Ni-Fe-Co/Cu(/Co) Superlattices.* Journal of Magnetism and Magnetic Materials, 1993. **121**(1-3): p. 374-377.

22. Parkin, S.S.P., N. More, and K.P. Roche, *Oscillations in exchange coupling and magnetoresistance in metallic superlattice structures: Co/Ru, Co/Cr, and Fe/Cr.* Physical Review Letters, 1990. **64**(19): p. 2304.

23. Silicon Quest International. *The resistivity of standard silicon wafers*. 2011; Available from: http://www.siliconquest.com/StandardSiliconWafers.aspx.

24. Carnegie Mellon Nanofab. *Carnegie Mellon Nanofabrication Facility*. 2011; Available from: http://nanofab.ece.cmu.edu/index.html.

25. Materials Characterization Laboratory. *Carnegie Mellon Materials Characterization Laboratory*. 2011; Available from: http://www.materials.cmu.edu/fac.

26. Moneck, M.T. and J. Zhu, *Development of novel prototype scalable*

magnetoresistive random access memory. 2008, Carnegie Mellon University, 2008.: Pittsburgh, PA. p. xx, 306 p.

27. Grovenor, C.R.M., H.T.G. Hentzell, and D.A. Smith, *The Development of Grain-Structure during Growth of Metallic-Films.* Acta Metallurgica, 1984. **32**(5): p. 773-781.

28. Cullity, B.D., *Introduction to magnetic materials*. Addison-Wesley series in metallurgy and materials. 1972, Reading, Mass.,: Addison-Wesley Pub. Co. xvii, 666 p.

29. Plummer, J.D., M.D. Deal, and P.B. Griffin, *Silicon VLSI technology : fundamentals, practice and modeling*. 2000, Upper Saddle River, NJ: Prentice Hall. xiv, 817 p.

30. Park, J.-H. and J. Zhu, *Magnetoresistive devices with perpendicular magnetic anisotrophy for spin-torque driven applications*. 2010, Carnegie Mellon University, 2010.: Pittsburgh, Pa. p. xv, 174 p.

31. Xactix. *Xetch e1 series*. 2011; Available from: http://www.xactix.com/Xetch_e1_overview.htm.

32. Smitha Shetty, L.S. *Xetch Xenon difluoride Etching system Lab procedure*. 2010; Available from: http://www.ece.cmu.edu/~mems/resources/HH1216/xetch.shtml.

33. Incropera, F.P., *Fundamentals of heat and mass transfer*. 6th ed. 2007, Hoboken, NJ: John Wiley. xxv, 997 p.

34. Yang, Y., R.M. White, and M. Asheghi, *Thermal characterization of Cu/CoFe*

multilayer for giant magnetoresistive head applications. Journal of Heat Transfer-Transactions of the Asme, 2006. **128**(2): p. 113-120.

35. Newnham, R.E., *Properties of materials*. 2005, New York: Oxford University Press.

36. Kreyszig, E., *Advanced engineering mathematics*. 8th ed. 1999, New York: Wiley.

37. Stanoyevitch, A., *Introduction to numerical ordinary and partial differential equations using MATLAB*. Pure and applied mathematics. 2005, Hoboken, N.J.: Wiley-Interscience. xiv, 813 p.

38. Vishay. *Vishay Foil Resistors Z201 (Z-Foil)* 2011;

]. Available from: www.foilresistors.com.

39. Yang, Y., et al., *Field-dependent thermal and electrical transports in Cu/CoFe multilayer.* Journal of Applied Physics, 2006. **99**(6): p. 063703.

40. Cahill, D.G., *Thermal-Conductivity Measurement from 30-K to 750-K - the 3-Omega Method.* Review of Scientific Instruments, 1990. **61**(2): p. 802-808.

41. Zink, B.L., et al., *Exploring thermoelectric effects and Wiedemann-Franz violation in magnetic nanostructures via micromachined thermal platforms.* Solid State Communications, 2010. **150**(11-12): p. 514-518.

42. University wafer. *thermally grown oxide wafer*. 2011; Available from: http://www.universitywafer.com/Wafers___Services/Thermal_Oxide/thermal_oxide.html.

43. Dieny, B., et al., *Spin-Valve Effect in Soft Ferromagnetic Sandwiches.* Journal

of Magnetism and Magnetic Materials, 1991. **93**: p. 101-104.

44. Inomata, K. and Y. Saito, *Giant Magnetoresistance and Low Saturation Fields in Co-Fe/Cu Multilayers.* Journal of Magnetism and Magnetic Materials, 1993. **126**(1-3): p. 425-429.

45. Yamamoto, H., et al., *Magnetoresistance of Non-Coupled [Nife/Cu/Co/Cu] Multilayers.* Journal of Magnetism and Magnetic Materials, 1993. **126**(1-3): p. 437-439.

46. Dieny, B., V.S. Speriosu, and S. Metin, *Thermal Variation of the Magnetoresistance of Soft Spin-Valve Multilayers.* Europhysics Letters, 1991. **15**(2): p. 227-232.

47. Lu, L., W. Yi, and D.L. Zhang, *3 omega method for specific heat and thermal conductivity measurements.* Review of Scientific Instruments, 2001. **72**(7): p. 2996-3003.

48. Dames, C. and G. Chen, *1 omega, 2 omega, and 3 omega methods for measurements of thermal properties.* Review of Scientific Instruments, 2005. **76**(12): p. 124902.

49. Widom, M., *Discussion about thermal conductivty in metals in Solid State Physics class at Carnegie Mellon University*. 2011.

50. Bandyopadhyay, S. and M. Cahay, *Electron spin for classical information processing: a brief survey of spin-based logic devices, gates and circuits.* Nanotechnology, 2009. **20**(41): p. 412001.

51. Pichanusakorn, P. and P. Bandaru, *Nanostructured thermoelectrics.* Materials

Science & Engineering R-Reports, 2010. **67**(2-4): p. 19-63.

52. Tellier, C.R., Tosser, A. J., *Size effects in thin films* 1982, New York: Elsevier.

53. Cahill, D.G., et al., *Nanoscale thermal transport.* Journal of Applied Physics, 2003. **93**(2): p. 793-818.

54. Stevens, R.J., A.N. Smith, and P.M. Norris, *Measurement of thermal boundary conductance of a series of metal-dielectric interfaces by the transient thermoreflectance technique.* Journal of Heat Transfer-Transactions of the Asme, 2005. **127**(3): p. 315-322.

55. Swartz, E.T. and R.O. Pohl, *Thermal-Boundary Resistance.* Reviews of Modern Physics, 1989. **61**(3): p. 605-668.

56. Plummer, J.D., Deal, ,M. D., Griffin, P. B. , *Silicon VLSI technology* 2000, New Jersey: Prentice Hall.

57. Smith, A.N., J.L. Hostetler, and P.M. Norris, *Thermal boundary resistance measurements using a transient thermoreflectance technique.* Microscale Thermophysical Engineering, 2000. **4**(1): p. 51-60.

58. Ujihara, K., *Reflectivity of Metals at High-Temperatures.* Journal of Applied Physics, 1972. **43**(5): p. 2376.

59. Iizuka, K., *Elements of photonics*. Wiley series in pure and applied optics. 2002, New York, N.Y.: Wiley-Interscience. 2 v. (xxviii, 1197, 25 p.).

60. Hopkins, P.E., et al., *Criteria for Cross-Plane Dominated Thermal Transport in Multilayer Thin Film Systems During Modulated Laser Heating.* Journal of Heat Transfer, 2010. **132**(8): p. 081302.

61. Scouler, W.J., *Temperature-Modulated Reflectance of Gold from 2 to 10 Ev.* Physical Review Letters, 1967. **18**(12): p. 445.

62. Chen, G. and P. Hui, *Pulsed photothermal modeling of composite samples based on transmission-line theory of heat conduction.* Thin Solid Films, 1999. **339**(1-2): p. 58-67.

63. Cheng, D.K., *Field and wave electromagnetics*. Addison-Wesley series in electrical engineering. 1983, Reading, Mass.: Addison Wesley. xvi, 576 p.

64. Pozar, D.M., *Microwave engineering*. 3rd ed. 2005, Hoboken, NJ: J. Wiley. xvii, 700 p.

65. Graf, U., *Applied Laplace transforms and z-transforms for scientists and engineers : a computational approach using a Mathematica package*. 2004, Basel ; Boston: Birkhäuser. x, 500 p.

66. Stehfest, H., *Algorithm 368: Numerical inversion of Laplace transforms [D5]*. Communications of the ACM, 1970. **13**(1): p. 47-49.

67. Kading, O.W., H. Skurk, and K.E. Goodson, *Thermal Conduction in Metallized Silicon-Dioxide Layers on Silicon.* Applied Physics Letters, 1994. **65**(13): p. 1629-1631.

68. Jeong, T. and J.-G. Zhu, *Thermal Conductivity Measurement of Cobalt-Iron Thin Films Using the Time-Resolved Thermoreflectance Technique.* ASME Conference Proceedings, 2009. **2009**(43574): p. 235-240.

69. Griffin, A.J., F.R. Brotzen, and P.J. Loos, *The Effective Transverse Thermal-Conductivity of Amorphous Si3n4 Thin-Films.* Journal of Applied

Physics, 1994. **76**(7): p. 4007-4011.

70. Gundrum, B.C., D.G. Cahill, and R.S. Averback, *Thermal conductance of metal-metal interfaces.* Physical Review B, 2005. **72**: p. 245426.

71. Swartz, E.T. and R.O. Pohl, *Thermal-Resistance at Interfaces.* Applied Physics Letters, 1987. **51**(26): p. 2200-2202.

72. Reddy, P., K. Castelino, and A. Majumdar, *Diffuse mismatch model of thermal boundary conductance using exact phonon dispersion.* Applied Physics Letters, 2005. **87**(21): p. 211908.

73. Costescu, R.M., M.A. Wall, and D.G. Cahill, *Thermal conductance of epitaxial interfaces.* Physical Review B, 2003. **67**(5): p. 054302.

74. Lyeo, H.K. and D.G. Cahill, *Thermal conductance of interfaces between highly dissimilar materials.* Physical Review B, 2006. **73**(14): p. 114301.

75. Stoner, R.J. and H.J. Maris, *Kinetic Formula for Estimating Resistive Phonon Lifetimes.* Physical Review B, 1993. **47**(18): p. 11826-11829.

76. Khater, A. and J. Szeftel, *Theory of the Kapitza Resistance.* Physical Review B, 1987. **35**(13): p. 6749-6755.

77. Nan, C.W. and R. Birringer, *Determining the Kapitza resistance and the thermal conductivity of polycrystals: A simple model.* Physical Review B, 1998. **57**(14): p. 8264-8268.

78. Yovanovich, M.M., *Influence of surface roughness and waviness upon thermal contact resistance*, in *Mechanical engineering*. 1967, Massachusetts Institute of Technology.

79. Michael A. Hall, N.J.D., Riccardo DeSalvo, Takayuki Tomaru, Francesco Fidecaro, *Surface Roughness and Thermal Conductivity for Sapphire Fibers: Reducing the Thermal Noise in Gravitational Wave Interferometers*. 2003, Laser interferometer gravitational-wave observatory (LIGO). p. 18.

80. Thomson, J.J., *On the theory of electric conduction through thin metallic films.* Proceedings of the Cambridge Philosophical Society, 1902. **11**: p. 120-122.

81. Fuchs, K., *The conductivity of thin metallic films according to the electron theory of metals.* Proceedings of the Cambridge Philosophical Society, 1938. **34**: p. 100-108.

82. Sondheimer, E.H., *The Mean Free Path of Electrons in Metals.* Advances in Physics, 1952. **1**(1): p. 1-42.

83. Mayadas, A.F. and M. Shatzkes, *Electrical-Resistivity Model for Polycrystalline Films - Case of Arbitrary Reflection at External Surfaces.* Physical Review B, 1970. **1**(4): p. 1382.

84. Jandel. *Four point Probes*. 2011 [cited 2011; Four point Probes by jandel]. Available from: http://www.jandel.co.uk/probeheads.htm.

85. Smits, F.M., *Measurement of Sheet Resistivities with the 4-Point Probe.* Bell System Technical Journal, 1958. **37**(3): p. 711-718.

86. Chopra, K.L., *Thin film phenomena*. 1969, New York,: McGraw-Hill. xx, 844 p.

87. Tellier, C.R. and A.J. Tosser, *Size effects in thin films*. Thin films science and

technology. 1982, Amsterdam ; New York: Elsevier. ix, 310 p.

88. Zhigal'skii, G.P. and B.K. Jones, *The physical properties of thin metal films*. Electrocomponent science monographs. 2003, London ; New York: Taylor & Francis. xiv, 215 p.

89. Hoffmann, H., J. Vancea, and U. Jacob, *Surface Scattering of Electrons in Metals.* Thin Solid Films, 1985. **129**(3-4): p. 181-193.

90. Jacob, U., J. Vancea, and H. Hoffmann, *A New Method for Determining the Electronic Mean Free-Path in Polycrystalline Metals.* Journal of Physics-Condensed Matter, 1989. **1**(49): p. 9867-9873.

91. Ziman, J.M., *Electrons and phonons; the theory of transport phenomena in solids*. The International series of monographs on physics. 1960, Oxford,: Clarendon Press. xiv, 554 p.

92. Reynolds, F.W. and G.R. Stilwell, *Mean Free Paths of Electrons in Evaporated Metal Films.* Physical Review, 1952. **88**(2): p. 418-419.

93. Chopra, K.L. and S.K. Bahl, *Hall Effect in Thin Metal Films.* Journal of Applied Physics, 1967. **38**(9): p. 3607.

94. Ashcroft, N.W. and N.D. Mermin, *Solid state physics*. 1976, New York,: Holt. xxi, 826 p.

95. Suri, R., A.P. Thakoor, and K.L. Chopra, *Electron-Transport Properties of Thin Copper-Films .1.* Journal of Applied Physics, 1975. **46**(6): p. 2574-2582.

96. Spallas, J.P., et al., *Improved performance of Cu-Co CPP GMR sensors.* Ieee Transactions on Magnetics, 1997. **33**(5): p. 3391-3393.

97. Bass, J. and W.P. Pratt, *Current-perpendicular (CPP) magnetoresistance in magnetic metallic multilayers.* Journal of Magnetism and Magnetic Materials, 1999. **200**(1-3): p. 274-289.

98. Zhu, J.-G. and C. Park, *Magnetic tunnel junctions.* Materials Today, 2006. **9**(11): p. 36-45.

99. Hopkins, P.E., et al., *Influence of interfacial mixing on thermal boundary conductance across a chromium/silicon interface.* Journal of Heat Transfer-Transactions of the Asme, 2008. **130**(6): p. 062402.

100. Schmidt, A., et al., *An optical pump-probe technique for measuring the thermal conductivity of liquids.* Review of Scientific Instruments, 2008. **79**(6): p. 064902.

101. Cielo, P., L.A. Utracki, and M. Lamontagne, *Thermal-Diffusivity Measurements by the Converging-Thermal-Wave Technique.* Canadian Journal of Physics, 1986. **64**(9): p. 1172-1177.